2011

Organic Light-Emitting Diodes (OLEDs) and Optically-Detected Magnetic Resonance (ODMR) studies on organic materials

Min Cai
Iowa State University

Organic Light-Emitting Diodes (OLEDs) and Optically-Detected Magnetic Resonance (ODMR) studies on organic materials

by

Min Cai

A dissertation submitted to the graduate faculty

in partial fulfillment of the requirements for the degree of

DOCTOR OF PHILOSOPHY

Major: Condensed Matter Physics

Program of Study Committee:

Joseph Shinar, Major Professor
Alex Travesset
David Vaknin
John Lajoie
Vikram Dalal

Iowa State University

Ames, Iowa

2011

TABLE OF CONTENTS

Abstract

Organic semiconductors have evolved rapidly over the last decades and currently are considered as the next-generation technology for many applications, such as organic light-emitting diodes (OLEDs) in flat-panel displays (FPDs) and solid state lighting (SSL), and organic solar cells (OSCs) in clean renewable energy. This dissertation focuses mainly on OLEDs.

Although the commercialization of the OLED technology in FPDs is growing and appears to be just around the corner for SSL, there are still several key issues that need to be addressed: (1) the cost of OLEDs is very high, largely due to the costly current manufacturing process; (2) the efficiency of OLEDs needs to be improved. This is vital to the success of OLEDs in the FPD and SSL industries; (3) the lifetime of OLEDs, especially blue OLEDs, is the biggest technical challenge. All these issues raise the demand for new organic materials, new device structures, and continued lower-cost fabrication methods.

In an attempt to address these issues, we used solution-processing methods to fabricate highly efficient small molecule OLEDs (SMOLEDs); this approach is cost-effective in comparison to the more common thermal vacuum evaporation. We also successfully made efficient indium tin oxide (ITO)-free SMOLEDs to further improve the efficiency of the OLEDs. We employed the spin-dependent optically-detected magnetic resonance (ODMR) technique to study the luminescence quenching processes in OLEDs and organic materials in order to understand the intrinsic degradation mechanisms. We also fabricated polymer LEDs (PLEDs) based on a new electron-accepting blue-emitting polymer and studied the effect of molecular weight on the efficiency of PLEDs.

All these studies helped us to better understand the underlying relationship between the organic semiconductor materials and the OLEDs' performance, and will subsequently assist in further enhancing the efficiency of OLEDs. With strongly improved device performance (in addition to other OLEDs' attributes such as mechanical flexibility and potential low cost), the OLED technology is promising to successfully compete with current technologies, such as LCDs and inorganic LEDs.

Dissertation Organization

This dissertation comprises 8 chapters and consists mainly of papers published or prepared for submission. Chapters 1 and 2 provide a general introduction to OLED technology and ODMR, respectively. Chapters 3 – 5 and 7 are based on published papers; Chapter 6 is based on a paper in preparation.

In Chapter 3, high efficiency solution-processed small molecule electrophosphorescent OLEDs is presented. Chapter 4 describes indium-tin-oxide- (ITO) free Alq_3 OLEDs with 80% enhanced power efficiency compared to similar LEDs with an ITO anode. In Chapter 5, the effect of the molecular weight on the efficiency of poly(*N*-vinylcarbazole)-based PLEDs is discussed. Chapter 6 presents blue fluorescent OLEDs based on a new electron-accepting polymer. Chapter 7 discusses the PLDMR studies of rubrene and oxygen-doped rubrene films and powders. Finally, the general conclusions of this dissertation are summarized in Chapter 8.

Chapter 1. Introduction to Organic Light-Emitting Diodes (OLEDs)

Brief history of OLED technology

A. Bernanose and co-workers at the Université de Nancy, France, first discovered electroluminescence (EL) in organic materials in the early 1950s by applying high-voltage alternating current (AC) to crystalline thin films of acridine orange and quinacridone (Fig. 1-1), but the EL was only a short burst of light at that time. They proposed a mechanism of either direct excitation of the dye molecules or excitation of electrons [1-4].

In the 1960s, Martin Pope and his group at New York University made seminal discoveries, including the ohmic, injecting electrode contacts to organic crystals, direct current (DC) EL, under vacuum, from a single crystal of pure anthracene as well as tetracene-doped anthracene, (Fig. 1-1) [5-8]. Also in the 1960s, W. Helfrich and W. G. Schneider produced double injection recombination EL for the first time, in an anthracene single crystal using hole and electron injecting electrodes whose work functions satisfied the requirements specified by Pope's group [9]. In parallel, in the 1970s, the EL from polymer films was first observed by Roger Partridge at the National Physical Laboratory in the United Kingdom, and the first polymer LEDs (PLEDs), consisting of a film of poly(*N*-vinylcarbazole) (PVK) up to 2.2 μm thick located between two charge injecting electrodes, was reported. The results of the project were patented in 1975 and published in 1983 [10-13]. However, at that time, the conductivity σ of such materials was so low that the devices required very high driving voltages V (> 100 V), which limited light output and did not attract industry interest.

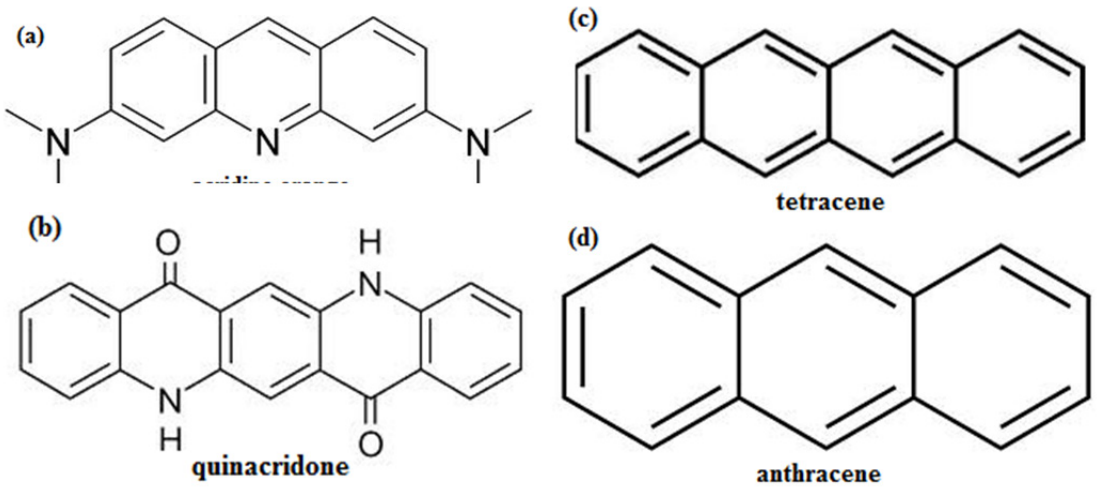

Fig. 1-1. *Chemical structures of (a) acridine orange, (b) quinacridone (c) tetracene and (d) anthracene.*

OLED technology began to draw serious commercial attention following Tang and Van Slyke's report in 1987 [14]. Working at Eastman Kodak, they successfully developed the first OLEDs with a luminance of over 1000 Cd/m^2 at $V \sim 10$ V. Their diode used a novel two-layer structure with a separate hole transporting layer (N,N'-diphenyl-N,N'-bis (3-methylphenyl) 1,1'-biphenyl-4, 4' diamine (TPD)) and an electron transporting layer (tris(8-hydroxyquinoline) aluminum (Alq_3)) such that recombination and light emission occurred in the middle of the organic layers. This resulted in a reduction in V and improvement in efficiency, and it launched the current era of OLED research and device development and production. The device structure and chemical structures are shown in Fig. 1-2 [14].

In 1990 J. H. Burroughes *et al.* at the Cavendish Laboratory in Cambridge reported the first low-V green PLEDs using 100-nm thick films of poly(*p*-phenylene vinylene) (PPV) [15].

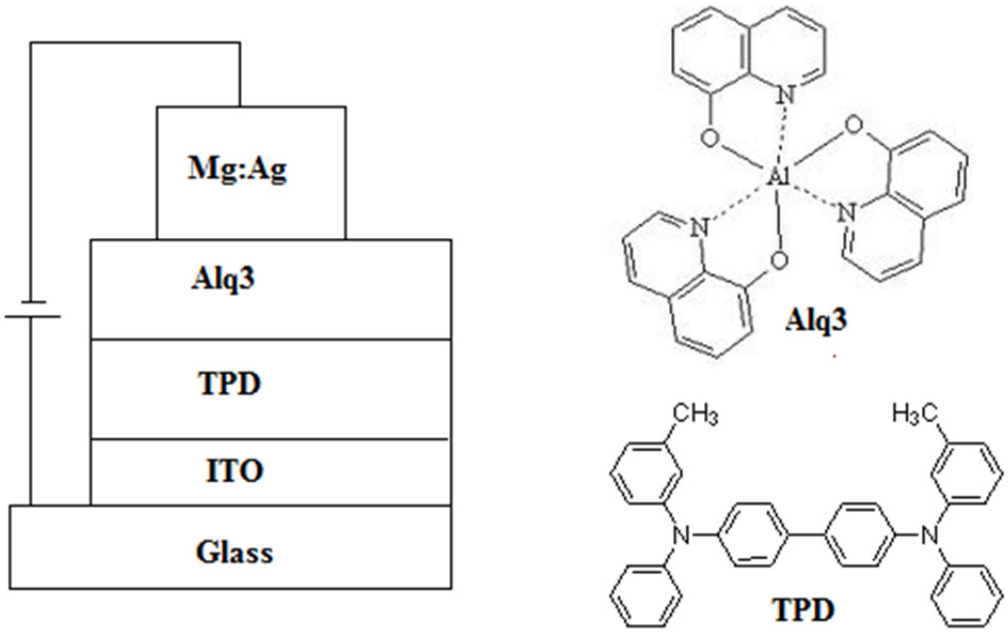

Fig. 1-2. *Device structure of Tang and Van Slyke's first heterojunction OLEDs and molecular structures of TPD and Alq_3.*

In the late 1990s and early 2000s, the groundbreaking work of S. R. Forrest, M. E. Thompson and their groups on phosphorescent OLEDs overcame the 25% limit on the internal quantum efficiency η_{int} of fluorescent OLEDs, further improving the efficiency of OLEDs dramatically. As well known, only the singlet excitons (SEs), which comprise 25% of the excited states, generate light in fluorescent organic materials. The other 75% of the excited states, which are triplet excitons (TEs), are almost entirely lost through nonradiative decay. However, the phosphorescent organic molecules, which usually contain a heavy metal atom at the center of the molecule, for example platinum or iridium, generate light from both triplet and singlet excitons by the fast and efficient intersystem crossing (ISC), allowing η_{int} of such materials to reach nearly 100%. Thus phosphorescent OLEDs (PHOLEDs) with power efficiency over 100 lm/W have been realized, rendering OLEDs as the next-generation

technology for both flat-panel displays and solid state lighting more and more competitive. The molecular structures of 3 widely-used phosphorescent materials, (a) Pt(II)octaethylporphine (PtOEP), (b) Tris(2-phenylpyridine)iridium(III) ($Ir(ppy)_3$) and (c) Bis(3,5-difluoro-2-(2-pyridyl)phenyl-(2-carboxypyridyl)iridium(III) (FIrpic) are shown in Fig. 1-3 [16-18].

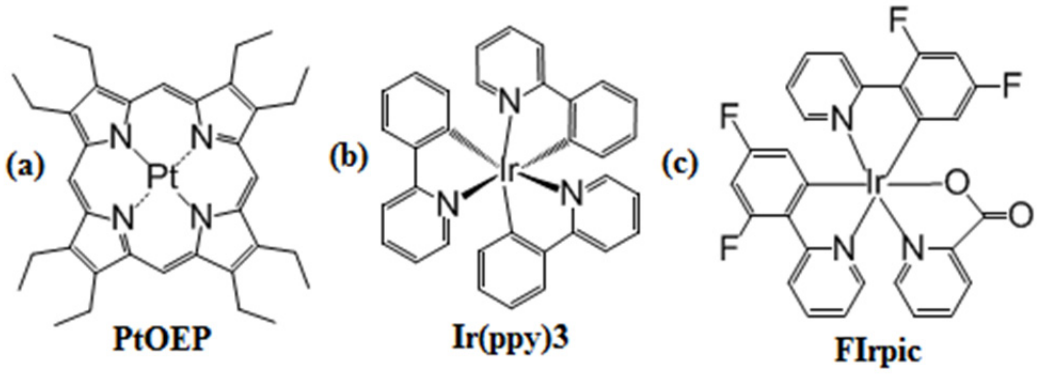

Fig. 1-3. *Molecular structures of 3 widely-used phosphorescent materials: (a) PtOEP (b) $Ir(ppy)_3$ (c) FIrpic.*

Organic semiconductor materials: conjugated aromatic hydrocarbons

Organic materials comprise ~90% of the two million known materials. However, among them, only a small fraction are conductive. These are typically conjugated aromatic molecules, i.e., they consist of alternating single and double bonds [19].

The electronic configuration of the carbon atom's ground state is $1s^2 2s^2 2p^2$ (Fig. 1-4). In the tetrahedral methane or diamond bonding configuration, the four valence electrons in the $n = 2$ shell occupy sp^3 orbitals that result from the hybridization of a $2s$ and three $2p$ orbitals. However, it is possible that the $2s$ orbital will hybridize with only two of the three available $2p$ orbitals to form three sp^2 orbitals with one p-orbital (p_z) remaining. The 3 sp^2 orbitals are all coplanar and oriented at 120° from each other; the bonds formed by these 3 sp^2 orbitals are called σ-bonds. The p_z orbital is

perpendicular to the plane of sp^2 hybridization, and the overlapping neighboring p_z orbitals form the so-called π-bond, which allows a delocalization of π-electrons across all the adjacent aligned p orbitals, and these delocalized π-electrons are responsible for the semiconducting properties of π-conjugated materials [19].

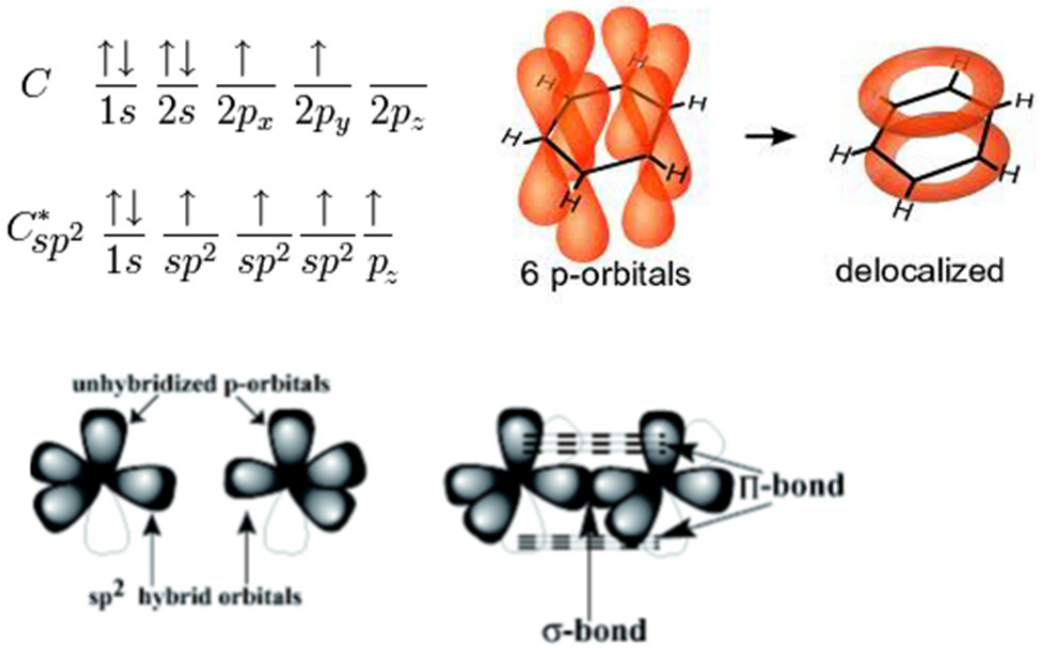

Fig. 1-4. *The electronic configuration of the carbon atom's ground state, sp^2 hybridization, and the formation of π-bonds.*

The molecular orbital (MO) wavefunctions based on linear combinations of atomic orbitals (LCAO) are the most extensively used in MO theory. According to LCAO, for a molecule that has N carbon atoms, the wavefunction of a π-MO can be written as

$$\psi_\pi = \sum_{l=1}^{N} a_l \phi_l \qquad (1.1)$$

where the ϕ_l terms are atomic orbitals, and the a_l terms are coefficients determined by minimizing the total energy of the system. By the Pauli principle, each can

accommodate two electrons of opposite spin, so the ground state wavefunction of the system is

$$\psi_\pi(ground) = \psi_1\alpha_1\psi_1\beta_1 \ldots \psi_{N/2}\alpha_{N/2}\psi_{N/2}\beta_{N/2} \quad (1.2)$$

where the ψ_l terms are functions of Eq. 1 and ordered according to increasing energy, i.e., $E_l > E_{l-1}$; α_l and β_l denote electron spin functions for up and down orientation, respectively. When the molecule is in its ground state, the unfilled and filled MOs are called antibonding and bonding MOs, respectively.

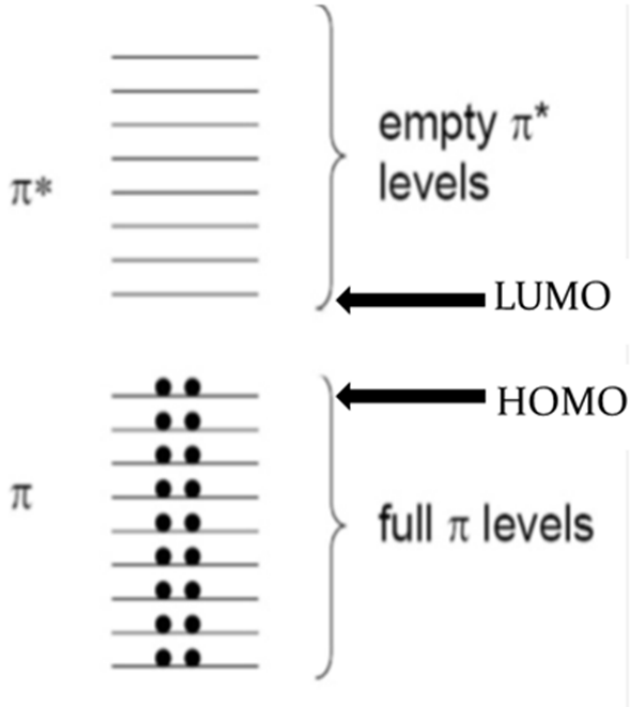

Fig. 1-5. *The HOMO and LUMO of a molecule.*

The excited states are formed by exciting one of the bonding electrons to an unfilled antibonding MO. The lowest energy required for that is to excite an electron in the highest occupied molecular orbital (HOMO) to the lowest unoccupied molecular orbital (LUMO). HOMO and LUMO here are thus analogous to the valence and conduction bands of inorganic semiconductors (Fig. 1-5). The energy

difference between the HOMO and LUMO level is regarded as the band gap energy, E_g, corresponding to the photon energy E_{Photon} in the optical transitions of absorption or radiative emission [19].

After a molecule is electronically excited, there are numerous routes for its decay to the ground state, such as radiative or nonradiative. A process of internal relaxation that occurs within a given spin manifold is termed internal conversion, whereas if the spin multiplicity changes it is called intersystem crossing (ISC). For the radiative decays, according to the quantum mechanical selection rules, the optical transitions for organic molecules include at least three different sources and can be written as:

$$R_{lu}^2 \propto \left|\langle \psi_{e_l} | \boldsymbol{M} | \psi_{e_u} \rangle\right|^2 \left|\langle \chi_{v_l} | \chi_{v_l} \rangle\right|^2 \left|\langle \psi_{s_l} | \psi_{s_u} \rangle\right|^2 \qquad (1.3)$$

1) The first term contains the dipole moment operator $\boldsymbol{M}$. Dipole-allowed transitions are those for which the transition moment is different from zero.

$$\boldsymbol{T}_{lu} = \langle \psi_l | \boldsymbol{M} | \psi_u \rangle \qquad (1.4)$$

It is clear that since $\boldsymbol{M}$ is a sum of odd operators, $\boldsymbol{T}_{lu}$ vanishes unless l and u are of opposite symmetry with respect to the inversion operator.

2) The second term relates the vibrational degrees of freedom. The transition amplitude for a vibronic transition can be written

$$\boldsymbol{T}_{lm,un} = \boldsymbol{T}_{lu} \langle \chi_{lm} | \chi_{un} \rangle \qquad (1.5)$$

The χ terms are the vibrational state wavefunctions; $|\langle \chi_{lm} | \chi_{un} \rangle|^2$ is called the Franck-Condon factor. A Franck-Condon transition is a vertical transition as denoted by the blue arrow in Fig.1-6. Generally, after the excited electron relaxes to the lowest vibrational n = 0 state, which occurs within ~1 ps, the electron can return to the ground state by emitting a photon or by other processes. As clearly seen in Fig. 1-6, there is an energy difference, called the

Stokes shift, between the peak in the fundamental absorption band and the peak in the emission band.

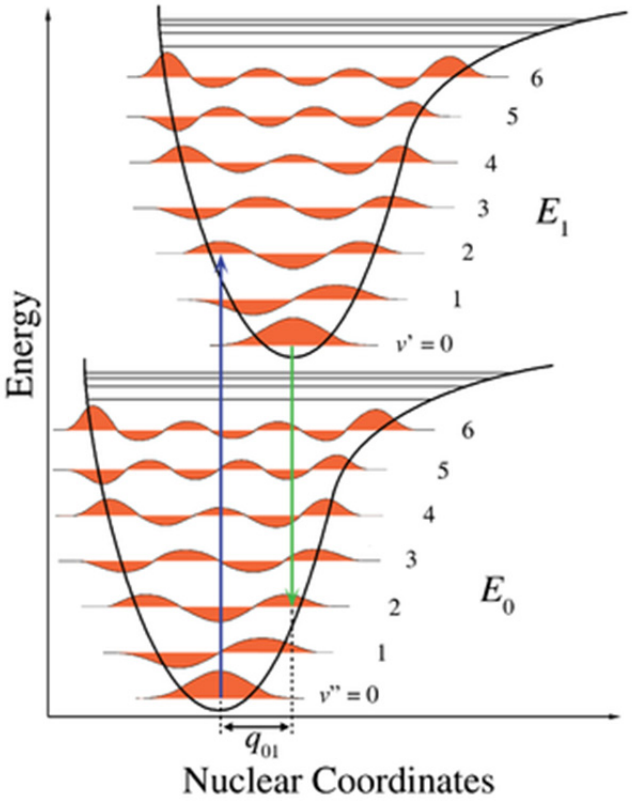

Fig. 1-6. *Franck–Condon principle energy diagram. Since electronic transitions are very fast compared with nuclear motions, vibrational levels are favored when they correspond to a minimal change in the nuclear coordinates.*

3) The third term is the spin selection rules. As long as the interactions between the spin and orbital angular momentum are small, the total wavefunction can be written as a product of wavefunctions on the spatial orbital and coordinates of the electrons. Under this condition, only states of the same spin quantum number *S* combine with each other. Thus in the absence of spin-orbit effects, transitions from singlet to the triplet states are totally forbidden [19].

The internal conversion is a radiative decay between the lowest excited singlet state S_1 and the ground state S_0 and it is called fluorescence. Internal conversion is often a fast process; the typical fluorescence lifetime τ_{flu} is ~10^{-9} – 10^{-8} s. On the other hand, a ISC process occuring between the lowest excited triplet state T_1 and the ground state S_0 is called phosphorescence. Because of the Pauli exclusion principle, two electrons in the triplet state are in different orbitals, the electron-electron repulsion is less than that between the electrons in a singlet state, thus the energy of S_1 state always lies higher than that of T_1 state in a given molecule. Hence, phosphorescence always occurs at longer wavelengths than those of fluorescence. ISC is often a slow process, and the typical phosphorescence lifetime τ_{pho} is ~10^{-6} to 10 s.

The Jablonski diagram for absorption, fluorescence, and phosphorescence is shown in Fig. 1-7. As mentioned above, the ground state S_0 for the organic molecules is a singlet state, so the direct decay from T_1 to S_0 is totally forbidden. It becomes partially allowed only if the spin-orbit interaction is increased and space and spin degrees of freedom are more strongly mixed.

Electrons and holes are both fermions with spin = 1/2. Excitons formed by the recombination of the hole-electron pairs may either be in a singlet or triplet state, depending on how the spins of two particles combine. Statistically, 25% of the excitons are singlet excitons (SEs) and 75% of them are triplet excitons (TEs) [20-21]. Radiative decay of the excitons results in the production of light through spontaneous emission. In OLEDs using fluorescent organic emitters, there is almost no light generated from the decay of TEs, which decay through nonradiative channels. Hence, this places a theoretical limit on η_{int} (the ratio of the total number of photons generated within the OLEDs to the number of electrons injected) of 25% [22-23].

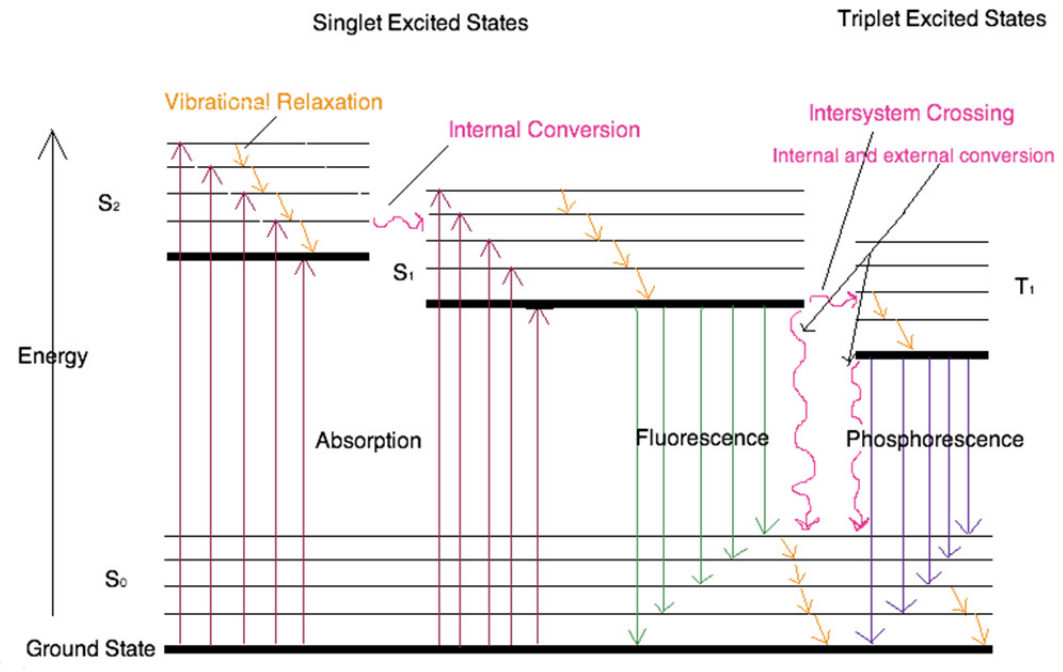

Fig. 1-7. *Jablonski diagram for absorption, fluorescence, and phosphorescence.*

However, the phosphorescent organic emitters usually contain a heavy metal atom at the center of the molecule, for example platinum [16] or iridium [18], of which the green emitting complex tris[2-(p-tolyl)pyridine]iridium(III) ($Ir(mppy)_3$) is one of many examples [24]. The large spin-orbit interaction experienced by the molecule due to this heavy metal atom facilitates ISC. This reduces the lifetime of the triplet state, so phosphorescence is readily observed [17,25]. The phosphorescent OLEDs generate light from both triplet and singlet excitons, allowing η_{int} of such devices to reach nearly 100% [18].

OLEDs fabrication methods

Generally, π-conjugated materials are divided into two categories, small molecules and polymers. A polymer is a large molecule (macromolecule) composed of *n*

repeating structural units ($n >> 1$). Small molecules usually have a much lower molecular weight (M_W) and are much easier to purify. Accordingly, OLEDs are also divided into two types, small molecule OLEDs (SMOLEDs) and polymer OLEDs (PLEDs).

The fabrication of SMOLEDs usually involves thermal evaporation in a vacuum as shown in Fig. 1-8. The vacuum deposition process enables the formation of well controlled, homogeneous films, and the construction of very complex multilayer structures. This high flexibility in layer design, enabling distinct charge transport and charge blocking layers to be formed, is the main reason for the high efficiencies of SMOLEDs [26-27]. However, due to the requirement of high vacuum ($< 10^{-6}$ Torr), the fabrication process is more complicated and expensive and the device size is limited [28-29].

Because polymers are too large to be thermally evaporated (at high temperature they either decompose or crosslink), PLEDs are fabricated by solution processing techniques, such as, spin-coating, inkjet printing, and screen printing. These solution processing techniques allow potentially large-area and cost-efficient PLEDs [29-30], but the efficiencies of PLEDs are not comparable to those of SMOLEDs, mainly due to the difficulty of fabricating complex device structures that require orthogonal organic solvents [31].

The different "stages" of spin coating are shown in Fig. 1-8. The first stage is called “dispensation”, which means deposition of the coating fluid onto the wafer or substrate. The second is the “acceleration” stage, in which the substrate is accelerated up to its final, desired, rotation speed. The third is the “flow dominated” stage, in which the substrate is spanned at a constant rate and viscous fluid forces dominate the

fluid thinning behavior at this stage. The last stage is the "evaporation dominated," in which the substrate is still spun at a constant rate but solvent evaporation dominates the coating thinning behavior.

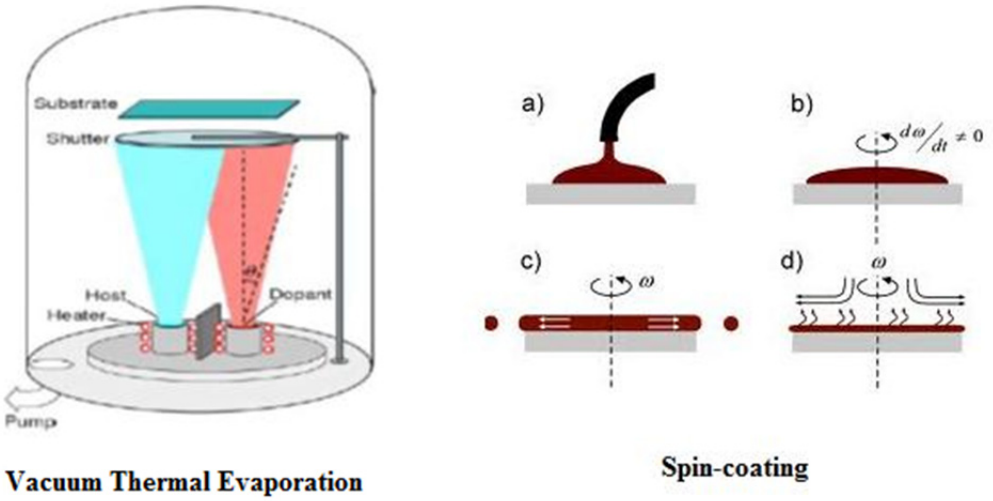

Fig. 1-8. *Comparison of Vacuum Thermal Evaporation and spin-coating technologies.*

Device structure of OLEDs

The device structure of the early OLEDs was very simple, consisting of only a single organic layer between the anode and the cathode. One example was the first PLEDs demonstrated by Burroughes *et al.*, which involved a single layer of PPV. The quantum efficiency of the PLEDs was only ~0.05%, partially due to lack of a heterostructure [15].

As mentioned, the first small molecule bilayer heterojunction OLEDs contained two organic layers, the TPD hole transport material and the Alq_3, emitting and electron transport material [14]. By inserting the separated hole transport layer, the quantum efficiency of the SMOLEDs was drastically improved, approximately ~100 fold, to ~ 1%, compared to the predated thermally deposited anthracene

electroluminescent devices [14,32]. Then in the first heterojunction PLEDs, reported in 1992, a polymeric heterostructure was developed using an electron transport layer of the molecular material 2-(4-biphenylyl)-5-(4-tert-butylphenyl)-1,3,4-oxadiazole (PBD) dispersed in insulating poly(methyl methacrylate) (PMMA). This improved the EL quantum efficiency to 0.8% [33]. With these studies, organic materials first showed their potential as an efficient emissive technology applicable to all aspects of the display and lighting industry. An intense examination by scientists and engineers followed.

Now, after decades of fast developments in OLED technology, the structure of advanced OLEDs has become more and more complicated, especially in SMOLEDs fabricated by thermal vacuum evaporation. The multilayered OLEDs can consist of as many as seven different organic layers situated between two electrodes. The layers typically include a hole injection layer (HIL), hole transport layer (HTL), electron blocking layer (EBL), emitting layer (EML), hole blocking layer (HBL), electron transport layer (ETL), and electron injection layer (EIL) (Fig. 1-9). The organic materials are typically classified according to their functions. The HIL (EIL) is the buffer layer between the anode (cathode) and adjacent HTL (ETL), which reduces the hole (electron) injection barrier and facilitates charge injection. Poly(3,4-ethylenedioxythiophene):poly(4-styrenesulfonate) (PEDOT:PSS) and MoO_3 are two typical hole injection materials (HIM) [34-35]. LiF and CsF are two widely-used electron injection materials (EIM) [36-37].

The HTL (ETL) rapidly transports the injected holes (electrons) to the recombination zone (RZ), which is located within the EML, so the hole transport materials (HTM) or electron transport materials (ETM) are designed to have high hole or electron mobility μ_h and μ_e, respectively. N,N'- bis(naphthalen-1-yl)-N,N'-

bis(phenyl)-2,2'-dimethylbenzidine (NPD) and Di-[4-(N,N-ditolyl-amino)-phenyl]cyclohexane (TAPC) are good HTMs [38-39]; Alq_3 and 4,7-diphenyl-1,10-phenanthroline (BPhen) are good ETMs [40-41]. The EBL (HBL)

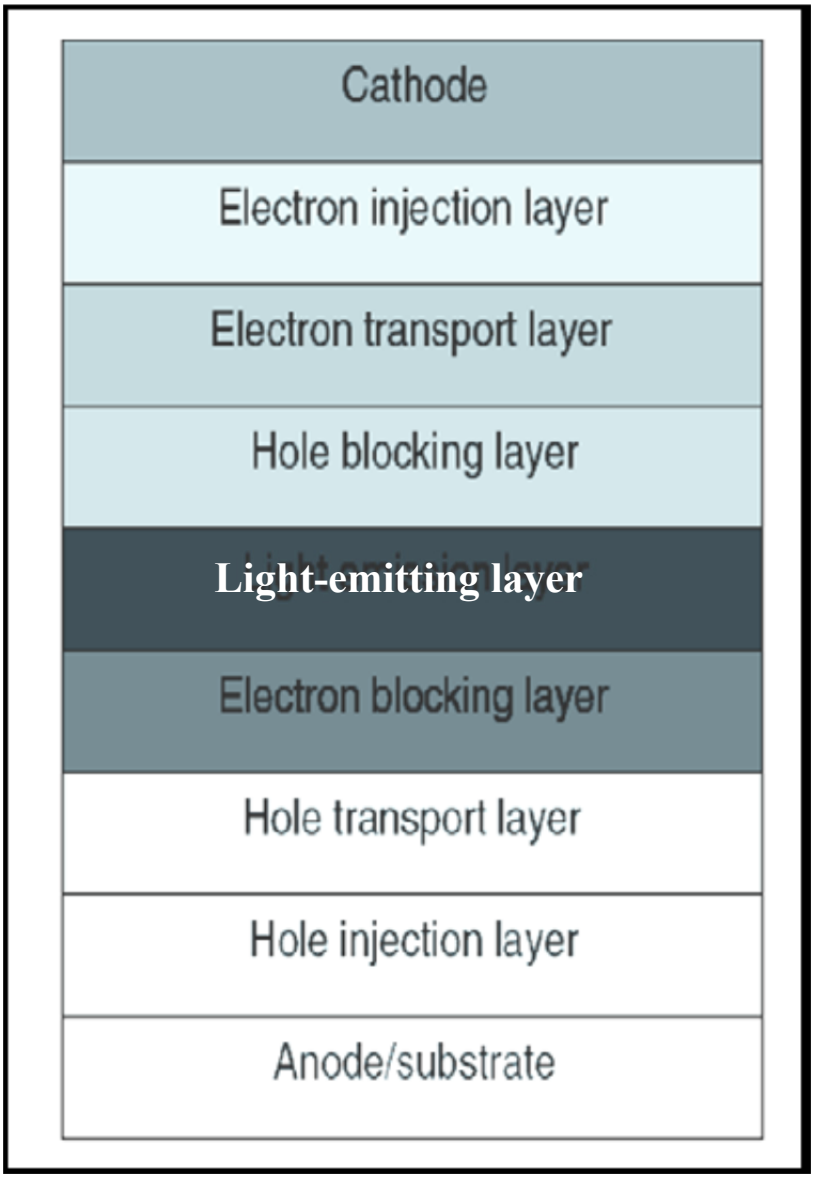

Fig. 1-9. *Device structure of multilayered SMOLEDs.*

blocks the electrons (holes) from reaching the opposite electrode and confines them to the RZ. A good HTM (ETM) is typically an efficient electron (hole) blocking material as well.

Since the exciton diffusion length is typically ~10 nm, the EML is where e^{-}-h^{+} recombination occurs and light is generated. By changing the emitter materials (EMs), the color of the OLEDs can be varied from UV to red, covering the whole visible range. For fluorescent materials, 4,4'-bis(carbazol-9-yl)biphenyl (CBP) emits in the near UV to deep violet, 4,4 '-bis(2,2 ' diphenyl vinyl)-1,1 '-biphenyl (DPVBi) in the sky-blue, Alq_3 in the green and 4-(dicyanomethylene)-2-methyl-6-julolidyl-9-enyl-4H-pyran (DCM2) in the red [42-44]. For phosphorescent materials, FIrpic emits in the sky-blue, $Ir(ppy)_3$ in the green, and PtOEP in the red [16-17,45]. Some organic materials are multifunctional. For example, Alq_3 can be both the EM [14,40,43] and ETM [40], NPD can be used as EML [46] or HTL [39], and CBP can be used as EML [42] or host material [17,35]. The chemical structures of the organic materials are shown in Fig. 1-10.

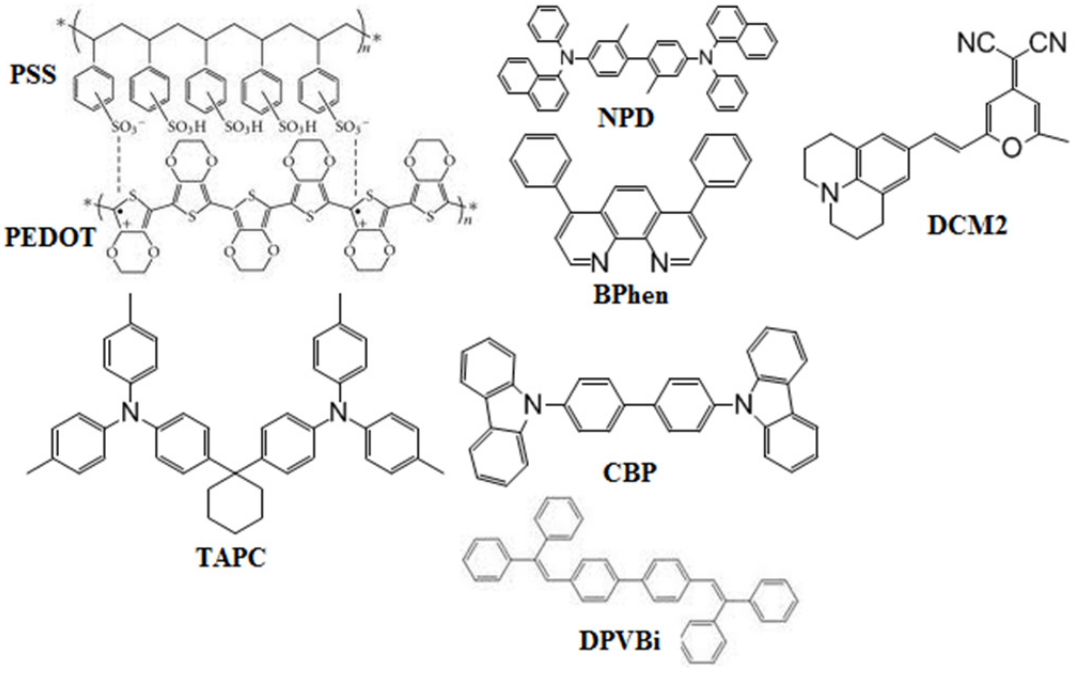

Fig. 1-10. *Chemical structure of the organic materials.*

Many other advanced OLED structures have been reported. We dwell briefly on some of these.

1) Top-emitting OLEDs (TEOLEDs)

Conventional OLEDs are mostly bottom-emitting, i.e., the light is emitted through the transparent substrate and transparent or semi-transparent bottom electrode. In TEOLEDs [47-49] the light is emitted through the transparent or semi-transparent top electrode. TEOLEDs are better suited for active-matrix applications as they can be more easily integrated with a non-transparent transistor backplane.

2) Transparent OLEDs (TOLEDs)

TOLEDs use transparent or semi-transparent electrodes. They can greatly improve contrast, making it much easier to view displays in bright sunlight [50]. This technology can be used in Head-up displays, smart windows or augmented reality applications. Novaled's OLED panel presented in Finetech Japan 2010 boasts a transparency of 60–70% [51].

3) Mixed Host and Graded Heterojunction OLEDs

Mixed host and graded junctions at the organic-organic interface have been reported to enhance the carrier injection as well as the device performance [52-56]. The lifetime of the devices fabricated with the mixed host architecture was reported to be more than 10 times the lifetime with a heterostructure scheme. Further enhancement in device performance was achieved with an emissive layer with a graded composition, i.e., the region close to the hole injection electrode is HTM rich and the region close to the electron injection electrode is ETM rich. Mixed-layer architecture was also adopted for phosphorescent devices and enhancement in device performance was demonstrated [57-58].

4) Stacking and tandem OLEDs

The concept of stacking and tandem OLEDs is to stack a set of complete OLED units on top of each other. From an electrical viewpoint, this means that several

independent OLEDs are connected in series. By doing this, the current efficiency of the device is increased because one injected charge can generate multiple photons in a stack of several OLEDs instead of only obtaining at most one photon in conventional OLEDs. And the improved current efficiency leads to longer useful lifetime. However, this comes at the cost of an increased operating voltage. But in any case, the power efficiency of such a device can be higher than for a conventional device [59-60].

5) Inverted OLEDs

In contrast to a conventional OLED, in which the anode is placed on the substrate, an inverted OLED uses a bottom cathode that can be connected to the drain end of an n-channel TFT, in particular for low cost amorphous silicon TFT backplanes used in the manufacturing of active matrix OLED (AMOLED) displays [61].

6) Indium tin oxide (ITO)-free OLEDs

ITO is the dominant material used as the transparent anode and offers many beneficial properties, such as good transparency in the visible range and good electrical conductivity. However, it is plagued by several key issues: (1) its fragility and inflexibility, which is due to its ceramic nature that limits the processing advantages of organic materials, (2) its relatively rough surface, which can cause contact problems and usually leads to unwanted energy loss, (3) its relatively high refraction index $n_{ITO} \sim 2.0$, which causes unwanted total internal reflection (TIR) at the ITO/glass substrate interface. Thus, these issues raise a demand for alternatives, and conducting polymers, carbon nanotubes, graphene, thin metal layers and printable metal grids are being investigated for this purpose. The motivation for using these alternatives is to lowering the fabrication cost, improving the device performance and also expanding the OLEDs use in e.g., flexible displays [62-67].

Working principle of OLEDs

During operation, a voltage is applied across the OLED such that the anode is positive with respect to the cathode. A current of electrons flows through the device from cathode to anode, as electrons are injected into the LUMO of the ETL at the cathode and withdrawn from the HOMO of the HTL at the anode. This latter process may also be described as the injection of holes. Then holes and electrons drift through the organic layers toward each other under the influence of the external electric field. Some of these carriers recombine to form excitons. This happens in the EML and usually closer to the EML/ETL interface, because in organic semiconductors holes are generally more mobile than electrons. Some exciton decay routes are radiative, leading to light emission. The photon energy E_{photon} depends on the band gap E_g of the emitter material, in this case the difference in energy between the HOMO and LUMO. Therefore, basically, light emission from OLEDs is governed by three major electronic processes: charge injection, transport, and recombination.

The resistivity of a typical organic material is in the range of 10^{15} - 10^{20} Ωcm at low electric fields (< 10^4 V/cm), which is too high to be considered as a good electric conductor, even semiconductor. This is the reason that the total thickness of the organic layers in the OLEDs usually is ~ 100 nm. This extremely low conductivity also implies that organic semiconductors intrinsically have virtually no free charge carriers, so charge carrier injection is one major step in charge transport in OLEDs. Inefficient injection or extraction of charge will hamper the device performance. In general, there are three major theoretical approaches involved to describe the charge injection mechanism:

1) Field-assisted thermionic injection in which the carriers from the electrodes are thermally excited to overcome the potential barrier resulting from the superposition of the image charge potential and external field [68].

$$J = J_{inj} - J_{rec} = A^* T^2 e^{-\frac{\Phi_B}{kT}} e^{f^{\frac{1}{2}}} - n_0 q S(F) \qquad (1.6)$$

where $A^* = \frac{16\pi\varepsilon\varepsilon_0 k^2 N_0}{q^2}$ is the effective Richardson constant, $f = \frac{qFr_C}{kT}$ is the reduced electric field and $S = \frac{J_{rec}}{n_0 q}$ is the surface recombination velocity. At high temperatures or low injection barrier heights, thermionic emission predicts the injection of a charge carrier from a metal contact into a semiconductor if the thermal energy of the carrier is greater than the Schottky barrier height.

2) The Fowler–Nordheim (FN) tunneling injection model, in which the carriers tunnel through the potential barrier of the metal–organic (MO) contact under a high electric field [69-71]:

$$J = AF^2 e^{-\frac{8\pi\sqrt{2m^*}\Phi_B^{1.5}}{3heF}} \qquad (1.7)$$

where m^* is the effective charge carrier mass, F is the applied electric field, and $A = \frac{q^3}{8\pi h \Phi_B}$ is a rate coefficient that contains a tunneling prefactor and the rate of current back-flow. At high electric fields or high injection barrier heights, the FN model describes tunneling currents through a triangular barrier into a delocalized conduction band.

3) The thermoactivated hopping injection model, which is attributed to the hopping of carriers from the metal Fermi level into the localized states of the organic semiconductor [72-77]. The results from the model were found to successfully describe the temperature and injecting contact-dependent current–voltage characteristics in a polytetraphenylbenzidine (PTPB).

In all of these approaches, the injection process is dominated by the charge injection barriers at the interfaces between the active layers and the metal electrodes. Injection barriers can be difficult to estimate from the work function of the metal electrode and the HOMO (or LUMO) of the organic layer. Actual injection barrier heights can deviate quite strongly from the expected values. Those deviations are attributed to chemical reactions between the metal and semiconductor leading to interface dipoles [78-79], band bending [80-81], or Fermi level pinning [82]. As a rule of thumb, the currents in organic devices with injection barriers greater than 0.25–0.3 eV [19] at zero field are found to be 'injection limited', i.e., the maximum current is determined by the injection process of the charge carriers into the device, as opposed to 'bulk limited' (or space-charge limited) devices (see below).

The charge carrier mobilities in organic semiconductors are typically low and Ohm's law is followed at a very low V. If the injection barriers are small, and the electrode can supply more carriers per unit time than can be transported through the bulk, the current is limited by the latter and can be described using the theory of space-charge-limited currents (SCLC) [19, 83–85]. Such organic/metal contacts are said to be Ohmic contacts

$$J_{SCL} = \frac{9}{8}\frac{\varepsilon\varepsilon_0\mu V^2}{L^3} \qquad (1.8)$$

Here, ε_0 is the permittivity of free space, ε is the relative dielectric constant, μ is the microscopic mobility of the carriers, L is the thickness of the organic film, and V is the voltage.

In the presence of discrete traps, situated at energy E_t below the LUMO level, a modified form of Eq. (1.8) may be derived as follows. If the proportion of traps that

are empty is not too small, then the proportion of the total charge which is free is given by

$$\theta_0 = \frac{n_f}{n_t} = \frac{N_{eff}}{N_0}\left(\frac{2.7qr_0}{3lkT}\right)^{3l}\left(\frac{V}{L}\right)^{3l}e^{-\frac{E_t}{kT}} \qquad (1.9)$$

$$J_{SCL} = \frac{9}{8}\theta_0\frac{\varepsilon\varepsilon_0\mu V^2}{L^3} = \frac{\varepsilon\varepsilon_0\mu}{2+3l}\left(\frac{3+3l}{2+3l}\right)^{2+3l}\theta_0\frac{V^2}{L^3} \qquad (1.10)$$

where l is a characteristic distribution parameter which can be replaced by a characteristic distribution temperature $T_c = lT$, N_{eff} is the effective density of states in the transport band, N_0 is the concentration of macrotraps, and r_0 is the macrotrap radius. Then the transition from the low- to high-field regions of the current occurs at

$$V_{tr} = \frac{3lkTL}{2.7er_0}\left(\frac{9l}{8}\right)^{\frac{1}{3l}}\frac{\left(\frac{2}{l}+3\right)^{1+\frac{1}{l}}}{\left(\frac{3}{l}+3\right)^{1+\frac{2}{3}l}} \qquad (1.11)$$

The charge carrier drift mobility μ is obviously an important parameter in organic semiconductors. Unlike their behavior in crystalline semiconductors, μ is electric field-dependent and thermally activated, probably due to the fact that carrier transport is mainly through hopping in a disordered material.

$$\mu(F,T) = \mu(0,T)e^{\gamma F^{1/2}} \qquad (1.12)$$

where $\mu(0,T)$ is the zero-field mobility and γ is an empirically determined coefficient. The hole mobility μ_h is typically 10^{-7} - 10^{-3} cm^2/Vs, and the electron mobility μ_e is usually 1 - 2 orders of magnitude lower. Such low mobility is due to the disorder in the amorphous or polycrystalline material. The dependence $\ln(\mu) \propto F^{1/2}$ is commonly observed experimentally by time-of-flight (TOF) [86-87] and other methods [88-89], and it follows the Poole–Frenkel model [90], which describes charge transport and trapping arises in the presence of the carrier traps. The field dependence of μ is explained by the spatial and energetic disorder of the hopping sites in a disordered material containing permanent electric dipole moments [91].

Another commonly observed experimental feature is the strong dependence of μ on the charge carrier concentration and on trapping effects. Recently, two advanced models based on hopping transport in a system with a Gaussian density of states (DOS) addressed this dependence [92-94]. According to these models, μ can be expressed as:

$$\mu(T,p,F) \approx \mu(T,p)f(T,F) \qquad (1.13)$$

where $\mu(T,p) = \mu_0 c_1 e^{-c_2\hat{\sigma}^2} e^{[\frac{1}{2}(\hat{\sigma}^2-\hat{\sigma})(2pa^3)^\delta]}$

and $f(T,p) = e^{\{0.44(\hat{\sigma}^{1.5}-2.2)[\sqrt{1+0.8\left(\frac{Fqa}{\sigma}\right)^2}-1]\}}$.

The p is the charge-carrier density, a is the lattice constant, $\alpha = 10/a$ is the inverse localization length, $\hat{\sigma} = \sigma/k_BT$, and σ is the width of the Gaussian.

The charge recombination process can be defined as e^--h^+ fusion to an exciton. The initial recombination (IR), or geminate recombination (GR), and volume-controlled recombination (VR) can be distinguished on the basis of the charge carriers' origin [95]. GR is the recombination process following the initial carrier separation from an exciton, forming a nearest-neighbor charge-transfer (CT) state. It typically occurs as part of intrinsic photoconduction.

In OLEDs, the holes and electrons are injected separately from the anode and cathode and transported into the organic layers, so the carriers are statistically independent of each other. In this case, the VR takes place, and this recombination process is kinetically bimolecular. The classic treatment of VR recombination can be related to the notion of the recombination time, τ_{rec}. The recombination time represents a combination of the carrier motion time (τ_m, the time to get the carriers within the capture radius) and the elementary capture time (τ_c), $\tau_{rec}^{-1} = \tau_m^{-1} + \tau_c^{-1}$.

If $\tau_m \gg \tau_c \rightarrow \tau_{rec} \approx \tau_c$, it is a Langevin-like volume recombination; if $\tau_c \gg \tau_m \rightarrow \tau_{rec} \approx \tau_{m,,}$ it is a Thomson-like volume recombination [96-97]. These two also can be distinguished by comparing the mean free path for optical phonon emission (λ) with the average distance $4r_{Ons}/3$ across a sphere of critical radius r_{Ons} [98-99]. when $\lambda >> r_{Ons}$, it is the Thomson-like case which assumes the recombination rate to be limited by the phonon emission process. When $\lambda << r_{Ons}$ it is the Langevin-like mechanism. Because of low μ in organic semiconductors, $\lambda \cong 1$ nm is clearly much lower than $r_{Ons} \cong 15$ nm (assuming the refractive index n ~ 2 so $\varepsilon \sim 4$), strongly suggesting a Langevin-like model to be appropriate to describe the recombination process.

Measuring the efficiency of OLEDs

As any other emerging technology, there are several standard methods for measuring and quoting device efficiency, which provide a basis for valid comparison of different devices and material properties, thereby helping to clearly identify real advances.

Because most OLEDs emit light in the visible range, which is detected by the human eye, the human eye response, or *photopic response*, directly affects the luminous efficacy. In other words, the perceived brightness of the OLED depends strongly on its emission spectrum. Thus, it takes more energy in the blue or red bands to create the same sensation of brightness as in the yellow-green region. The photosensitivity of the human eye peaks at 555 nm and vanishes above ~700 nm and below ~390 nm, as seen in Fig. 1-11.

The internal quantum efficiency η_{int} is the ratio of the total number of photons generated within the structure to the number of electrons injected, can be expressed as [100]

$$\eta_{int} = \gamma \eta_{exc} \phi_{PL} \qquad (1.14)$$

where γ is the electron–hole charge balance factor (a measure of the balance between h^+ and e^- injection, and of the probability that each of them will recombine with the other; it is very difficult to measure, but it is probably close to 1 in relatively efficient

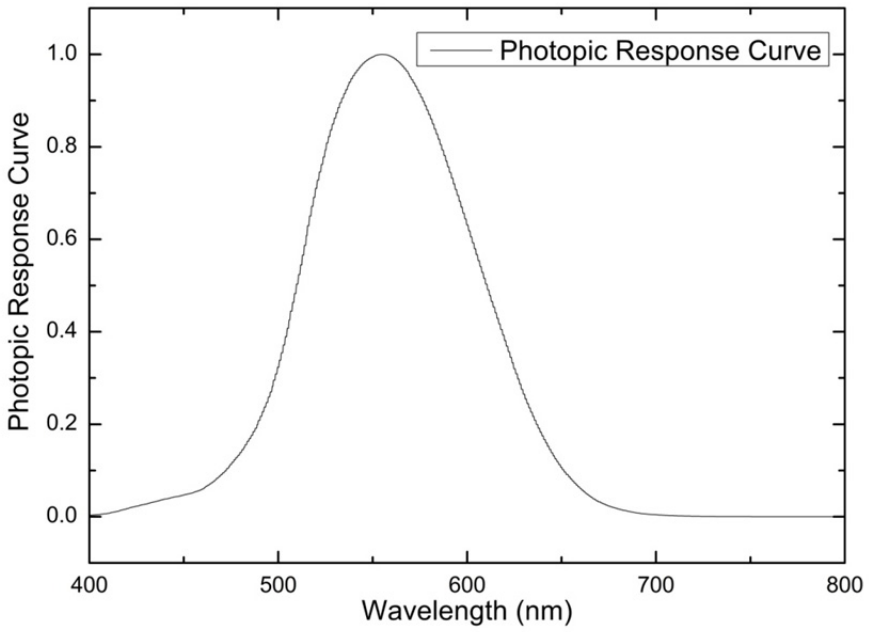

Fig. 1-11. *Photopic response of human eyes.*

OLEDs), η_{exc} is the fraction of total number of excitons formed which result in radiative decay (η_{exc} = 0.25 and 1 for fluorescence, and phosphorescence-based OLED materials, respectively), and ϕ_{PL} is the intrinsic quantum efficiency for radiative decay (including both fluorescence and phosphorescence) [23,62]. Hence, from Eq. (1.14) we see that for fluorescent OLEDs, $\eta_{int,max}$ = 25% and for phosphorescent OLEDs, $\eta_{int,max}$ = 100%.

The external quantum efficiency η_{ext} is defined as the ratio of the number of photons emitted by the OLED into the viewing direction to the number of electrons injected. η_{ext} is related to η_{int} by the following relation [23,62]:

$$\eta_{ext} = \eta_{int}\eta_{coupling} \qquad (1.15)$$

where $\eta_{coupling}$ is the outcoupling efficiency (i.e. the fraction of the photons which are emitted from the front surface of the device). Assuming isotropic emission in the organic layer and a perfectly reflecting cathode, the fraction of generated light escaping from the substrate is [23,62,101-103]

$$\eta_{coupling} = \frac{1}{\xi n_{org}^2} \qquad (1.16)$$

where n_{org} is the refractive index of the organic layers and ξ is a constant that depends on the radiative exciton dipole orientation and the geometry of the OLED device. For most organic materials $n_{org} \sim 1.7$ and for randomly oriented dipoles $\xi \approx 2$, so in these cases $\eta_{coupling} \sim 17\%$. According to classical ray optics theory about 80% of generated light is lost in waveguided modes due to the glass substrate ($n_{glass} = 1.55$) and ITO ($n_{ITO} \approx 2.0$), which means that the majority of the light is either trapped inside the glass substrate and device, or emitted from the glass edges the device [62,102-105].

The luminous efficiency η_L, in candelas per amp [Cd/A], is equivalent to η_{ext}, with the exception that η_L weights the photons according to the photopic response of the eye. In this case, we define:

$$\eta_L = \frac{L}{J_{OLED}} \qquad (1.17)$$

where L is the brightness (in [Cd/m^2]) and J_{OLED} is the current density (in [A/m^2]) of the OLEDs. η_{ext} can be calculated from η_L as follows [106]:

$$\eta_{ext} = \frac{\pi q}{k_m hc}\eta_L \frac{\int_{380}^{780} g(\lambda)\lambda d\lambda}{\int_{380}^{780} g(\lambda)k(\lambda)d\lambda} \qquad (1.18)$$

where $g(\lambda)$ is the relative EL intensity wavelength λ and $k(\lambda)$ is the Commision International de l'Eclairage chromaticity (CIE) standard Photopic Luminous Efficiency Function.

The most frequently used efficiency unit is the power efficiency η_P, in lumens per watt [lm/W]. η_P is ratio of luminous power emitted in the forward direction, L_P [lm], to the total electrical power required to drive the OLEDs at a particular voltage V. It can be written as [106]:

$$\eta_P = \frac{L_P}{I_{OLED}V} = \frac{\pi\eta_L}{V} \qquad (1.19)$$

The η_P of the state-of-the-art OLEDs already exceeds the benchmark 100 lm/W, which is higher than the 60–70 lm/W of fluorescent tubes.

Applications of OLEDs

OLED technology is realized in commercial applications such as flat-panel displays (FPDs) and solid-state lighting (SSL).

1) Flat-panel displays:

I. Small screens:

OLEDs used as small screens in mobile phones, portable digital media players, car radios, digital cameras, and others. Such portable applications favor the high light output of OLEDs for readability in sunlight and their low power drain. OLEDs are also used in many Motorola and Samsung cell phones, as well as some HTC, LG and Sony Ericsson models [107]. Nokia has also recently introduced some OLED products including the N85 and the N86 8MP, both of which feature an AMOLED display. OLED technology can also be found in digital media players such as the Creative ZEN V, the iriver clix, the Zune HD, and the Sony Walkman X Series.

II. TVs

OLED-TVs are commercially available now. DuPont stated in a press release in May 2010 that they can produce a 50” OLED TV in two minutes with a new printing technology [108].

2) Solid-state lighting:

Applications in flexible signs and lighting are also being developed [109]. Philips Lighting has made OLED lighting samples under the brand name 'Lumiblade,' which are available for sale online [110], and Siemens Osram offers the Orbeus white OLED panels for sale.

Challenges of OLEDs

Although the first OLED-TV (Sony XEL-1) was released in 2008, OLED technology still faces many challenges:

1) Current costs

OLED manufacturing currently requires process steps that make it extremely expensive, especially for thermal vacuum evaporated OLEDs [26-29].

2) Lifespan

The biggest technical problem for OLEDs was the limited lifetime of the devices [111]. In particular, blue OLEDs have achieved a lifetime of ~14,000 hours to half original brightness (five years at 8 hours a day) when used for flat-panel displays. This is lower than the typical lifetime of LCDs, LEDs or plasma displays—each currently rated for 25,000–40,000 hours to half brightness, depending on manufacturer and model [112-113].

3) Color balance issues

As blue emitters degrade significantly more rapidly than green or red emitters, then blue light output decreases relative to the other colors. This variation in the differential color output changes the color balance of the display and is much more noticeable than a decrease in overall luminance [114].

4) Efficiency of blue OLEDs

Improvement to the efficiency and lifetime of blue OLEDs is vital to the success of OLEDs as replacements for LCD technology.

5) Water damage

Water rapidly damages the organic materials of the displays. Therefore, improved sealing processes are critical for practical manufacturing. Water damage may especially limit the longevity of more flexible displays [115].

6) Outdoor performance

As an emissive display technology, OLEDs rely completely upon converting electricity to light. The metallic cathode in an OLED acts as a mirror, with reflectance approaching 80%, leading to poor readability in bright ambient light such as outdoors.

References

[1] A. Bernanose, M. Comte, and P. Vouaux, J. Chim. Phys. **50**, 64 (1953).

[2] A. Bernanose and P. Vouaux, J. Chim. Phys. **50**, 261 (1953).

[3] A. Bernanose, J. Chim. Phys. **52**, 396 (1955).

[4] A. Bernanose and P. Vouaux, J. Chim. Phys. **52**, 509 (1955).

[5] H. Kallmann and M. Pope, J. Chem. Phys. **32**, 300 (1960).

[6] H. Kallmann and M. Pope, Nature **186**, 4718 (1960).

[7] P. Mark and W. Helfrich, J. Appl. Phys. **33**, 205 (1962).

[8] M. Pope, H. P. Kallmann and P. Magnante, J. Chem. Phys. **38**, 2042 (1963).

[9] W. Helfrich and W. Schneider, Phys. Rev. Lett. **14**, 229 (1965).

[10] R. Partridge, Polymer **24**, 733 (1983).

[11] R. Partridge, Polymer **24**, 739 (1983).

[12] R. Partridge, Polymer **24**, 748 (1983).

[13] R. Partridge, Polymer **24**, 755 (1983).

[14] C. W. Tang and S. A. Vanslyke, Appl. Phys. Lett. **51**, 913 (1987).

[15] J. H. Burroughes, D. D. C. Bradley, A. R. Brown, R. N. Marks, K. MacKay, R. H. Friend, P. L. Burns and A. B. Holmes, Nature **347**, 539 (1990).

[16] M. A. Baldo, D. F. O'Brien, Y. You, A. Shoustikov, S. Sibley, M. E. Thompson and S. R. Forrest, Nature **395**, 151 (1998).

[17] M. A. Baldo, S. Lamansky, P. E. Burrows, M. E. Thompson and S. R. Forrest, Appl. Phys. Lett. **75**, 4 (1999).

[18] C. Adachi, M. A. Baldo, M. E. Thompson and S. R. Forrest, J. Appl. Phys. **90**, 5048 (2001).

[19] *Electronic processes in organic crystals and polymers*, 2nd ed., edited by M. Pope and C. E. Swenberg (Oxford University Press, New York, 1999).

[20] A. R. Brown, K. Pichler, N. C. Greenham, D. D. C. Bradley, R. H. Friend and A. B. Holmes, Chem. Phys. Lett. **210**, 61 (1993).

[21] M. A. Baldo, D. F. O'Brien, M. E. Thompson and S. R. Forrest, Phys. Rev. B **60**, 14422 (1999).

[22] T. Tsutsui, M.-J. Yang, M. Yahiro, K. Nakamura, T. Watanabe, T. Tsuji, Y. Fukuda and T. Wakimoto, Jpn. J. Appl. Phys. **38**, L1502 (1999).

[23] S. R. Forrest, D. D. C. Bradley and M. E. Thompson, Adv. Mater. **15**, 1043

(2003).

[24] X. Yang, D. Neher, D. Hertel and T. Daubler, Adv. Mater. **16**, 161 (2004).

[25] D. F. O'Brien, M. A. Baldo, M. E. Thompson and S. R. Forrest, Appl. Phys. Lett. **74**, 442 (1999).

[26] C. Adachi, M. A. Baldo, S. R. Forrest and M. E. Thompson, Appl. Phys. Lett. **77**, 904 (2000).

[27] J. S. Huang, M. Pfeiffer, A. Werner, J. Blochwitz, K. Leo and S. Y. Liu, Appl. Phys. Lett. **80**, 139 (2002).

[28] B.W. D'Andrade, M.E. Thompson and S.R. Forrest, Adv. Mater. **14**, 147 (2002).

[29] M. C. Gather, A. Köhnen and K. Meerholz, Adv. Mater. **23**, 2 (2011).

[30] J. Huang, G. Li, E. Wu, Q. Xu and Y. Yang, Adv. Mater. **18**, 114 (2006).

[31] S.R. Forrest, Nature **428**, 911 (2004).

[32] P. S. Vincett, W. A. Barlow, R. A. Hann and G. G. Roberts, Thin Solid Films **94**, 171 (1982).

[33] A. R. Brown, D. D. C. Bradley, J. H. Burroughes, R. H. Friend, N. C. Greenham, P. L. Burn, A. B. Holmes and A. Kraft, Appl. Phys. Lett. **61**, 2793 (1992).

[34] S. A. Choulis, V. E. Choong, M. K. Mathai and F. So, Appl. Phys. Lett. **87**, 113503 (2005).

[35] Z. B. Wang, M. G. Helander, J. Qiu, D. P. Puzzo, M. T. Greiner, Z. W. Liu and Z. H. Lu, Appl. Phys. Lett. **98**, 073310 (2011).

[36] Z. T. Xie, W. H. Zhang, B. F. Ding, X. D. Gao, Y. T. You, Z. Y. Sun, X. M. Ding and X. Y. Hou, Appl. Phys. Lett. **94**, 063302 (2009).

[37] P. Piromreun, H. Oh, Y. Shen, G. G. Malliaras, J. C. Scott and P. J. Brock, Appl. Phys. Lett. **77**, 2403 (2000).

[38] T. Matsushima, G.-H. Jin, and H. Murata, J. Appl. Phys. **104**, 054501 (2008).

[39] Y. Zheng, S-H. Eom, N. Chopra, J. Lee, F. So, and J. Xue, Appl. Phys. Lett. **92**, 223301 (2008).

[40] G. Xie, Y. Meng, F. Wu, C. Tao, D. Zhang, M. Liu, Q. Xue, W. Chen and Y. Zhao, Appl. Phys. Lett. **92**, 093305 (2008).

[41] S.-H. Eom, Y. Zheng, N. Chopra, J. Lee, F. So and J. Xue, Appl. Phys. Lett. **93**, 133309 (2009).

[42] L. Zou, V. Savvate'ev, J. Booher, C.-H. Kim and J. Shinar, Appl. Phys. Lett. **79**, 2282 (2001).

[43] Z. Gan, Y. Tian, D. W. Lynch, J-H. Kang, Q-H. Park and J. Shinar, J. Appl. Phys. **106**, 094502 (2009).

[44] K. O. Choen and J. Shinar, Appl. Phys. Lett. **81**, 1783 (2002).

[45] N. Chopra, J. S. Swensen, E. Polikarpov, L. Cosimbescu, F. So and A. B. Padmaperuma, Appl. Phys. Lett. **97**, 033304 (2010).

[46] H. Mu, I. Reddy, J. Hunt, P. Severs and S. Patil, J. Phys. D: Appl. Phys. **43** 195103 (2010)

[47] V. Bulovic, G. Gu, P. E. Burrows, M. E. Thompson and S. R. Forrest, Nature **380**, 29 (1996).

[48] G. Parthasarathy, P. E. Burrows, V. Khalfin, V. G. Kozlov and S. R. Forrest, Appl. Phys. Lett. **72**, 2138 (1998).

[49] L. S. Hung, C. W. Tang, M. G. Mason, P. Raychaudhuri and J. Madathil, Appl. Phys. Lett. **78**, 544 (2001).

[50] M. E. Thompson, S. R. Forrest and P. Burrows, US patent (1999).

[51] Novaled. Retrieved on 2011-10-04.

[52] C. Chen, T. Cho, C. Wu, H. Yu and T. Luh, Appl. Phys. Lett. **81**, 1570 (2002).

[53] B. J. Chen, X. W. Sun, T. K. S. Wong, X. Hu and A. Uddin, Appl. Phys. Lett. **87,** 063505 (2005).

[54] A. B. Chwang, R. C. Kwong and J. J. Brown, Appl. Phys. Lett. **80**, 725 (2002).

[55] Y. Shao and Y. Yang, Appl. Phys. Lett. **83** 2453 (2003).

[56] A. W. D. Van Der Gon, J. Birgerson, M. Fahlman and W. R. Salaneck, Org. Electron. **3**, 111 (2002).

[57] C. H. Hsiao, Y. H. Chen, T. C. Lin, C. C. Hsiao and J. H. Lee, Appl. Phys. Lett. **89**, 163511 (2006).

[58] T. W. Lee, M. G. Kim, S. Y. Kim, S. H. Park, O. Kwon, T. Noh and T. S. Oh, Appl. Phys. Lett. **89**, 123505 (2006).

[59] T. W. Lee, T. Noh, B. K. Choi, M. S. Kim, D. W. Shin and J. Kido , Appl. Phys. Lett. **92**, 043301 (2008).

[60] J. Kido, Dig. Tech. Pap.-Soc. Inf. Disp. Int. Symp. **39**, 931 (2008).

[61] T.-Y. Chu, J.-F. Chen, S.-Y. Chen, C.-J. Chen and C. H. Chen, Appl. Phys. Lett. **89**, 053503 (2006).

[62] K. Saxena, V. K. Jain and D. S. Mehta, Opt. Mater. **32**, 221 (2009).

[63] D. S. Hecht, L. B. Hu and G. Irvin, Adv. Mater. **23**, (2011).

[64] A. M. Alfantazi and R. R. Moskalyk, Miner. Eng. **16**, 687 (2003).

[65] M. A. Green, Prog. Photovoltaics **17**, 347 (2009).

[66] D. R. Cairns, R. P. Witte, D. K. Sparacin, S. M. Sachsman, D. C. Paine, G. P. Crawford and R. R. Newton, Appl. Phys. Lett. **76**, 1425 (2000).

[67] D. R. Cairns and G. P. Crawford, Proc. IEEE **93**, 1451 (2005).

[68] J. C. Scott and G. G. Malliaras, Chem. Phys. Lett. **299**, 115 (1999).

[69] R. H. Fowler and L. Nordheim, Proc. Roy. Soc. **121**, 626 (1928).

[70] I. D. Parker, J. Appl. Phys. **75**, 1658 (1995).

[71] Z. Chiguvare, J. Parisi and V. Dyakonov, J. Appl. Phys. **94**, 2440 (2003).

[72] M. A. Abkowitz, H. A. Mizes and J. S. Facci, Appl. Phys. Lett. **66**, 1288 (1995).

[73] E. M. Conwell and M. W. Wu, Appl. Phys. Lett. **70**, 1867 (1997).

[74] V. I. Arkhipov, E. V. Emelianova, Y. H. Tak and H. Bässler, J. Appl. Phys. **84**, 848 (1998).

[75] U. Wolf, V. I. Arkhipov and H. Bässler, Phys. Rev. B **59**, 7507 (1999).

[76] V. I. Arkhipov, U. Wolf, and H. Bässler, Phys. Rev. B **59**, 7514 (1999).

[77] S. Barth, U. Wolf, H. Bässler, P. Müller, H. Riel, H. Westweber, P. F. Seidler and W. Rieß, Phys. Rev. B **60**, 8791 (1999).

[78] S. Narioka, H. Ishii, D. Yoshimura, M. Sei, Y. Ouchi, K. Seki, S. Hasegawa, T. Miyazaki, Y. Harima and K. Yamashita, Appl. Phys. Lett. **67**, 1899 (1995).

[79] H. Ishii, K. Sugiyama, E. Ito and K. Seki, Adv. Mater. **11**, 605 (1999).

[80] T. Shimada, K. Hamaguchi, A. Koma and F.S. Ohuchi, Appl. Phys. Lett. **72**, 1869 (1998).

[81] R. Schlaf, P. G. Schroeder, M. W. Nelson, B. A. Parkinson, P. A. Lee, K. W. Nebesny and N. R. Armstrong, J. Appl. Phys. **86**, 1499 (1999).

[82] J. M. Barathan and Y. Yang, J. Appl. Phys. **84**, 3207 (1998).

[83] *Electronic Processes in Ionic Crystals*, 2nd ed., edited by N. F. Mott and R. W. Gurney (Oxford University Press, Oxford, 1948).

[84] M. A. Lampert, Phys. Rev. **103**, 1648 (1956).

[85] *Current injection in solids,* edited by M. A. Lampert and P. Mark (Academic Press, New York, 1970).

[86] E. M. Horsche, D. Haarer and H. Scher, Phys. Rev. B **35**, 1273 (1987).

[87] H. Meyer, D. Haarer, H. Naarmann and H.H. Höhold, Phys. Rev. B **52**, 2587 (1995).

[88] P. W. M. Blom, M. J. M. de Jong and J. J. M. Vleggaar, Appl. Phys. Lett. **68**, 3308 (1996).

[89] H. C. F. Martens, H. B. Brom and P. W. M. Blom, Phys. Rev. B **60**, R8489 (1999).

[90] J. Frenkel, Phys. Rev. **54**, 647 (1937).

[91] S. V. Novikov, D. H. Dunlap, V. M. Kenkre, P. E. Parris and A. V. Vannikov, Phys. Rev. Lett. **81**, 4472 (1998).

[92] R. Schmechel, Phys. Rev. B **66**, 235206 (2002).

[93] R. Schmechel, J. Appl. Phys. **93**, 453 (2003).

[94] W. F. Pasveer, J. Cottaar, C. Tanase, R. Coehoorn, P. A. Bobbert, P. W. M. Blom, D. M. de Leeuw and M. A. J. Michels, Phys. Rev. Lett. **94**, 206601 (2005).

[95] J. Kalinowski, Mol. Cryst. Liq. Cryst. **355**, 231 (2001).

[96] P. Langevin, Ann. Chem. Phys. **28**, 433 (1903).

[97] J. J. Thomson, Philos. Mag. **47**, 337 (1924).

[98] M. Lax, Phys. Rev. **119**, 1502 (1960).

[99] R. Morris and M. Silver, J. Chem. Phys. **50**, 2969 (1969).

[100] *Physics of Semiconductor Devices,* 3rd ed., edited by S. M. Sze and K. K. Ng (Wiley, New York 2007).

[101] N. K. Patel, S. Cinà and J. H. Burroughes, IEEE J. Select. Top. Quant. Electron. **8**, 346 (2002).

[102] D.S. Mehta and K. Saxena, Proc. 9th Asian Symp. Inf. Disp. (ASID-06), 198 (2006).

[103] S. R. Forrest, Org. Electron. **4,** 45 (2006).

[104] G. Gu, D. Z. Garbuzov, P. E. Burrows, S. Venkatesh, S. R. Forrest and M. E. Thompson, Opt. Lett. **22**, 396 (1997).

[105] J.-S. Kim, P. K. H. Ho, N. C. Greenham and R. H. Friend, J. Appl. Phys. **88**, 1073 (2000).

[106] H. Li, C. Zhang, D. Li and Y. Duan, J. Lumin. **122**, 626 (2007).

[107] "OLEDs Replacing LCDs in Mobile Phones" www.edn.com, Retrieved on 2007-07-28.

[108] "DuPont Creates 50 inches OLED in Under 2 Minutes" www.tomsguide.com, Retrieved on 2010-06-10.

[109] "Start-up creates flexible sheets of light", www.CNet.com, Retrieved on 2008-07-20.

[110] "Philips Lumiblades", www.lumiblade.com, Retrieved on 2009-08-17.

[111] "OLED TV estimated lifespan shorter then (sic) expected", www.hdtvinfo.eu.

[112] "HP Monitor manual: CCFL-Backlit LCD", www.Webcitation.org, Retrieved on 2011-10-04.

[113] "Viewsonic Monitor manual. LED-Backlit LCD", www.Webcitation.org, Retrieved on 2011-10-04.

[114] "Ageless OLED", www.digidelve.com, Retrieved on 2009-11-16.

[115] "OLED Sealing Process Reduces Water Intrusion and Increases Lifetime" www.gtresearchnews.gatech.edu.

Chapter 2. Introduction to Optically-Detected Magnetic Resonance (ODMR)

Luminescence-quenching processes

OLED technology has attracted increased attention due to its potential to realize very high efficiencies [1]. Efficiency, however, decreases rapidly with increasing OLEDs current density *J*, as shown in Fig. 2-1, especially for phosphorescent OLEDs (PHOLEDs). This behavior is referred to as efficiency roll-off [2], which is attributed to a number of luminescence-quenching mechanisms:

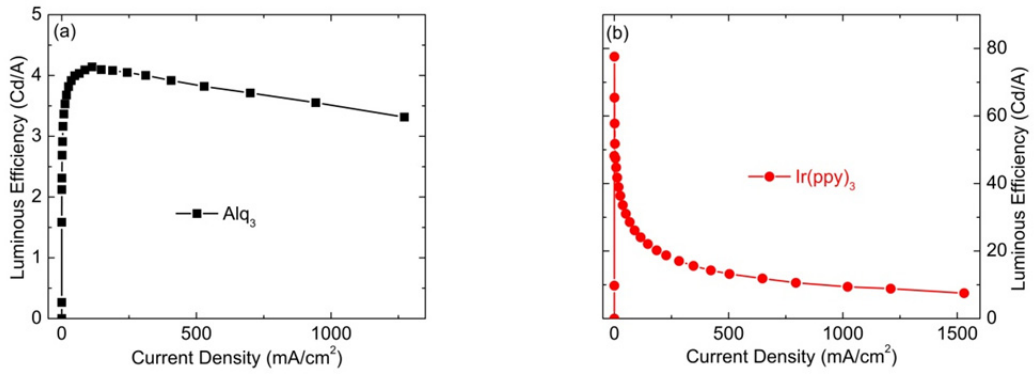

Fig. 2-1. *Luminous efficiency vs. current density in devices with (a) Alq_3 and (b) $Ir(ppy)_3$ as the emitter.*

1) SEs – TEs quenching [3,4]:

$$S_1 + T_1 \rightarrow T_1^* + phonons \qquad (2.1)$$

where SEs are singlet excitons (S_1), TEs are triplet excitons (T_1), and T_1^* is a higher energy state in the TE manifold.

2) SEs – polarons quenching. This quenching can occur by either of two mechanisms:

a) Direct annihilation of the SEs, i.e.,

$$S_1 + p^{\pm} \rightarrow S_0 + p^{\pm^*} + phonons \qquad (2.2)$$

where $p^{\pm}$ is a (typically trapped) negative or positive polaron and $p^{\pm^*}$ is a high-energy (typically transport) state of the polaron.

b) Polaron-induced dissociation of the SEs, i.e.,

$$S_1 + p^{\pm} \rightarrow p^{+} + p^{-} + p^{\pm} + phonons \qquad (2.3)$$

This polaron-induced dissociation results from the electric field created by the polaron, which enhances SE dissociation [5].

3) SEs – bipolarons (trions) quenching. As in the case of SEs – polarons quenching, this could be either:

a) Direct annihilation of the SEs, i.e.,

$$S_1 + bp^{--/++} \rightarrow S_0 + bp^{--/++^*} + phonons \qquad (2.4)$$

b) Dissociate the SE into a positive+negative polaron pair, i.e.,

$$S_1 + bp^{--/++} \rightarrow p^{+} + p^{-} + bp^{--/++} + phonons \qquad (2.5)$$

where $bp^{--/++^*}$ is a high energy state of the doubly positive bp^{++} or negative bp^{--} charged bipolarons, and a trion is a bipolaron stabilized by a counterpolaron or counterion [6].

4) TEs – polarons quenching (TPQ) [3,6-9]:

$$T_1 + p^{\pm} \rightarrow S_0 + p^{\pm^*} + phonons \qquad (2.6)$$

5) TEs – TEs annihilation (TTA) [10-11]:

$$T_1 + T_1 \rightarrow S_1 + S_0 + phonons \qquad (2.7)$$

In this case, two TEs interact (usually upon collision) to produce one excited SE and another ground state SE. This is often, but not always, followed by delayed fluorescence [3,12]. In some unusual cases, such as for 5,6,11,12-tetraphenyl-

tetracene (rubrene) and similar molecules [13], where the energy of E_{S_1} is about twice the E_{T_1}, fusion of two T_1 back to S_1 and S_0 is relatively highly efficient.

Among all these processes, because of the spin $\boldsymbol{S} = 0$ for the SEs, processes 1) – 3) are all spin-independent and processes 4) and 5) are strongly spin-dependent.

In a typical high-field optically- and electrically-detected magnetic resonance (ODMR and EDMR, respectively) experiment, *microwave-induced changes in an optical or electrical quantity are monitored as the sample* (a thin film, powder, solution, light-emitting device, solar cell, photodiode, etc.) *is subjected to magnetic resonance conditions*. As the polarons' and TEs' spin $\boldsymbol{S} \neq 0$, magnetic resonance conditions may affect their spin sublevel populations. Since different spin sublevel states may decay at different rates, magnetic resonance conditions may change their overall populations and hence yield a detectable microwave-induced change Δ. By studying these observed changes vs. temperature T, microwave chopping power p_{M}, microwave chopping frequency f_M, and excitation power p_{Laser} or current density J, a better understanding of the underlying relationship between the luminescence-quenching mechanisms and the device performance is achieved. This is especially the case for those mechanisms involved dark excitations-species, and subsequently helps in fabricating more promising OLEDs.

According to the different optical or electrical quantities that are monitored experimentally, ODMR is divided into:

1) photoinduced-absorption (PA)-detected magnetic resonance (PADMR), where the photoinduced-absorption of π – conjugated materials is monitored.

2) Photoluminescence (PL)-detected magnetic resonance (PLDMR), where the photoluminescence of π – conjugated materials, typically excited by a laser, is monitored.
3) Electroluminescence (EL)-detected magnetic resonance (ELDMR), where the EL of OLEDs is monitored.

For EDMR, usually the current flow through the device is monitored; depending on the source of the current, there are two EDMR types:

1) Current- or Conductivity-detected magnetic resonance (CDMR) and
2) Photoconductivity-detected magnetic resonance (PCDMR)

Introduction to PLDMR

PLDMR is an extension of electron-spin resonance (ESR) developed in the 60s [14]. It can detect a very small change in the PL of the π – conjugated materials that is induced by the magnetic resonance conditions (typically $\frac{\Delta I_{PL}}{I_{PL}} < 10^{-3}$). It is a very sensitive technique and is particularly useful for studying dark excitations—species that are normally incapable of PL, such as spin-1/2 polarons and spin-1 TEs.

Fig. 2-2 shows a schematic of the X-band 9.35 GHz PLDMR spectrometer. The samples, π – conjugated luminescent films, were sealed in an evacuated quartz tube. They were placed in the quartz finger dewar inserted into the microwave cavity. The cavity was optically-accessible through slits in the cavity wall. That cavity was positioned between the poles of a DC magnet and connected to a microwave power supply and bridge. A laser beam was directed through the slits onto the sample, and the PL was collected directly by a condensing lens outside the optical access of the cavity and focused either on the entrance slit of a monochromator or directly onto a

photomultiplier tube (PMT) or Si photodiode (PD). Besides the DC magnetic field H and the exciting laser power, the sample was also subjected to a microwave field, typically chopped at a frequency 50 Hz < f_M < 10 kHz. The signal from the PMT or Si PD was connected to the input signal channel of a lockin amplifier, which was referenced by the waveform used to chop the microwaves. Hence, the lockin amplifier output was directly proportional to the microwave-induced changes in the PL. The sign of the PLDMR – whether positive (PL-enhancing) or negative (PL-quenching) – is usually determined by comparing it to that of a known standard. However, when a known standard is not available, the most reliable method is to directly monitor the PL intensity vs H under constant microwave irradiation. In other words, the small change in the PL intensity is observed directly at the field-for-resonance, without resorting to lockin detection.

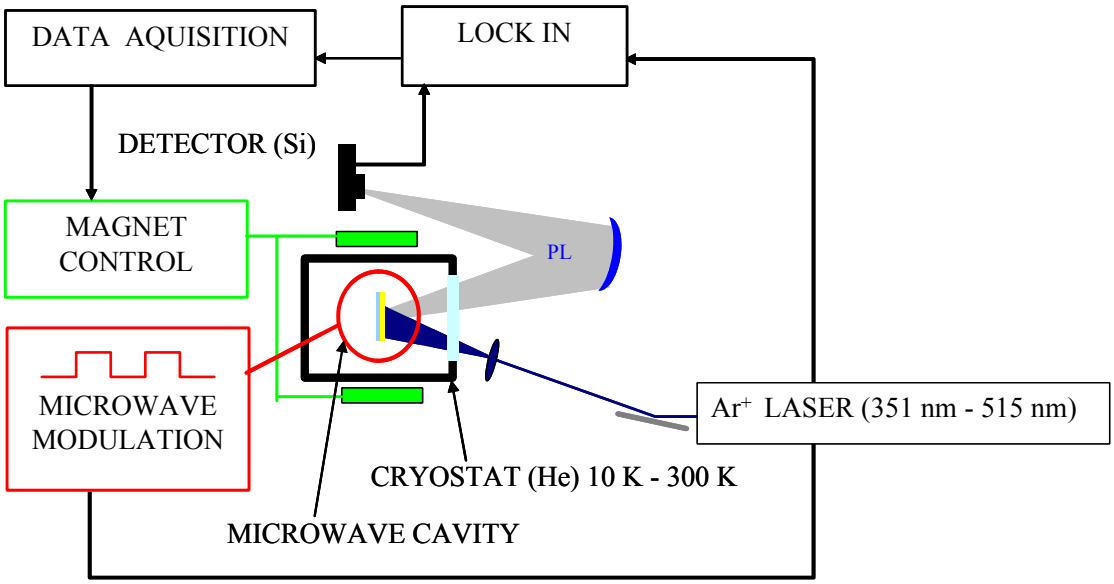

Fig. 2-2. *Schematic of the X-band PLDMR system in which the sample is photoexcited by an Ar+ laser.*

The spin-1/2 PLDMR

The spin $\boldsymbol{S}$ of an exciton is "locked", either $\boldsymbol{S}$ = 0 for SEs or $\boldsymbol{S}$ = 1 for TEs. However, the spins of the electron-hole polaron pair (p^+- p^-) are much less interacted with each other, so their spin-spin coupling energy is usually negligible compared to the Zeeman splitting induced by the applied static magnetic field H_0. Each polaron p has S = 1/2 and it can align parallel or antiparallel to H_0, which results in four possible energy levels:

$$E = \frac{1}{2}(\pm g_e, \pm g_h)\mu_B H_0 \qquad (2.8)$$

where g_e and g_h are the e^- and h^+ g values, and μ_B is the Bohr magneton.

As mentioned in Chapter 1, the lifetime of SEs is much shorter than that of TEs, which indicates that the recombination of spins in the singlet configuration would be much faster than that in the triplet configuration, leading to a steady state population difference between the singlet and triplet polaron pairs (n_2, $n_3 < n_1$, n_4), as shown in Fig. 2-3. When at a magnetic resonance condition, the photon energy of the microwave is:

$$h\nu = g_e\mu_B H_0 \; or \; g_h\mu_B H_0 \qquad (2.9)$$

then the steady state population between the different states will be equalized, i.e., $n_1 = n_3$ or $n_2 = n_4$ [15]. These changes in the population in the different states under magnetic resonance conditions will directly or indirectly affect the PL signal, which is the spin-1/2 PLDMR signal.

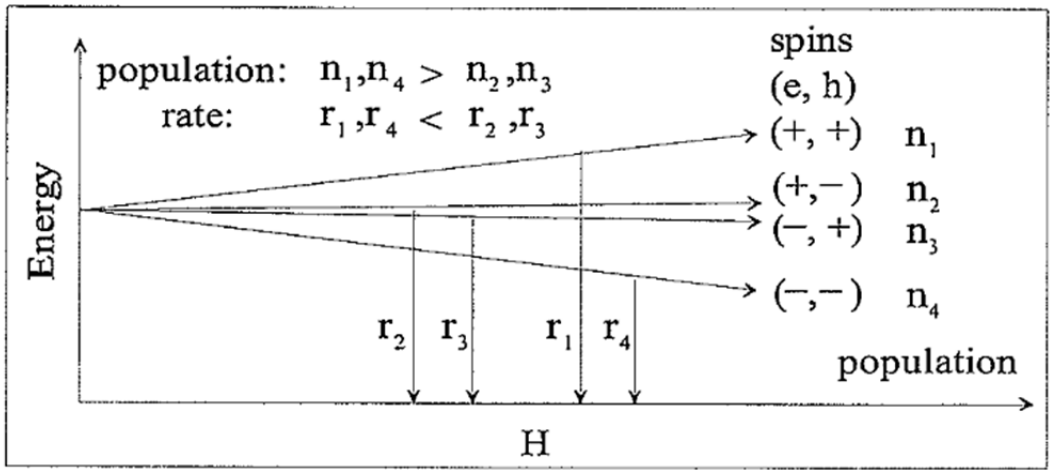

Fig. 2-3. *Schematic energy levels with magnetic field for weakly interacting distant electron-hole polaron pairs.*

Fig. 2-4 shows the spin 1/2 PLDMR in (a) Poly[2-methoxy-5-(2-ethylhexyloxy)-1,4-phenylenevinylene] (MEH-PPV) and (b) Oxidized rubrene. As clearly seen, the resonance is symmetric in both MEH-PPV and oxidized rubrene, but the sign is different. The MEH-PPV sample shows a positive (PL-enhancing) signal at $g \approx 2.00649 \pm 0.00002$, and the oxidized rubrene sample shows a negative (PL-enhancing) signal $g \approx 2.00752 \pm 0.00002$.

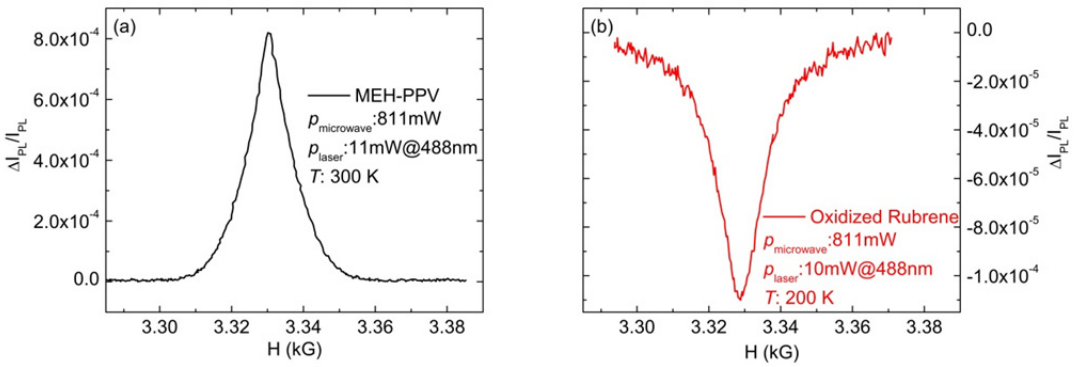

Fig. 2-4. *The spin-1/2 PLDMR in (a) MEH-PPV and (b) Oxidized rubrene.*

Regarding the origin of the positive spin-1/2 PLDMR, there are two major mechanisms still under debate:

1) The delayed PL model [16-18]:

   This model is based on recombination and considers the positive spin-1/2 PLDMR to be a form of delayed PL resulting from the recombination of slow (long-lived) polarons. It has been used to argue that SEs formation is favored over TEs formation in OLEDs [16-17]. The magnetic resonance condition enhances conversion of triplet polaron pairs to singlet pairs, consequently enhancing SE formation from such pairs, and consequently the delayed PL, at the expense of TE formation.

2) Triplet – polaron quenching (TPQ) model [8-9,19-31]:

   This model is based on quenching, where the positive spin-1/2 PLDMR is due to reduced SE annihilation under resonance conditions. Under magnetic resonance conditions, the population of the polarons and TEs is decreased, which is supported by the negative change in the polaron and TE photoinduced absorption bands, i.e., the negative spin-1/2 PADMR.[29-30,32] This negative change is believed to be due to the spin-dependent nature of the TPQ interaction. The magnetic resonance condition will convert composite TE-polaron states that are in one of the 4 sublevels of the spin 3/2 quadruplet configuration, where TE quenching by the polaron is forbidden, to states in the spin 1/2 doublet configuration, where this quenching is allowed. Those SEs quenchers, polarons and TEs, are decreased; therefore, the quenching effect caused by those quenchers should be reduced, which leads to a PL-enhancing spin-1/2 PLDMR.

In order to distinguish between the contribution of the TPQ interaction and that of the delayed PL to the observed positive spin-1/2 PLDMR, the double-modulation PLDMR was introduced recently. [8-9] In this technique, both the Ar^+ laser and the microwave power are modulated. The signal from the PMT or Si PD is introduced into the signal input channel of the additional lockin amplifier #2 (see Fig. 2-5), which is referenced by the driver of the laser modulation, i.e., at the laser modulation frequency typically in the range 1 kHz < f_L < 200 kHz. The output from lockin #2 is then introduced into the signal input channel of lockin #1, which is referenced by the driver of the microwave chopper, i.e., at the microwave chopping frequency f_M. Hence, in effect, lockin #2 filters out the slow component of the luminescence, i.e., the delayed PL that is slower than $1/f_L$. The experimental setup is shown in Fig. 2-5.

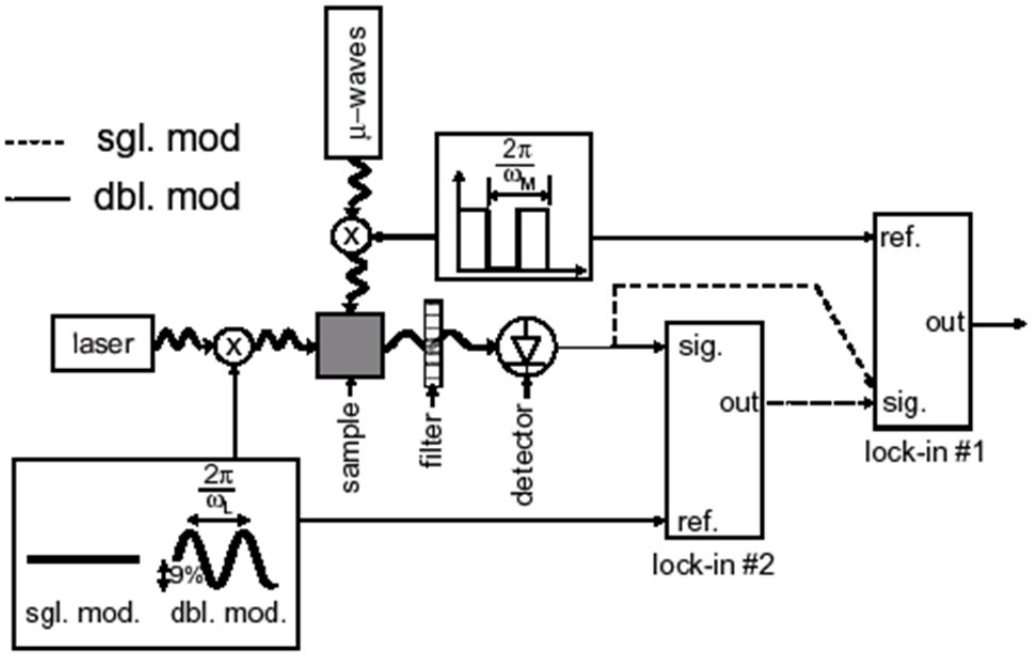

Fig. 2-5. *The experimental setup DM-PLDMR.*

The results of DM-PLDMR measurements on MEH-PPV at 100 K (shown in Fig. 2-6), and Poly(3-hexylthiophene-2,5-diyl) (P3HT) at both 15 K and 300 K, unambiguously support the TPQ mechanism as the source of that PLDMR and rules out enhanced delayed PL as a significant mechanism for that resonance.

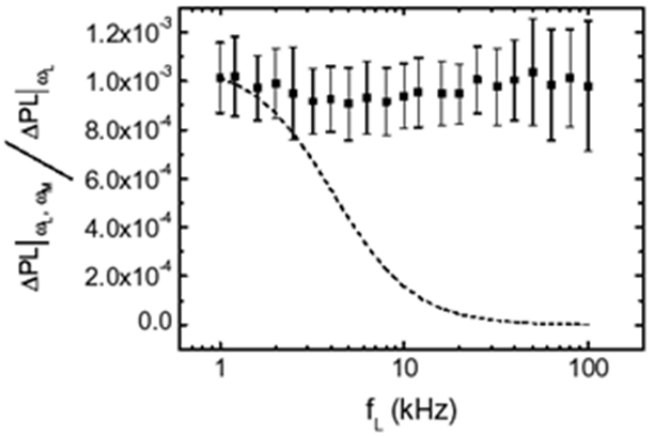

Fig. 2-6. *The DM-PLDMR $\Delta PL|_{\omega L,\omega M}/\Delta PL|_{\omega L}$ of an MEH-PPV film vs. the laser modulation frequency f_L, with f_M = 200 Hz. The dashed line is the behavior predicted by the delayed PL model to first order, scaled to match the data.*

The origin of the negative spin-1/2 PLDMR is believed due to the enhanced spin-dependent formation of spinless bipolarons or trions (bipolarons stabilized by a counterpolaron or counterion). The increased population of the bipolarons or trions quenches more SEs at magnetic resonance conditions, which leads to a negative spin-1/2 PLDMR.

The spin-1 TE PLDMR

The spin-1 TE PLDMR is from the TEs, the typically lifetime of TEs is about ~ 10^{-4} to 10 s. According to quantum mechanics, the spin $\boldsymbol{S}$ =1 TEs have 3 different sublevels, $|+1\rangle$, $|0\rangle$ and $|-1\rangle$. The $\Delta m_S = \pm 1$ transitions, shown in Fig. 2-7, which are the transitions between $|+1\rangle \leftrightarrow |0\rangle$ or $|0\rangle \leftrightarrow |-1\rangle$, can be observed at field A

and B. The corresponding g is around 2, and it is termed the ”full field spin-1 resonance”. The $\Delta m_S = \pm 2$ transitions, shown in Fig. 2-6, which are the transitions between $|+1\rangle \leftrightarrow |-1\rangle$, can be observed at field A. The corresponding g is around 4, and according to Equation 2.9, the magnetic field H is only the half of $\Delta m_S = \pm 1$ transitions, so it is termed the ”half field spin 1 resonance”.

Since the positions A, B, and C depend on the orientation of H relative to the principal axes of the TE state, an amorphous or powder sample will yield half-field and full-field “powder pattern” such as those shown in Fig. 2-8. A reduction of TEs enhances the PL of the luminescent π-conjugated polymers; the only possible mechanism that could account for this observation was the TPQ model, which is the same mechanism for the positive spin-1/2 PLDMR. The TPQ mechanism also raises an intriguing

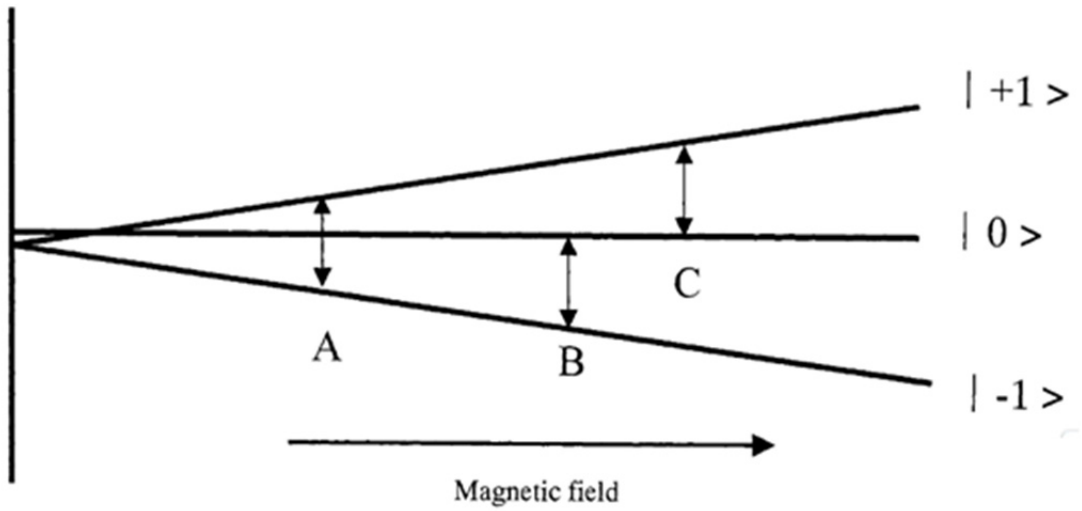

Fig. 2-7. *Energy vs. magnetic field for spin-1 TE PLDMR.*

possibility that the TEs responsible for the resonance are likely those trapped by an adjacent polaron. Hence they would be localized at a site adjacent to that polaron [3,12-13,19-21,31,34-38].

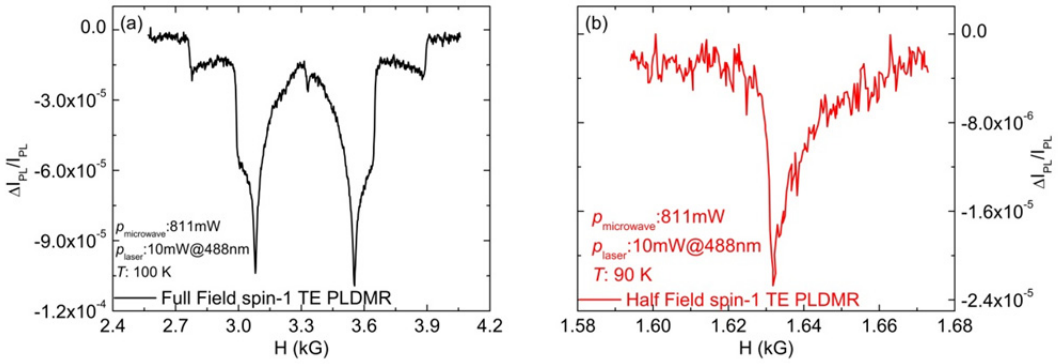

Fig. 2-8. *The spin-1 TE (a) full field and (b) half field PLDMR in oxidized rubrene.*

References

[1] C. Adachi, M. A. Baldo, M. E. Thompson and S. R. Forrest, J. Appl. Phys. **90**, 5048 (2001).

[2]M. A. Baldo, D. F. O'Brien, Y. You, A. Shoustikov, S. Sibley, M. E. Thompson and S. R. Forrest, Nature **395**, 151 (1998).

[3] *Electronic processes in organic crystals and polymers*, 2nd ed., by M. Pope and C. E. Swenberg (Oxford University Press, New York, 1999).

[4] *An Introduction to Organic Light-Emitting Devices*, edited by J. Shinar and V. Savvate'ev (Springer Verlag, New York, 2004).

[5] R. Kersting, U. Lemmer, M. Deussen, H. J. Bakker, R. F. Mahrt, H. Kurz, V. I. Arkhipov, H. Bässler and E. O. Göbel, Phys. Rev. Lett. **73**, 1440 (1994).

[6] A. Kadashchuk, V. I. Arkhipov, C.-H. Kim, J. Shinar, D.-W. Lee, Y.-R. Hong, J.-I. Jin, P. Heremans and H. Bässler, Phys. Rev. B **76**, 235205 (2007).

[7] C. A. Steren, H. van Willigen and M. Fanciulli, Chem. Phys. Lett. **245**, 244 (1995).

[8] M.-K. Lee, M. Segal, Z. G. Soos, J. Shinar and M. A. Baldo, Phys. Rev. Lett. **94**, 137403 (2005).

[9] M. Segal, M. A. Baldo, M. K. Lee, J. Shinar and Z. G. Soos, Phys. Rev. B **71**, 245201 (2005).

[10]M. A. Baldo, C. Adachi and S. R. Forrest, Phys. Rev. B **62**, 10967 (2000).

[11]S. Reineke, K. Walzer and K. Leo, Phys. Rev. B **75**, 125328 (2007).

[12] V. I. Lesin, A. I. Pristupa and E. L. Frankevich, Opt. Spectrosc+ **51**, 477 (1981).

[13] A. M. Muller, Y. S. Avlasevich, W. W. Schoeller, K. Mullen and C. J. Bardeen, J. Am. Chem. Soc. **129**, 14240 (2007).

[14] M. Scharnoff, J. Chem. Phys. **46**, 3263 (1967).

[15] D. J. Dunstan, J. Phys. C, Solid State Phys., **12**, 2927 (1979).

[16] M. Wohlgenannt, Kunj Tandon, S. Mazumdar, S. Ramasesha and Z. V. Vardeny, Nature **409**, 494 (2001).

[17] M. Wohlgenannt, X. M. Jiang, Z. V. Vardeny and R. A. J. Janssen, Phys. Rev. Lett. **88**,197401 (2002).

[18] M. Wohlgenannt, C. Yang and Z. V. Vardeny, Phys. Rev. B **66**, 241201(R) (2002).

[19] L. S. Swanson, J. Shinar and K. Yoshino, Phys. Rev. Lett. **65**, 1140 (1990).

[20] L. S. Swanson, P. A. Lane, J. Shinar and F. Wudl, Phys. Rev. B **44**, 10617 (1991).

[21] L. S. Swanson, J. Shinar, A. R. Brown, D. D. C. Bradley, R. H. Friend, P. L. Burn, A. Kraft and A. B. Holmes, Phys. Rev. B **46**, 15072 (1992).

[22] L. S. Swanson, J. Shinar, P. A. Lane, B. C. Hess and F. Wudl, Syn. Met. **49-50**, 481 (1992).

[23] L. S. Swanson, J. Shinar, Y. W. Ding and T. J. Barton, Syn. Met. **55-57**, 1 (1993).

[24] L. S. Swanson, P. A. Lane, J. Shinar, Y. Pang and T. J. Barton, Syn. Met. **55-57**, 293 (1993).

[25] W. Graupner, J. Partee, J. Shinar, G. Leising and U. Scherf, Phys. Rev. Lett. **77**, 2033 (1996).

[26] P. A. Lane, J. Shinar and K. Yoshino, Phys. Rev. B **54**, 9308 (1996).

[27] *Handbook of Organic Conductive Molecules and Polymers: Vol. 3. Conductive Polymer: Spectroscopy and Physical Properties*, edited by H. S. Nalwa (J. Wiley, New York, 1997).

[28] E. J. W. List, C. H. Kim, J. Shinar, A. Pogantsch, G. Leising and W. Graupner, Appl. Phys. Lett. **76**, 2083 (2000).

[29]E. J. W. List, J. Partee, J. Shinar, U. Scherf, K. Müllen, E. Zojer, K. Petritsch, G. Leising and W. Graupner, Phys. Rev. B **61**, 10807 (2000).

[30] E. J. W. List, C.-H. Kim, A. K. Naik, U. Scherf, G. Leising, W. Graupner and J. Shinar, Phys. Rev. B **64**, 155204 (2001).

[31] E. J. W. List, U. Scherf, K. Müllen, W. Graupner, C.-H. Kim and J. Shinar, Phys. Rev. B **66**, 235203 (2002).

[32] X. Wei, B. C. Hess, Z. V. Vardeny and F. Wudl, Phys. Rev. Lett. **68**, 666 (1992).

[33] H. Thomann, L. R. Dalton, M. Grabowski, Y. Tomkiewicz, N. S. Shiren and T. C. Clarke, Phys. Rev. Lett. **50**, 533 (1983).

[34] S. Kuroda, T. Noguchi and T. Ohnishi, Phys. Rev. Lett. **72**, 286 (1994).

[35] D. K. Campbell, A. R. Bishop and K. Fesser, Phys. Rev. B **26**, 6862 (1982).

[36] A. J. Heeger, S. Kivelson, J. R. Schrieffer and W.-P. Su, Rev. Mod. Phys. **60**, 781 (1988).

[37] J. M. Warman, G. H. Gelinck, J. J. Piet, J. W. A. Suykerbuyk, M. P. de Haas, B. M. W. Langveld-Voss, R. A. J. Janssen, D.-H. Hwang, A. B. Holmes, M. Remmers, D. Neher, K. Müllen, and P. Bäuerle, in *Optical Probes of Conjugated Polymers,* edited by Z. Valy Vardeny and L. J. Rothberg, SPIE Conf. Proc. **3145**, 142 (1997).

[38] M. Reufer, M. J. Walter, P. G. Lagoudakis, A. B. Hummel, J. S. Kolb, H. G. Roskos, U. Scherf and J. M. Lupton, Nat. Mat. **4**, 340 (2005).

Chapter 3. High efficiency solution-processed small molecule electrophosphorescent OLEDs

A paper published in *Advanced Materials*

Min Cai, Teng Xiao, Emily Hellerich, Ying Chen, Ruth Shinar and Joseph Shinar

Abstract

We demonstrate *very high efficiency* (forward power and luminous efficiencies up to 60 lm/W and 69 Cd/A, respectively) *spin-coated small molecule* electrophosphorescent OLEDs (SMOLEDs) based on a green-emitting iridium complex doped into a 4,4'-bis(9-carbazolyl)-biphenyl (CBP) host. Electron- and hole-transporting molecules were blended with the host to improve the transport balance of the charge carriers. An additional electron- transporting/hole-blocking BPhen layer was thermally evaporated on the spin-coated active layer, followed by the LiF/Al cathode. The peak efficiency of these largely-solution-processed SMOLEDs is higher than that of any polymer or solution-processed OLED reported to date, and almost as high as that of the most efficient thermally evaporated (SM)OLED, when excluding the contribution of outcoupling-enhancing structures such as microlens arrays. When such outcoupling enhancement is included, the peak power efficiency would be 120 lm/W, essentially the highest of any OLED reported to date. The high efficiency is attributed to the relatively high carrier mobility in CBP, the enhanced mobility due to the additional electron- and hole-transporting dopants, and the smoothness of the doped CBP-based films, whose RMS surface roughness is only ~0.50 nm. The enhanced performance of the spin-coated SMOLEDs implies that such devices are an

attractive alternative to the fabrication of multi-component SMOLEDs, e.g., white OLEDs, reducing the cost and complexities of co-evaporation of multiple dopants and host materials in the thermal vacuum deposition processes.

Introduction

Extensive research on organic light-emitting diodes (OLEDs) continues due to their promise in applications such as flat panel displays and solid state lighting [1-5]. Commonly, thermal high-vacuum evaporation technology is used for fabrication of small molecule-based OLEDs (SMOLEDs) and solution processing technology is used for those based on polymers (PLEDs). Thermal evaporation deposition enables complicated multilayer device architectures and renders excellent devices with high efficiencies [6,7]. In contrast, solution-based deposition limits fabrication of composite device structures because the solvent used for one layer can redissolve or otherwise damage the previous layers [8]. Therefore, thermally evaporated SMOLEDs are typically more efficient and longer-lived than solution-processed PLEDs. However, thermal evaporation deposition has its own disadvantages. First, it requires high vacuum and is consequently much more costly. Second, making multi-dopant OLEDs, such as white OLEDs (WOLEDs), requires precise control of the doping concentration of each dopant in the emitting layer (EML) to obtain the desired emission [9,10]. These reasons usually lead to a fabrication process of greater complexity and higher cost. On the other hand, solution processing, such as spin-coating, inkjet printing, and screen printing, is advantageous over thermal evaporation processing, due to its low-cost and large area manufacturability [10,11]. Additionally, it is possible to realize co-doping of several dopants by mixing the dopants and host material in solution. Hence, the fabrication of SMOLEDs via a solution process is of great importance. To that end, we demonstrate high efficiency (forward power and

luminous efficiencies up to 60 lm/W and 69 Cd/A, respectively) spin-coated electrophosphorescent SMOLEDs based on green-emitting tris[2-(p-tolyl)pyridine] iridium(III) ($Ir(mppy)_3$) doped into a 4,4'-bis(9-carbazolyl)-biphenyl (CBP) host, probably due to the materials and film morphology. This is the highest reported efficiency of any solution-processed OLED and among the highest of any OLED without outcoupling enhancement. The electron- transporting 2-(4-biphenylyl)-5-(4-tert-butylphenyl)- 1,3,4-oxadiazole (PBD) and hole- transporting N,N'-diphenyl-N,N'-bis(3-methyl-phenyl)- [l,l'biphenyl]-4,4'-diamine (TPD) are blended with the host to improve the transport balance of the charge carriers. A poly(3,4-ethylenedioxy thiophene):poly(4-styrenesulfonate) (PEDOT:PSS) hole-injection layer is first spin-coated on the indium tin oxide (ITO)/glass substrate, and an additional electron-transporting/hole-blocking 4,7-diphenyl-1,10-phenanthroline (BPhen) layer is thermally evaporated on the spin-coated active layer. Hence, the structure of the devices is ITO/spin-coated PEDOT:PSS/spin-coated CBP:TPD:PBD: $Ir(mppy)_3$/thermally evaporated BPhen/LiF/Al. In particular, the performance of these SMOLEDs is superior to that of PLEDs with a similar structure based on poly(N-vinyl carbazole) (PVK) as the host (device structure: ITO/spin-coated PEDOT:PSS/spin-coated PVK:TPD:PBD:$Ir(mppy)_3$/thermally evaporated BPhen/LiF/Al). The enhanced performance of the spin-coated SMOLEDs implies that such devices are an attractive and alternative route to the fabrication of small-molecular multi-component OLEDs, such as white OLEDs, reducing the cost of devices and avoiding the complexities of the co-evaporation of multiple dopants and host material in the vacuum deposition.

Results and discussion

In spin-coated PLEDs, small molecule guests are typically blended with a polymer host in a suitable solvent as is the case for PVK:Ir(mppy)$_3$ PLEDs [12,13]. However, when using this approach, phase separation may occur either after some time of operation or immediately following fabrication due to differences between small molecules and conjugated polymers in attributes such as viscosity and boiling point [14]. To address this issue, many other solution-processible organic molecules were designed and synthesized, including dendrimers, oligomers, spiro-molecules, and binuclear metal chelates [15-18]. Recently, efficient OLEDs based on solution-processed small molecules have been reported [19–26]. For example, He *et al.* reported that fluorescent SMOLEDs fabricated by spin-coating blends of N, N"-bis-(3-naphthyl)-N, N"-biphenyl-(1,1"-biphenyl)-4,4"-diamine (NPB) and tris-(8-hydroxyquinoline)-aluminum (Alq$_3$) as the emitting layer exhibited maximum brightness and luminous efficiency exceeding 10,000 Cd/m^2 and 3.8 Cd/A, respectively [23]. These values are comparable to those of thermally evaporated Alq$_3$-based devices. Thus, the development of solution-processed SMOLEDs based on materials used in high-efficient OLEDs fabricated via vacuum deposition is promising.

Ir(mppy)$_3$ is a widely used phosphorescent dopant in OLEDs. The energy of the lowest lying triplet state of Ir(mppy)$_3$ is E_{T1} ~ 2.38 eV, while that of the CBP host is E_{T1} ~ 2.56 eV, which satisfies the obvious requirement that E_{T1} of the host be ≥ to that of the guest [27,28]. Previous studies showed that in the case of PVK:Ir(mppy)$_3$PLEDs, carrier trapping and subsequent recombination on the guest molecule is, in general, the dominant triplet excitation path of the phosphorescent

guest [12,29-31]. This is due to the energy of the highest occupied molecular orbital E_{HOMO} = -5.4 eV and the lowest unoccupied molecular orbital E_{LUMO} = -2.4 eV of

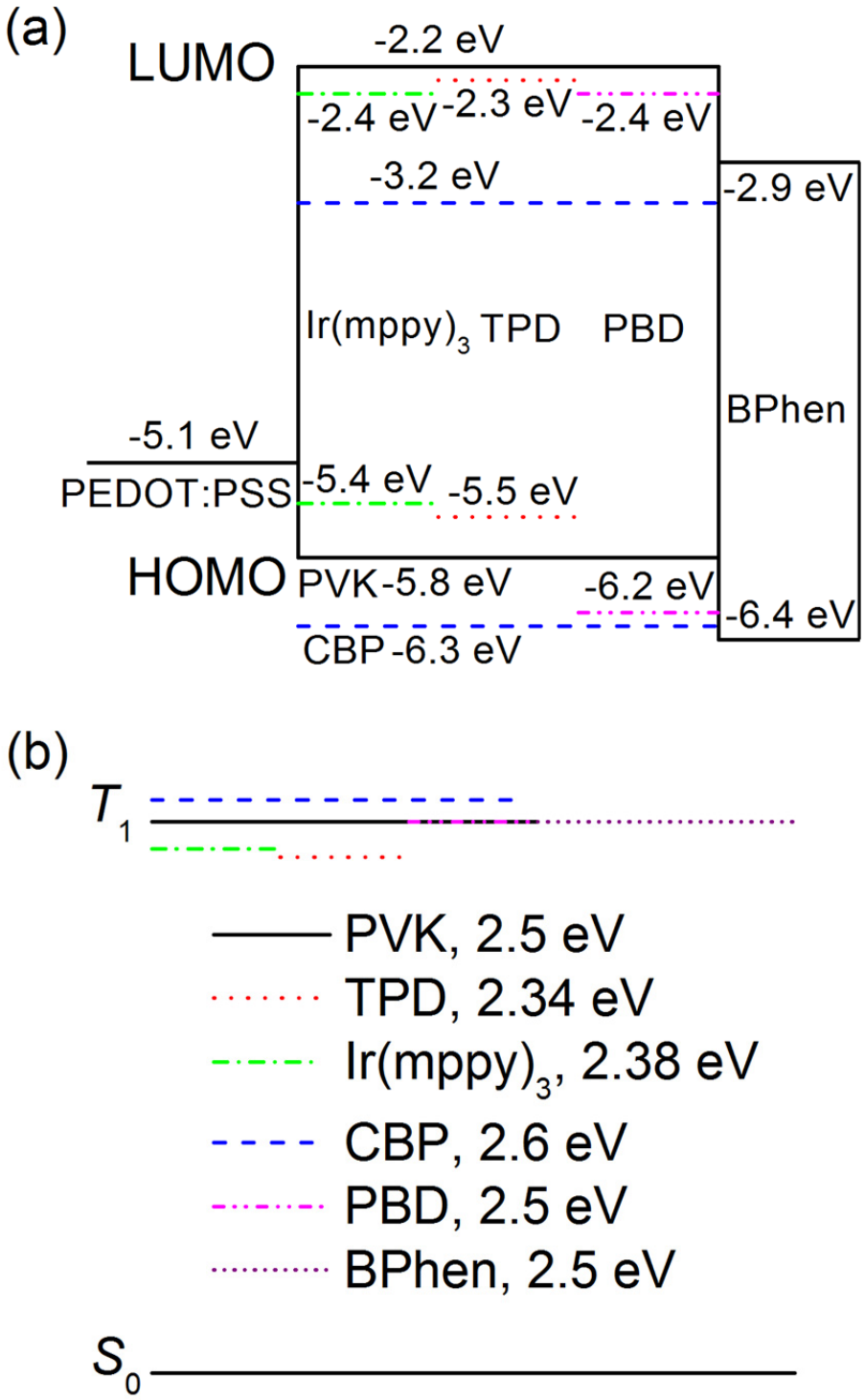

Fig. 3-1. *(a) HOMO and LUMO energy levels and (b) triplet energy (T_1) levels of the various OLED materials.*

$Ir(mppy)_3$ being within those of PVK (E_{HOMO} = -5.8 eV, E_{LUMO} = -2.2 eV); see Fig. 3-1(a)) [32,33]. Even though the direct formation of the guest triplet state is the most elegant way to achieve good color purity and high efficiency, this direct formation often requires a high operating voltage due to the buildup of a space-charge field [32]. In order to improve the performance of the PVK:$Ir(mppy)_3$ PLEDs, electron-transporting PBD ($\mu_e \sim 2\times10^{-5}$ cm^2/Vs) and hole transporting TPD ($\mu_h \sim 2\times10^{-3}$ cm^2/Vs) were co-doped with the $Ir(mppy)_3$ [34,35]. The introduction of PBD and TPD diminishes to a certain extent the buildup of the space charge field in the device and improves the balance of charge injection and transport due to their high carrier mobilities [12,29-32]. It was found that the optimized concentrations of PVK,TPD, PBD and $Ir(mppy)_3$ in the EML were 61, 9, 24 and 6 wt. %, respectively [12, 29-32]. On the other hand, the carbazole-containing CBP host is a very common host material in thermally-evaporated phosphorescent SMOLEDs that yield highly efficient devices with emission colors across the entire visible spectrum [36-39]. However, systematic studies on solution-processing of CBP and CBP-based SMOLEDs have not been reported. Therefore in this study, a series of CBP and CBP-based multilayer SMOLEDs with the following structures were fabricated:

Device A: ITO/spin-coated PEDOT:PSS/spin-coated CBP/thermally evaporated BPhen (40 nm)/LiF (1 nm)/Al (100 nm),

Device B: ITO/spin-coated PEDOT:PSS/spin-coated CBP (0.94):$Ir(mppy)_3$(0.06)/thermally evaporated BPhen (40 nm)/LiF (1 nm)/Al (100 nm), and

Device C: ITO/spin-coated PEDOT:PSS/spin-coated CBP(0.61):TPD(0.09):PBD(0.24):Ir(mppy)$_3$(0.06)/thermally evaporated BPhen (40 nm)/LiF (1 nm)/Al (100 nm).

PLEDs based on PVK similar to Device C were also fabricated for comparison:

Device D: ITO/spin-coated PEDOT:PSS/spin-coated PVK(0.61):TPD(0.09):PBD(0.24):Ir(mppy)$_3$(0.06)/thermally evaporated BPhen (40 nm)/LiF (1 nm)/Al (100 nm). This structure differed from previously reported structures by the addition of the BPhen layer [12,32-33].

The optimized fractions of each component by weight in the EML were 0.61 CBP or PVK, 0.09 TPD, 0.24 PBD, and 0.06 Ir(mppy)$_3$. E_{HOMO}, E_{LUMO}, and E_{T1} of the materials in these devices are also shown in Fig. 3-1 [32,33,36,40-43].

In order to determine the possible effect of morphology on device performance, we examined the films by atomic force microscopy (AFM). Some polymer blend systems phase separate and AFM has been shown to be a powerful tool in the analysis of this behavior [44]. AFM images of the spin-coated emitting films are shown in Fig. 3-2; all show pinhole-free surfaces.

The root-mean-square (RMS) surface roughness spin-coated CBP and PVK films are 0.98 and 0.87 nm, respectively. They are shown in Figs. 3-2(a)-(b). These values are significantly smaller than the 1.5 and 1.3 nm roughness of the thermally evaporated films measured in our work and by Liu *et al.*, respectively [45]. This demonstrates that a typical amorphous SM EML can be fabricated effectively not only by thermal vacuum deposition but also by a solution process.

Figs. 3-2(c)-(f) show the surface morphology of the spin-coated films of the

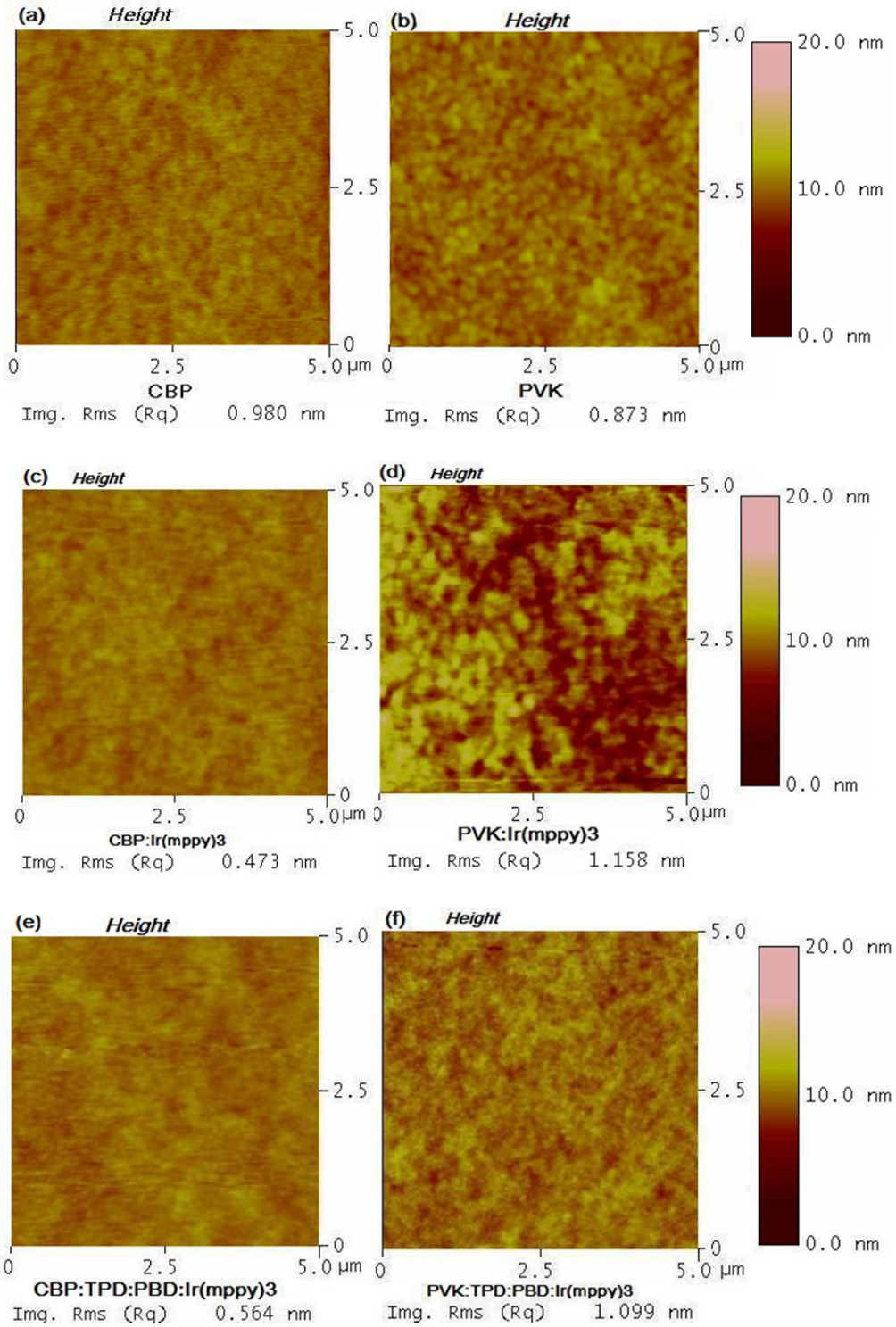

Fig. 3-2. *AFM images of thin films formed by spin-coating (a) CBP, (b) PVK, (c) CBP:Ir(mppy)$_3$, (d) PVK:Ir(mppy)$_3$,(e) CBP:TPD:PBD:Ir(mppy)$_3$ and (f) PVK:TPD:PBD:Ir(mppy)$_3$.*

CBP (0.94):Ir(mppy)$_3$ (0.06), PVK (0.94):Ir(mppy)$_3$ (0.06), CBP (0.61):TPD (0.09): PBD (0.24):Ir(mppy)$_3$ (0.06) and PVK (0.61):TPD (0.09):PBD (0.24):Ir(mppy)$_3$ (0.06) blends, respectively. The RMS surface roughness values of these films are 0.47, 1.16, 0.57 and 1.10 nm, respectively. *Thus, replacing PVK with CBP as the host matrix reduces the EML's surface roughness by > 50%.* A possible explanation for this behavior may be related to the difference between the small molecules and polymers. The latter often show improved mechanical strength due to a stronger intermolecular forces and steric hindrances. Hence, during spin-coating, the films formed by small molecules and polymers show different degrees of phase separation [46,47]. Thus, for these particular compositions of the CBP- and PVK-based blends, phase separation likely occurs more readily in the PVK-based films than in the CBP-based films prepared under similar conditions. The increased phase separation would then increase the surface roughness in the PVK-based films. The better uniformity of the EML in Device C (in comparison to Device D) may be partially responsible for the better device performance described next. Note, however, that the morphology and phase separation in the blends are expected to strongly depend on the composition, and the conclusions drawn in this work are valid only for these particular compositions.

It is noteworthy that the thin films of the spin-coated blends of 6 wt. % Ir(mppy)$_3$ in CBP are surprisingly smoother, as their RMS surface roughness is ~50% lower than that of the CBP-only films. This intriguing result indicates that Ir(mppy)$_3$ reduces the roughness of the CBP-based films and it warrants further investigation. Indeed, it is made all the more surprising in view of the observation that adding TPD and PBD

into the blend increases the RMS surface roughness only slightly, from 0.47 nm to 0.56 nm.

As mentioned, in our experiments, all devices have a spin-coated PEDOT:PSS hole-injection layer, which precedes the spin-coated EML. The BPhen electron-transporting layer is thermally evaporated on the spin-coated EML. It is one of the most attractive electron-transporting materials, with $\mu_e \sim 2.8\times10^{-4}$ cm^2/Vs at room temperature and a high $E_{T1} = 2.5$ eV (Fig. 3-1(b)) [42,48]. Thus, the role of the BPhen layer is two-fold: First, it improves the electron injection and transport due to its high electron mobility, thus providing better charge balance in the devices. Second, its high E_{T1} and deep HOMO level (-6.4 eV) confine holes and excitons within the EML, resulting in high efficiencies [42].

The spin-coated EML of Device A consists of CBP only. The EL spectrum, which peaked at ~409 nm, is apparently due to bulk emission from CBP. This spin-coated CBP device shows a peak brightness of ~200 Cd/m^2 and a peak luminous efficiency of 0.23 Cd/A, which corresponds to an external quantum efficiency of 0.73 %. These values are comparable to those of the thermally evaporated devices[49,50], demonstrating that spin-coated CBP-based OLEDs are viable and promising.

The normalized electroluminescence (EL) spectra of devices B, C and D, driven at 57 mA/cm^2, are shown in Fig. 3-3(a). As clearly seen, the spectra peak at ~510 nm, and their EL bands are nearly identical. Hence, the EL originates only from the $Ir(mppy)_3$ molecule, indicating an essentially complete energy or charge transfer from the other components of the blend to the $Ir(mppy)_3$.

Fig. 3-3 also shows the brightness and current density vs. voltage, and the luminous efficiency, luminous power efficiency and external quantum efficiency vs. brightness for Devices B, C and D. The spin-coated EML of Device B, made of CBP (0.94):Ir(mppy)$_3$ (0.06), shows a peak luminous efficiency of 26 Cd/A, a peak luminous power efficiency of 14 lm/W and a peak external quantum efficiency of

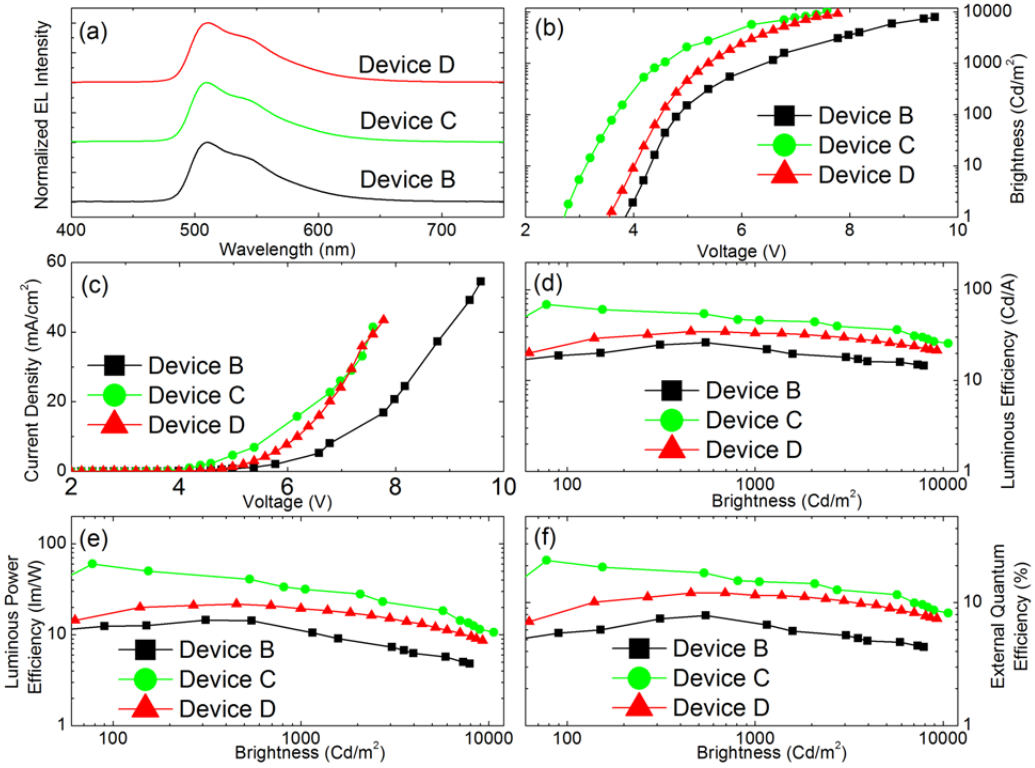

Fig. 3-3. *Comparison of device characteristics (a) EL spectra, (b) Brightness vs. voltage, (c) Current density vs. voltage, (d) Luminous efficiency vs. brightness, (e) Luminous power efficiency vs. brightness, (f) External Quantum Efficiency vs. brightness of Device B (square), Device C (circle) and Device D (triangle).*

7.9 %. These results indicate that spin-coated Ir(mppy)$_3$:CBP-based devices are comparable to the thermally evaporated ones [36,51].

As expected from Ref. 32 the performance of Device C, where the EML includes TPD and PBD, is much better than Device B. The turn-on voltage (i.e., the voltage at

1 Cd/m^2) is 2.8 V for Device C, which is ~1.0 V lower than that of Device B, and the current density of Device C is larger throughout the whole bias range. This reduction of the turn-on voltage and larger current density are clearly due to the increased hole conductivity of TPD and electron conductivity of PBD. In addition, TPD, with a HOMO level similar to $Ir(mppy)_3$ (see Fig. 3-1) likely prevents saturation of the $Ir(mppy)_3$ with trapped holes, and eliminates the buildup of the hole space charge. This behavior is consistent with previous studies on PVK:$Ir(mppy)_3$ PLEDs [12,29-33]. As a result of the improved balance of the charge injection and transport due to TPD and PBD, the maximum luminous efficiency, luminous power efficiency and external quantum efficiency reach 69 Cd/A, 60 lm/W and 22 %, respectively. We note that with an outcoupling enhancement of 100% such as reported recently [52], the maximal luminous power efficiency of Device C would reach 120 lm/W, i.e., it would be one of the highest reported to date on any OLED.

The turn-on voltage of Device D is 3.5 V, or 0.7 V higher than that of Device C, and the current density is lower in comparison to Device C. This clearly demonstrates a reduced conductivity of Device D. The higher conductivity and higher efficiencies of Device C are probably due to the much higher hole mobility of CBP ($\mu_h \sim 10^{-3}$ cm^2/Vs) than of PVK ($\mu_h \sim 10^{-9}$ cm^2/Vs), but may also be related to the smoother surface of the CBP-based layer [53,54]. The corresponding efficiencies of Device D are shown in Fig. 3-3. The peak luminous, luminous power, and external quantum efficiencies are 35 Cd/A, 22 lm/W, and 12 %, respectively. The results therefore demonstrate that using CBP as the host material instead of PVK improves the quality of the spin-coated film, enhancing the overall device performance.

The high efficiency of Device C is likely due to the following factors:

(i) The relatively high carrier mobility in CBP:Ir(mppy)$_3$:TPD:PBD blends. Choulis *et al.* reported highly efficient spin-coated PVK:Ir(mppy)$_3$:TPD:PBD-based PLEDs [33]. However, the replacement of PVK by CBP probably improves the devices' carrier mobility significantly, as the intrinsic mobility in the connecting PVK tissue is very low (~10^{-9} cm^2/Vs).

(ii) The considerable amounts of the hole- transporting TPD and electron-transporting PBD likely improve charge balance, as they probably do in the PVK:Ir(mppy)$_3$:TPD:PBD-based PLEDs to yield the high efficiency of these latter devices.

(iii) The addition of the BPhen layer blocks holes from reaching the cathode, and, importantly separates the recombination zone from the cathode region. This largely eliminates quenching of the excitons by the cathode.

(iv) Given the AFM images shown in Fig. 3-2, the apparently smoother morphology of the CBP-based SMOLEDs likely results in higher carrier mobility and reduced quenching of excitons at defect sites.

Although efficient solution-processed SMOLEDs have drawn increasing attention recently, there are only a few reports on the operational lifetime of these devices [22,26,55]. Lee *et al.* fabricated other spin-coated SMOLEDs with thermally evaporated Alq$_3$ (or TPBI)/LiF/Al.[22] Their operational lifetimes L_{50}, i.e., the time at which the brightness decreased to 50% of its initial value, were ~3 h at an initial brightness L_0 = 600 Cd/m^2. Ooe *et al.*[55] fabricated SMOLEDs with a solution-processed α-NPD:CBP:Ir(tpy)$_3$ active layer, on which they thermally evaporated a hole-blocking layer of bathocuproine (BCP), followed by LiF/Al. Their L_{50} was ~4.5 h at L_0 = 1,000 Cd/m^2. Preliminary stability measurements on the CBP-based Device C yielded L_{50} ~ 2.4 h at L_0 = 810 Cd/m^2. This is more than twice that of the PVK-

based Device D, where L_{50} ~0.83 h at L_0 = 1,000 Cd/m^2, and it is actually higher than the ~3 h at L_0 = 600 Cd/m^2 reported by Lee *et al.*[22], but somewhat lower than the ~4.5 h at L_0 = 1,000 Cd/m^2 reported by Ooe *et al.*[55]. We suspect that the higher 96°C glass-transition temperature T_g of α-NPD as compared to the 65°C of TPD, and the relatively low T_g of BPhen reduced L_{50}. We also suspect that a lower film density caused by the presence of free volume between aggregates may also accelerate degradation. If that scenario is vindicated, optimizing several key parameters such as the use of materials with high T_g, spin coating speed and time, and the thermal treatment (temperature and time) should improve the stability. In addition, we note that the devices were encapsulated by lining the edges of the glass substrate with torr-seal epoxy and attaching a glass cover on the device. While such encapsulation is usually sufficient for brief measurements, it is believed that encapsulation by, e.g., the polymer multilayer technique would improve the protection of the device from water and enhance its stability [56,57]. A detailed study is in progress and will be reported later.

Conclusions

In conclusion, we described solution-processed CBP-based SMOLEDs and compared their performance to that of PVK-based PLEDs, demonstrating SMOLEDs with peak power efficiency higher than any solution-processed device and among the highest of any OLED reported to date. Uniform SMOLED EMLs of CBP:PBD:TPD:Ir(mppy)$_3$ (in comparison to the PLED EMLs PVK:PBD:TPD:Ir(mppy)$_3$) were obtained by spin-coating. The improved performance of these spin-coated SMOLEDs is believed to be due to the higher conductivity of CBP and the smoother spin-coated SMOLED EML. Consequently,

solution-processing of SMOLEDs is expected to be a new and growing route for fabricating multi-components OLEDs, such as WOLEDs, to reduce manufacturing costs, increase device size, and avoid the complexity of the vacuum co-deposition process.

Experimental procedures

PEDOT:PSS was purchased from H. C. Starck and used as the hole injection layer (HIL). CBP and PVK, the host materials, TPD and PBD, the hole- and electron-transporting molecules, respectively, and BPhen, an electron-transporting and hole-blocking material, were purchased from Sigma-Aldrich. $Ir(mppy)_3$, the dopant material, was purchased from American Dye Source. These materials were used without further purification.

Films were fabricated on 1"×1" nominally 20 Ω/square, 140 nm-thick ITO-coated glass substrates (Colorado Concept Coatings). The ITO substrates were first cleaned by a surfactant in an ultrasonic bath, and then rinsed in flowing de-ionized water. This was followed by consecutive ultrasonications, first in isopropanol and then in acetone to remove dust and organic residue. Finally, the cleaned ITO substrates were dried by blowing nitrogen and then treated in a UV ozone oven to increase the work function of the ITO and hence facilitate hole injection, as described elsewhere [58]. The PEDOT:PSS was first filtered through a 0.45 μm syringe filter. It was then spin coated at 1000 rpm for 60 s on the ITO to generate a 60 nm layer that was baked in air at 160^{o}C for 1 hour. CBP, a blends of CBP: $Ir(mppy)_3$, CBP: PBD: TPD: $Ir(mppy)_3$, or a blend of PVK: PBD: TPD: $Ir(mppy)_3$ in chlorobenzene were spin-coated on top of the PEDOT:PSS layer inside an Ar-filled glove box in which the oxygen level is generally below 10 ppm. These blends form the light emitting layers. After spin-

coating at 4000 rpm for 60 s, the resulting light-emitting layers were annealed at 60°C for 30 min. The morphology of the spin-coated thin films was measured by atomic force microscopy (AFM) (model MM AFM-2 from Digital Instruments, working at contact mode).

Following the annealing step, the films were transferred to a thermal evaporator chamber within the glove box. BPhen, LiF and Al layers were deposited sequentially by thermal evaporation using tungsten-heating baskets. The background pressure in the chamber was $\sim 2 \times 10^{-6}$ mbar. The evaporation rate of the BPhen layer was ~1 Å/s while that of LiF was 0.2 Å/s. The thickness of the BPhen layer was 40 nm and that of LiF was 1 nm. The Al cathode was deposited through a shadow mask containing 1.5 mm diameter circular holes; the evaporation rate of the Al was ~4-5 Å/s and its thickness was 100 nm. Bias voltages across the OLEDs were supplied by a Kepco DPS 40-2M programmable power supply and the current was measured using a Keithley 2000 multimeter. The OLEDs' EL was measured by a Minolta LS110 luminance meter and the EL spectra were obtained using an Ocean Optics CHEM2000 spectrometer.

Acknowledgements

Research supported by the U.S. Department of Energy, Basic Energy Sciences, Materials Sciences and Engineering Division under Contract No. DE-AC 02-07CH11358.

References

[1] C. W. Tang and S. A. Vanslyke, Appl. Phys. Lett. **51**, 913 (1987).

[2] C. W. Tang, S. A. Vanslyke and C. H. Chen, J. Appl. Phys. **65**, 3610 (1989).

[3] J. H. Burroughes, D. D. C. Bradely, A. R. Brown, R. N. Marks, K. Mackay, R. H. Friend, P. L. Burn and A. B. Holmes, Nature **347**, 539 (1990).

[4] M. A. Baldo, D. F. O'Brien, Y. You, A. Shoustikov, S. Sibley, M. E. Thompson and S. R. Forrest, Nature **395**, 151 (1998).

[5] V. Bulovic, P. E. Burrows and S. R. Forrest, Semicond. Semimet. **64**, 255 (2000).

[6] C. Adachi, M. A. Baldo, S. R. Forrest and M. E. Thompson, Appl. Phys. Lett. **77**, 904 (2000).

[7] J. S. Huang, M. Pfeiffer, A. Werner, J. Blochwitz, K. Leo and S. Y. Liu, Appl. Phys. Lett. **80**, 139 (2002).

[8] S.R. Forrest, Nature **428**, 911 (2004).

[9] B.W. D'Andrade, M.E. Thompson and S.R. Forrest, Adv. Mater. **14**, 147 (2002).

[10] M. C. Gather, A. Köhnen and K. Meerholz, Adv. Mater. **23**, 2 (2011).

[11] J. Huang, G. Li, E. Wu, Q. Xu and Y. Yang, Adv. Mater. **18**, 114 (2006).

[12] X. H. Yang, D. C. Muller, D. Neher and K. Meerholz, Adv. Mater. **18**, 948 (2006).

[13] X. H. Yang, D. Neher, D. Hertel and T. K. Daubler, Adv. Mater. **16**, 161 (2004).

[14] M. H. Jonathan, N. G. Pillow, D. W. Samuel and P. L. Burn, Adv. Mater. **11**, 371 (1999).

[15] J. Q. Ding, B. H. Zhang, J. H. Lu, Z. Y. Xie, L. X. Wang, X. B. Jing and F. S. Wang, Adv. Mater. **21**, 1 (2009).

[16] R. Pudzich and J. Salbeck, Synth. Met. **21**, 138 (2003).

[17] H. Fukagawa, K. Watanabe and S. Tokito, Org. Electron. **10**, 798 (2009).

[18] J. Qiao, L. D. Wang, J. F. Xie, G. T. Lei, G. S. Wu and Y. Qiu, Chem. Commun. **5**, 4560 (2005).

[19] N. Rehmann, D. Hertel, K. Meerholz, H. Becker and S. Heun, Appl. Phys. Lett. **91**, 103507 (2007).

[20] D. D. Wang, Z. X. Wu, X. W. Zhang, B. Jiao, S. X. Liang, D. W. Wang, R. L. He and X. Hou, Org. Electron. **11**,641 (2010).

[21] L. D. Hou, L. Duan, J. Qiao, W. Li, D. Q Zhang and Y. Qiu, Appl. Phys. Lett. **92**, 263301 (2008).

[22] T-W. Lee,T.Y. Noh, H-W. Shin, O. Kwon, J-J. Park, B-K. Choi, M-S. Kim, D. W. Shin and Y-R. Kim, Adv. Funct. Mater. **19**, 1625 (2009).

[23] L. He, J. F. Liu, Z. X. Wu, D. D. Wang, S. X. Liang, X. W. Zhang, B. Jiao, D. W. Wang and X. Hou, Thin Solid Films **518**, 3866 (2010).

[24] C.-G. Zhen, Z.-K. Chen, Q.-D. Liu, Y.-F. Dai, R. Y. C. Shin, S.-Y. Chang and J. Kieffer, Adv. Mater. **21**, 2425 (2009).

[25] Y. Byun, Y.-Y. Lyu, R. R. Das, O. Kwon, T.-W. Lee and Y. J. Park, Appl. Phys. Lett. **91**, 211106 (2007).

[26] L. Duan, L. Hou, T.-W. Lee, J. Qiao, D. Zhang, G. Dong, L. Wang and Y. Qiu, J. Mater. Chem. **20**, 6392 (2010).

[27] H. H. Liao, H. F. Meng, S. F. Homg, W. S. Lee, J. M. Yang, C. C. Liu, J. T. Shy, F. C. Chen and C. S. Hsu, Phys. Rev. B **74**, 245211 (2005).

[28] C. Adachi, R. C. Kwong, P. Djurovich, V. Adamovich, M. A. Baldo, M. E. Thompson and S. R. Forrest, Appl. Phys. Lett. **79**, 2802 (2001).

[29] S. Lamansky, P. I. Djurovich, F. Abel-Razzaq, S. Garon, D. L. Murphy and M. E. Thompson, J. Appl. Phys. **92**, 1570 (2002).

[30] K. M. Vaeth and C. W. Tang, J. Appl. Phys. **92**, 3447 (2002).

[31] X. Gong, M. R. Robinson, J. C. Ostrowski, D. Moses, G. C. Bazan and A. J. Heeger, Adv. Mater. **14**, 581 (2002).

[32] X. H. Yang and D. Neher, Appl. Phys. Lett. **84**, 2476 (2004).

[33] S. A. Choulis, V. E. Choong, M. K. Mathai and F. So, Appl. Phys. Lett. **87**, 113503 (2005).

[34] Y. Kawabe and J. Abe, Appl. Phys. Lett. **81**, 493 (2002).

[35] A. Kuwahara, S. Naka, H. Okada and H. Onnagawa, Appl. Phys. Lett. **89**, 132106 (2006).

[36] M. A. Baldo, S. Lamansky, P. E. Burrows, M. E. Thompson and S. R. Forrest, Appl. Phys. Lett. **75**, 4 (1999).

[37] G. F. He, M. Pfeiffer, K. Leo, M. Hofmann, J. Birnstock, R. Pudzich and J. Salbeck, Appl. Phys. Lett. **85**, 3911 (2004).

[38] R. J. Holmes, S. R. Forrest, Y. J. Tung, R. C. Kwong, J. J. Brown,S. Garon and M. E. Thompson, Appl. Phys. Lett. **82**, 2422 (2003).

[39] A. Tsuboyama, H. Iwawaki, M. Furugori, T. Mukaide, J. Kamatani, S. Igawa, T. Moriyama, S. Miura, T. Takiguchi, S. Okada, M. Hoshino and K. Ueno, J. Am. Chem. Soc. **125**, 12971 (2003).

[40] M. Y. Chan, C. S. Lee, S. L. Lai, M. K. Fung, F. L. Wong, H. Y. Sun, K. M. Lau and S. T. Lee, J. Appl. Phys. **100**, 094506 (2006).

[41] F-C. Chen, S-C Chang, G. F. He, S. M. Pyo, Y. Yang, M. Kurotaki and J. Kido, J. Polym. Sci. Pol. Phys. **41**, 2681 (2003).

[42] J. Lee, N. Chopra, S. H. Eom, Y. Zheng, J. Xue, F. So and J. Shi, Appl. Phys. Lett. **93**, 123306 (2008).

[43] M. Suzuki, S. Tokito, F. Sato, T. Igarashi, K. Kondo, T. Koyama and T. Yamaguchi, Appl. Phys. Lett. **86**, 103507 (2005).

[44] Y.-Y. Noh, C.-L. Lee, J.-J. Kim and K. Yase, J. Chem. Phys. **118**, 2853 (2003).

[45] Z. T. Liu, C. Y. Kwong, C. H. Cheung, A. B. Djurisic, Y. Chan and P. C. Chui, Synth. Met. **150**, 159 (2005).

[46] H. Razafitrimo, Y. Gao, W.A. Feld and B.R. Hsieh, Synth. Met. **79**, 103 (1996).

[47] C. Liu, X. C. Zou, S. Yin and W. X. Zhang, Thin Solid Films **466**, 279 (2004).

[48] M. A. Khan, W. Xu, K. -u. Haq, Y. Bai, Y. Jiang, Z. L. Zhang, W. Q. Zhu, Z. L. Zhang and W. Q. Zhu, J. Appl. Phys. **103**, 014509 (2008).

[49] L. Zou, V. Savvate'ev, J. Booher, C.-H. Kim and J. Shinar, Appl. Phys. Lett. **79**, 2282 (2001).

[50] J. Shinar, R. Shinar and Z. Zhou, Appl. Surf. Sci. **254**, 749 (2007).

[51] D. D. Song, S. L. Zhao, Y. C. Luo and H. Aziz, Appl. Phys. Lett. **97**, 243304 (2010).

[52] J.-M. Park, Z. Q. Gan, W. Y. Leung, R. Liu, Z. Ye, K. Constant, J. Shinar, R. Shinar and K. M. Ho, Opt. Exp. **19**, A786 (2011).

[53] S. M. Liu, B. Li, L. M. Zhang, H. Song and H. Jiang, Appl. Phys. Lett. **97**, 083304 (2010).

[54] P. D'Angelo, M. Barra, A. Cassinese, M. G. Maglione, P. Vacca, C. Minarini and A. Rubino**,** Solid State Electron. **51**, 123 (2007).

[55] M. Ooe, S. Naka, H. Okada and H. Onnagawa, Jpn. J. Appl. Phys. **45**, 250 (2006).

[56] P. E. Burrows, G. L. Graff, M. E. Gross, P. M. Martin, M. Hall, E. Mast, C. Bonham, W. Bennett, L. Michalski, M. Weaver, J. J. Brown, D. Fogarty and L. S. Sapochak, in Organic Light-Emitting Materials and Devices IV, (edited by Z. H. Kafafi), SPIE Conf. Proc. **4105**, 75 (2000).

[57] L. Moro, T. A. Krajewski, N. M. Rutherford, O. Philips,R. J. Visser, M. Gross, W. D. Bennett and G. Graff, in Organic Light Emitting Materials and Devices VII, (edited by Z. H. Kafafi, P. A. Lane), SPIE Conf. Proc. **5214**, 83 (2004).

[58] Z. Q. Zhou, R. Shinar, A. J. Allison and J. Shinar, Adv. Func. Mater. **17**, 3530 (2007).

Chapter 4. Indium-tin-oxide-free tris(8-hydroxyquinoline) Al OLEDs with 80% enhanced power efficiency

A paper published in *Applied Physics Letters*

Min Cai, Teng Xiao, Rui Liu, Ying Chen, Ruth Shinar and Joseph Shinar

Abstract

Efficient indium tin oxide (ITO)-free small molecule organic light-emitting diodes (SMOLEDs) with *multilayered* highly conductive poly(3,4-ethylenedioxy thiophene): poly(styrenesulfonate) (PEDOT:PSS) as the anode are demonstrated. SMOLEDs with the structure PEDOT:PSS/MoO_3/N,N'-diphenyl- N,N'-bis(1-naphthylphenyl)-1,1'-biphenyl-4,4'-diamine (NPD)/tris(8- hydroxyquinoline) Al (Alq_3)/ 4,7-diphenyl-1,10-phenanthroline (BPhen)/LiF/Al exhibited a peak power efficiency of 3.82 lm/W, which is 81% higher than that of similar ITO-based SMOLEDs (2.11 lm/W). The increase in the device performance is believed to be due to the advantageous higher workfunction, lower refractive index and decreased surface roughness of PEDOT:PSS as compared to ITO, as well as to Ohmic hole injection from the PEDOT:PSS to the NPD layer via the MoO_3 interlayer. The results demonstrate that a polymeric anode has the potential to substitute ITO in OLEDs with strongly improved device performance.

Introduction

Transparent electrodes are crucial for organic optoelectronics, in particular for organic light-emitting diodes (OLEDs) and organic solar cells (OSCs) [1-2]. Traditionally, this role has been well-served by indium tin oxide (ITO). However,

ITO has key issues: (i) Its ever-increasing cost due to the short supply of indium, (ii) its relatively inefficient deposition processes [3], (iii) its fragility and inflexibility that is due to its ceramic nature, which limits the processing advantages of organic devices [4], and (iv) its relatively high index of refraction ($n_{\mathrm{ITO}} \sim 2.0$), which is higher than $n_{org} \sim 1.7$ of the organic materials and $n_{gl} \sim 1.5$ of the conventional glass substrate. The high n_{ITO} contributes to the high unwanted total internal reflection at the ITO/glass interface [5]. Thus, these issues beg for alternatives to ITO. Conducting polymers [6-8], carbon nanotubes (CNTs) [9], grapheme [10], thin metals layers [11] and printable metal grids [12] are being investigated for this purpose. Conducting polymers, especially poly(3,4-ethylenedioxythiophene) (PEDOT) stabilized by aqueous poly(styrenesulfonate) acid (PSS), were used as electrodes in organic electronic devices since their inception [13,14]. However, a significant current drop, which reduced the power efficiency η_P, was observed in OLEDs with PEDOT:PSS anodes due to its relatively low conductivity ($\sigma_{\mathrm{PEDOT:PSS}} < 1$ S/cm) [8]. Hence, due to the low $\sigma_{\mathrm{PEDOT:PSS}}$ and high work function (5.1 – 5.2 eV) [15], PEDOT:PSS was used mainly as a buffer layer between ITO and the organic layers to improve hole injection or extraction in OLEDs or OSCs, respectively [15-16].

Recent studies showed that additives and blending of the aqueous PEDOT:PSS with solvents such as dimethyl sulfoxide, N,N-dimethylformamide, tetrahydrofuran, sorbitol, glycerol, or ethylene glycol (EG) improve $\sigma_{\mathrm{PEDOT:PSS}}$ by 2–3 orders of magnitude. And similar or improved OLEDs and OSCs (relative to devices with ITO) with highly conductive PEDOT:PSS anodes were reported [6-8]. Different analytical procedures and mechanistic hypotheses suggest that structural and chemical changes are responsible for the enhanced $\sigma_{\mathrm{PEDOT:PSS}}$ [8, 16-17]. In particular, for EG, recent

studies indicate that not only mixing EG and aqueous PEDOT:PSS solutions, but also immersing PEDOT:PSS films in EG solution for a few minutes increase $\sigma_{PEDOT:PSS}$ [8,16,20]. Kim *et al.*[8] reported optimized PEDOT:PSS ($\sigma_{PEDOT:PSS}$ > 1400 S/cm) used as anodes in small molecule OSCs whose power conversion efficiency was comparable to those of OSCs with ITO.

In this letter, we describe *multilayered* PEDOT:PSS (Clevios PH 1000 from H. C. Starck) films as anodes in small molecule OLEDs (SMOLEDs); such films were recently used as anodes in small molecule OSCs [8]. The ITO-free SMOLEDs were fabricated on glass substrates. Their structure was PEDOT:PSS/MoO_3/N,N'-diphenyl-N,N'-bis(1-naphthylphenyl)-1,1'-biphenyl- 4,4'-diamine (NPD)/tris(8-hydroxyquinoline)Al (Alq_3)/4,7-diphenyl-1,10-phenanthroline (BPhen)/LiF/Al. Their peak $\eta_{P,max}$ = 3.82 lm/W is 81% higher than that of the otherwise identical ITO-based devices fabricated on identical glass substrates (2.11 lm/W, which is among the highest values reported, using 10 Ω/square ITO(Ref. 18)) under equivalent conditions. This large improvement in device performance is probably due to the advantageous properties of PEDOT:PSS as well as to Ohmic hole injection from the PEDOT:PSS to the hole transport layer (HTL), achieved by inserting an ultrathin interlayer of MoO_3 [18-20]. The results clearly demonstrate that the highly conductive polymer can replace the expensive and brittle ITO, and with the proper device design enable much more efficient SMOLEDs.

Results and discussion

Devices with 1 to 4 PEDOT:PSS layers were evaluated and the device architecture and molecular structures of the various organic materials are depicted in Fig. 4-1. Table 1 summarizes the thickness, T_{550}, and $R_{\square}$ of the PDEOT:PSS and ITO films. As

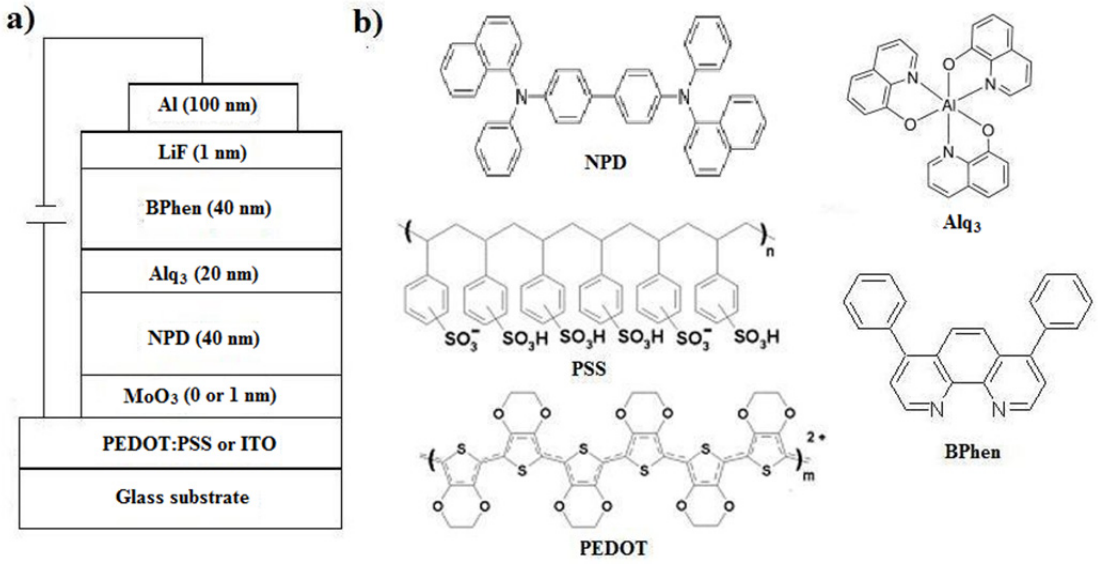

Fig. 4-1. *(a) Schematic device structures of the OLEDs and (b) chemical structures of the various OLED materials used in this study.*

seen, for the four-layer PEDOT:PSS film $R_{\square}$ = 55 Ω/□ and T_{550} = 79%; the values for

Table 1. *The thickness, transmittance, and sheet resistance of the treated PDEOT:PSS and ITO films.*

Materials	Thickness (nm)	Transmittance (%)	Sheet resistance (Ω/square)
Treated PEDOT:PSS	36	91	226
	72	87	115
	114	82	72
	149	79	55
ITO	140	92	14

the ITO film are 14 Ω/□ and 92%. The average layer thickness in the multilayer PEDOT:PSS structure is ~37 nm and, as expected, $R_{\square}$ and T_{550} decrease with increasing number of layers.

AFM images of the treated PEDOT:PSS and ITO films are shown in Fig. 4-2. The root-mean-square surface roughness R_{rms} = 2.0, 2.0, 2.5, and 3.1 nm for the treated 36, 72, 114, and 149 nm-thick PEDOT:PSS films, respectively. As clearly seen, there were small aggregates on the surface of the treated PEDOT:PSS films; they are believed to be PEDOT-rich domains, as described elsewhere [21].

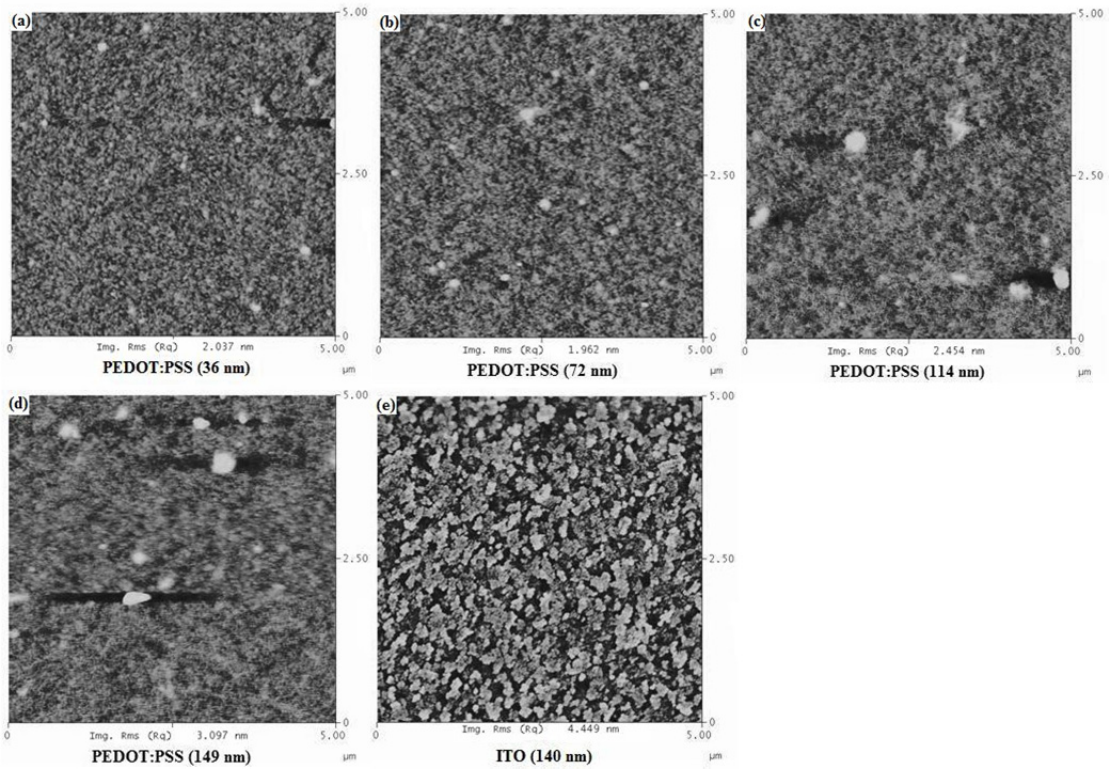

Fig. 4-2. *AFM images of thin films (a) PEDOT: PSS (36 nm), (b) two-layer PEDOT:PSS (72 nm), (c) three-layer PEDOT:PSS (114 nm), (d) four-layer PEDOT:PSS (149 nm) and (e) ITO (140 nm).*

The R_{rms} values of the PEDOT:PSS films are significantly smaller than the 4.4 nm of the ITO films. The smoother PEDOT:PSS films may improve the contact with the adjacent HTL. The higher work function (5.1 – 5.2 eV) of the PEDOT:PSS compared to that of ITO (4.5 – 4.8 eV) reduces the energy barrier for hole injection into the HTL [15], and the lower $n_{PEDOT:PSS} \sim 1.5$ vs $n_{ITO} \sim 2.0$ likely enhances the outcoupling efficiency [6,22]. Hence, the PEDOT:PSS anodes should improve hole injection and light-extraction, consequently enhancing device performance, as reported elsewhere for a single layer PEDOT:PSS (PH 500) [6]. Based on the foregoing considerations, the following Alq_3-based SMOLEDs were fabricated:

Device A: ITO/40 nm NPD/20 nm Alq_3/40 nm BPhen/1 nm LiF/100 nm Al;

Device B: *x* nm PEDOT:PSS/40 nm NPD/20 nm Alq_3/40 nm BPhen/1 nm LiF/100 nm Al;

Device C: ITO/1 nm MoO_3/40 nm NPD/20 nm Alq_3/40 nm BPhen/1 nm LiF/100 nm Al;

Device D: *x* nm PEDOT:PSS/1 nm MoO_3/40 nm NPD/20 nm Alq_3/40 nm BPhen/1 nm LiF/100 nm Al.

Here $x = 36$, 72, 114, and 149 nm.

All thicknesses of the PEDOT:PSS anodes were evaluated for Devices B and D. For Device B (no MoO_3), the 3 layer 114 nm-thick PEDOT:PSS yielded the highest η_P, but for Device D (with MoO_3), the 2 layer 72 nm-thick PEDOT:PSS yielded the highest η_P. This difference is clearly due to the improved hole injection with the

MoO_3 layer (see the discussion below). Therefore, only the results for these particular Devices B (3 layers) and D (2 layers) are shown.

Fig. 4-3(a) shows the normalized electroluminescence (EL) spectra of Devices A to D at a current density J = 57 mA/cm^2. As seen, the spectra are nearly identical, peaking at ~530 nm, and clearly originating from the Alq_3, independent of the anode.

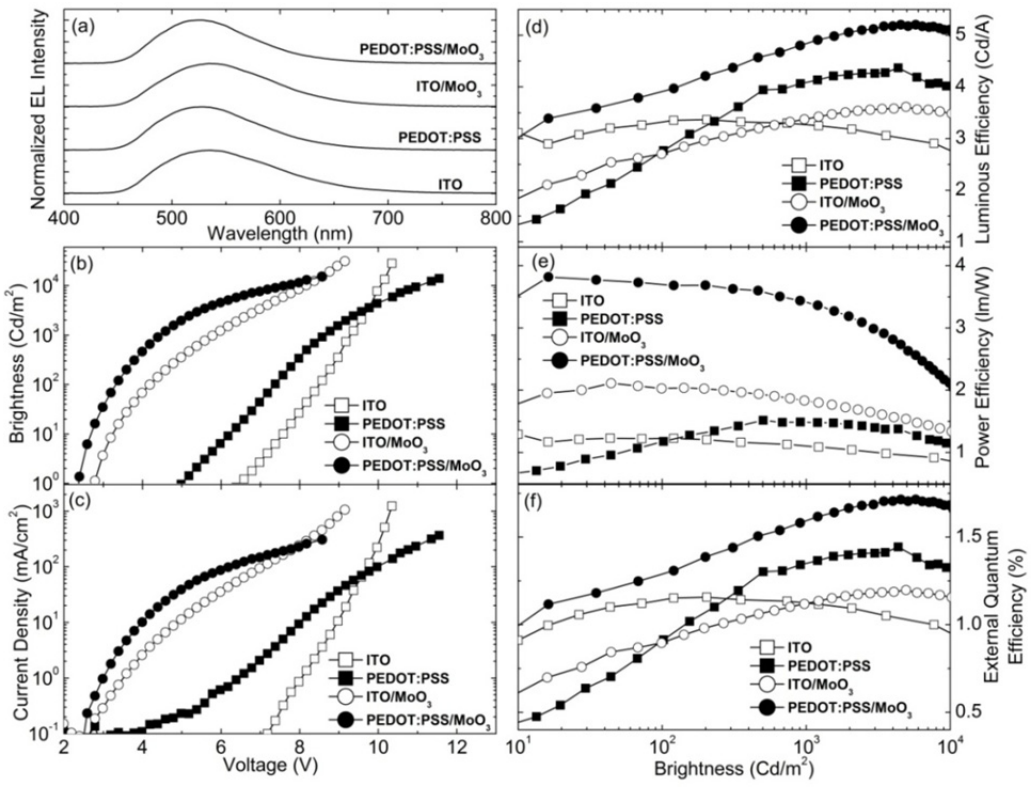

Fig. 4-3. *Comparison of device characteristics (a) EL spectra, (b) Brightness vs. voltage, (c) Current density vs. voltage, (d) Luminous efficiency vs. brightness, (e) Power efficiency vs. brightness, and (f) External Quantum Efficiency vs. brightness of Device A (solid squares), Device B (open squares; with 3 PEDOT:PSS layers), Device C(solid circles) and Device D (open circles; with 2 PEDOT:PSS layers).*

As Fig. 4-3(b) shows, all SMOLEDs show steep brightness L vs voltage V curves, indicating excellent charge-carrier injection. The turn-on voltages V_{on} (i.e., V at L = 1 Cd/m^2) with the PEDOT:PSS are lower than those with the ITO (compare Device B ($V_{on,B}$ ~ 5.0 V) to A ($V_{on,A}$ ~ 6.6 V) and Device D ($V_{on,D}$ ~ 2.3 V) to C ($V_{on,D}$ ~ 2.8 V)). In SMOLEDs without the MoO_3 this ΔV_{on} ~ 1.6 V is much larger than the work function difference $\Delta\varphi$ ~ 0.5 eV between PEDOT:PSS and ITO, suggesting that ΔV_{on} is probably also due to a poorer ITO/HTL contact, which may result from the rougher ITO surface. As expected, V_{on} of the SMOLEDs with the MoO_3 is significantly reduced. Their ΔV_{on} ~ 0.5 V is very close to $\Delta\varphi$, indicating that the MoO_3 yields Ohmic hole injection from ITO and PEDOT:PSS into NPD. This Ohmic contact is formed by electron transfer from both the anode and NPD to MoO_3. Hole injection then proceeds via electron extraction from the NPD highest occupied molecular orbital (HOMO) to the low-lying MoO_3 conduction band [18-20]. This may also explain the effect of the PEDOT:PSS thickness on optimized device performance: The reduced hole injection efficiency of Device B (no MoO_3, 3 layer PEDOT:PSS) requires thicker PEDOT:PSS (lower $R_{\square}$) to increase hole injection than Device D (with MoO_3; 2 layer PEDOT:PSS). The maximum brightness of Devices B and D are ~14,000 and ~15,000 Cd/m^2, respectively, with the latter the highest reported for OLEDs with a PEDOT:PSS anode. However, the difference in brightness between Devices C and D decreases as V increases, consistent with Fig. 4-3(c) that shows that at V > 4 V the differential resistance of the devices with PEDOT:PSS increases sharply. We note that the devices were not encapsulated, which may affect the behavior of the devices with PEDOT:PSS at high V.

Figs. 4-3(d)-(f) also show the luminous efficiency η_L (Cd/A), η_P (lm/W), and external quantum efficiency η_{EQE} (%) vs. L for Devices A-D. These further emphasize the advantages of the treated, layered PEDOT:PSS anode: η_L= 3.37, 4.37, 3.61, and 5.21 Cd/A, $\eta_{P,max}$= 1.23, 1.52, 2.11, and 3.82 lm/W, and $\eta_{EQE,max}$= 1.16, 1.44, 1.20, and 1.71% for Devices A to D, respectively. The 20-30% improvement in efficiencies from Device A to B is comparable to that reported earlier for devices with no MoO_3,[6] but in comparing Devices D and C, with MoO_3, the improvements in η_L and η_{EQE} increase to ≥43%. We suspect that these improvements result mainly from the lower $n_{PEDOT:PSS}$. Even more importantly, η_P improved by 81%, or almost twice that in η_L and η_{EQE}. This additional strong improvement in η_P is probably due to an Ohmic contact created by the MoO_3 layer [18-20].

Conclusions

In summary, we described ITO-free SMOLEDs using EG-treated multilayers of the highly conductive PEDOT:PSS as the anode, which result in strongly improved device performance. The η_P of SMOLEDs with the 3 layer (114 nm thick) PEDOT:PSS anode but no MoO_3 layer surpassed that of the SMOLEDs with ITO by ~24%. SMOLEDs with the 1 nm MoO_3 layer yielded $\eta_{P,max}$ = 3.82 lm/W when using a 2 layer (72 nm thick) PEDOT:PSS anode. This $\eta_{P,max}$ is 81% higher than similar SMOLEDs with ITO (2.11 lm/W) This strong increase in device performance is believed to result from the advantageous higher work function, lower $n_{PEDOT:PSS}$, and reduced R_{rms} of PEDOT:PSS vs ITO, and Ohmic hole injection from the anode to the HTL induced by the MoO_3 layer. The results demonstrate that PEDOT:PSS has the potential to substitute ITO in OLEDs with strongly improved device performance.

Experimental procedures

PEDOT:PSS solutions were mixed with 6 vol.% EG. The resulting solutions were filtered with 0.45 μm syringe filters and spin-coated on precleaned and UV-ozone treated glass substrates, which are identical to those used in the devices with ITO. Single PEDOT:PPS layer films were fabricated by spin coating at 3000 rpm for 30 s and annealing at 120°C for 15 min. Immediately after annealing, they were immersed and cooled in an EG bath for 30 min, then spun at 3000 rpm for another 30 s to remove the EG solution. Next, the samples were annealed at 120°C for another 15 min. For multilayer PEDOT:PSS films, the next PEDOT:PSS layer was prepared in the same way on the existing layer(s). After the PEDOT:PSS deposition was completed, the films were baked at 120°C for 1 h, then transferred into an Ar-filled glovebox (< 10 ppm O_2) and baked at 120°C for another 1 h to remove residual water. We note that the EG and heating result in layers that remain intact following subsequent spin-coating of PEDOT:PSS layers [8,16,17]. As shown below, the multilayered structure was essential for reducing its sheet resistance $R_{\square}$. ITO substrates (Colorado Concept Coatings) with $R_{\square}$ = 14 Ω/□ and 92% transmittance were used as reference diodes. The films' thickness was determined by scanning electron microscope images. The transmittance at 550 nm T_{550} (which includes the glass absorption and reflection) was obtained using an Ocean Optics CHEM2000 spectrophotometer. The films' morphology was obtained by tapping mode atomic force microscopy.

All OLEDs were fabricated in a thermal evaporation chamber within a glovebox with a base pressure of $\sim 2 \times 10^{-6}$ mbar on the glass/PEDOT:PSS or the glass/ITO substrates as detailed elsewhere [23]. The cleaned ITO substrates were treated in a

UV-ozone oven to increase their work function and hence facilitate hole injection. MoO_3 (from Sterm Chemicals) is the hole injection layer (HIL), NPD (from H. W. Sands) is the HTL, Alq_3 (from H. W. Sands) is the green emitting layer (EML), and BPhen (from Sigma-Aldrich) is the electron-transport and hole-blocking layer (ETL/HBL). These materials were used as received. MoO_3, NPD, Alq_3, BPhen, LiF, and Al layers were deposited sequentially; the Al cathode was deposited through a shadow mask containing 1.5 mm diameter circular holes.

Acknowledgements

This work was supported by the US Department of Energy, Basic Energy Sciences, Materials Sciences and Engineering Division, under Contract No. DE-AC 02-07CH11358.

References

[1] C. W. Tang and S. A. Vanslyke, Appl. Phys. Lett. **51**, 913 (1987).

[2] C. J. Brabec, Sol. Ener. Mater. Sol. Cells **83**, 273 (2004).

[3] A. Tolcin, 2008 Minerals Yearbook **35,** 1 (2009).

[4] D. R. Cairns, R. P. Witte, D. K. Sparacin, S. M. Sachsman, D. C. Paine, G. P. Crawford, and R. R. Newton, Appl. Phys. Lett. **76**, 1425 (2000).

[5] J.-M. Park, Z. Q. Gan, W. Y. Leung, R. Liu, Z. Ye, K. Constant, J. Shinar, R. Shinar, and K. M. Ho, Opt. Exp. **19**, A786 (2011).

[6] K. Fehse, K. Walzer, K. Leo, W. Lövenich, and A. Elschner, Adv. Mater. **19**, 441 (2007).

[7] S.-I. Na, S.-S. Kim, J. Jo, and D.-Y. Kim, Adv. Mater. **20**, 4061 (2008).

[8] Y. H. Kim, C. Sachse, M. L. Machala, C. May, L. M.-Meskamp, and K. Leo, Adv. Funct. Mater. **21**, 1076 (2011).

[9] M. W. Rowell, M. A. Topinka, M. D. McGehee, H. J. Prall, G. Dennler, N. S. Sariciftci, L. Hu, and G. Gruner, Appl. Phys. Lett. **88**, 233506 (2009).

[10] L. Gomez De Arco, Y. Zhang, C. W. Schlenker, K. Ryu, and M. E. Thompson, ACS Nano **4,** 2865 (2010).

[11] J. Meiss, M. Riede, and K. Leo, Appl. Phys. Lett. **94**, 013303 (2009).

[12] M. G. Kang, M. S. Kim, J. Kim, and L. J. Guo, Adv. Mater. **20**, 4408 (2008).

[13] G. Gustafsson, Y. Cao, G. M. Treacy, F. Klavetter, N. Colaneri, and A. J.Heeger, Nature **357**, 477 (1992).

[14] Y. Yang and A. J. Heeger, Appl. Phys. Lett. **64**, 1245 (1994).

[15] M. Cai, T. Xiao, E. Hellerich, Y. Chen, R. Shinar, and J. Shinar, Adv. Mater **23**, 3590 (2011).

[16] T. Xiao, W. Cui, J. Anderegg, J. Shinar, and R. Shinar, Org. Electron. **12**, 257 (2011).

[17] J. Ouyang, Q. Xua, C.-W. Chua, Y. Yang, G. Li, and J. Shinar, Polymer **45**, 8443 (2004).

[18] T. Matsushima, G.-H. Jin, and H. Murata, J. Appl. Phys. **104**, 054501 (2008).

[19] T. Matsushima, Y. Kinoshita, and H. Murata, Appl. Phys. Lett. **91**, 253504 (2007).

[20] M. Kröger, S. Hamwi, J. Meyer, T. Riedl, and W. Kowalsky, Appl. Phys. Lett. **93**, 123301 (2009).

[21] H. Okuzaki, Y. Harashina, and H. Yan, Eur. Polym. J. **45**, 256 (2009).

[22] T-W Koh, J.-M. Choi, S. Lee, and S. Yoo, Adv. Mater. **22**, 1849 (2010).

[23] Z. Q. Zhou, R. Shinar, A. J. Allison, and J. Shinar, Adv. Func. Mater. **17**, 3530 (2007).

Chapter 5. Effect of molecular weight on the efficiency of poly(*N*-vinylcarbazole)-based polymer LEDs

A paper published in *Applied Physics Letters*

Min Cai, Teng Xiao, Ying Chen, Emily Hellerich, Rui Liu,

Ruth Shinar and Joseph Shinar

Abstract

Polymer light-emitting diodes (PLEDs) based on poly(*N*-vinylcarbazole) (PVK) with molecular weights M_W of 1.1×10^6 and $\sim7.5\times10^4$ are compared. For devices without an electron transport layer (ETL), the high M_W PVK PLEDs yield higher external quantum efficiency (0.67% vs 0.18%), but for devices with an ETL, the low M_W PVK PLEDs are more efficient (1.13% vs 0.83%). This intriguing difference is believed to result from higher energetic disorder in the higher M_W polymer and different distances of the recombination zone from the quenching metal electrode, in agreement with S. J. Konezny, L. J. Rothberg, M. E. Galvin and D. L. Smith [Appl. Phys. Lett. **97**, 143305 (2010)].

Introduction

Solution-processable conjugated polymers are an important class of materials for low-cost optoelectronic applications, such as polymer light-emitting diodes (PLEDs), polymer solar cells, and polymer field effect transistors [1-6]. Conjugated polymers combine the properties of conventional polymers, such as light weight, mechanical flexibility, and processability, with semiconducting properties, such as a tunable bandgap and conductivity. However, they usually have a distribution of conjugation lengths, resulting from a distribution of defects and weight-average molecular weights

M_W [7]. The distribution of conjugation lengths (typically 8 – 15 repeat units per conjugated segment) and defects commonly leads to energetic disorder [8], which plays a crucial role in device performance [9]. In general, it is believed that higher M_W PLEDs are usually less efficient than low M_W devices due to higher energetic disorder [7].

Recently Konezny *et al.*[9] demonstrated that, surprisingly, in predominantly electron-transporting PLEDs where the recombination zone (RZ) is far from the quenching metal cathode, introducing electron traps by increasing the polymer chain length can improve device efficiency. Although increasing energetic disorder should lower the electron mobility μ_e, it can improve electron injection into lower energy trap sites and consequently the overall performance of the PLEDs. This behavior can be attributed to both closer μ_e and hole mobility μ_h and to a higher electron-hole current density product *np*. The former can lead to an improved charge balance and the latter to a higher exciton generation rate. Konezny *et al.*'s study also predicts that similar efficiency enhancement can be achieved by reducing μ_h with additional traps in devices where cathode quenching is dominant [9], as that shifts the RZ away from the cathode.

Poly(*N*-vinyl carbazole) (PVK) (see Fig. 5-1) is a well-known polymer where $\mu_h \sim 10^{-9}$ cm^2/Vs and $\mu_e << \mu_h$ [10], which is widely utilized for PLEDs emitting in the near-UV-violet-blue range [11], as well as the host for blue and longer wavelengths PLEDs.[12] In this letter we describe PLEDs based on PVKs with $M_W \approx 1.1\times10^6$ and $(7.5 \pm 2.5)\times10^4$. The results are in agreement with Konezny *et al.*[9] as they demonstrate that the larger M_W can have both negative and positive effects on PLED performance, most likely depending on the location of the RZ.

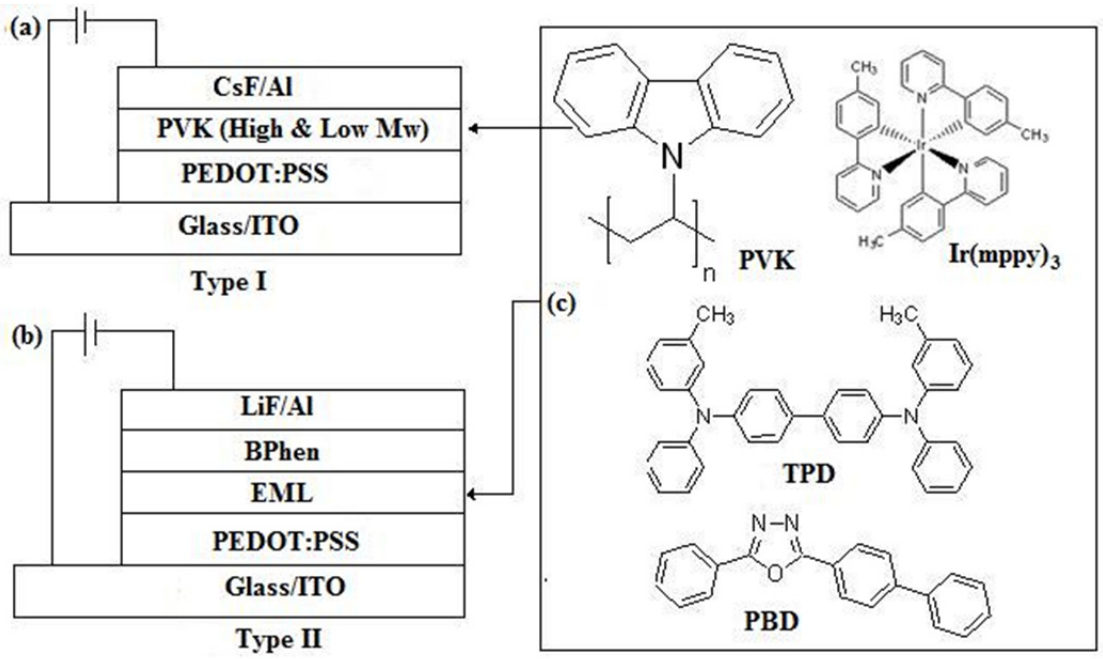

Fig. 5-1. *Device structure of (a) Type I and (b) Type II PLEDs, (c) Chemical structures of the key materials used in the PLEDs.*

Results and discussion

The PLED and material structures are shown in Fig. 5-1. The first type of PLEDs that were studied were ITO/PEDOT:PSS/PVK (high and low M_W)/CsF (1 nm)/Al (100 nm) (**Type I**) (see Fig. 5-1). Fig. 5-2 shows the EL spectra, normalized transient EL intensity vs. time t, cw brightness L and current density J vs. bias V, and external quantum efficiency η_{ext} vs. L of these devices. As clearly seen, the turn-on V (i.e., the bias V_{on} required for L = 1 Cd/m^2) are both ~4.4 V. But J of the high M_W PVK PLED is much lower than that of the low M_W PVK PLEDs throughout the whole bias range. This lower J is most likely due to the strong effects of energetic disorder on charge carrier transport. Indeed, electrochemical studies have shown that the energetic disorder in polymers increases as M_W increases [13], and this increased energetic disorder generates additional and deeper charge carrier traps [7]. Since PVK is a hole transport material, these carrier traps are presumably hole traps. In the PVK PLEDs

this would translate into more holes being trapped near the PEDOT: PSS/PVK interface in the high M_W PVK than in the low M_W polymer. Fig. 5-2(b) shows the normalized transient EL spike's amplitude in the Type I PLEDs. As clearly seen, the spike's amplitude in the high M_W PVK is ~1.34, considerably stronger than the ~1.05 amplitude in the low M_W PVK devices and entirely consistent with greater hole trapping in the high M_W PVK [14,15].

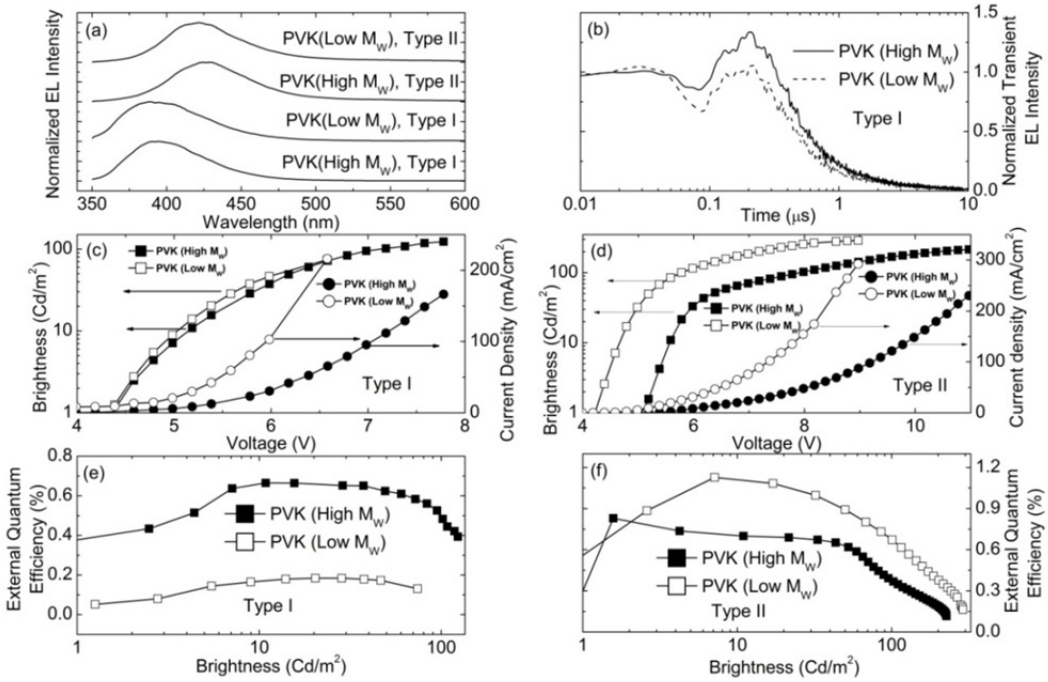

Fig. 5-2. *Comparison of device characteristics: (a) EL spectra, (b) normalized transient EL vs. time (the bias pulse ends at t = 0), (c) brightness and current density vs. voltage of device Type I, (d) brightness and current density vs. voltage of device Type II, (e) external quantum efficiency vs. brightness of device Type I, and (f) external quantum efficiency vs. brightness of device Type II. Solid symbols are for the high M_W PVK devices and open symbols are for the low M_W PVK devices.*

Greater hole trapping would obviously slow charge carrier transport in the high M_W PVK, resulting in a smaller J at any V, as observed. However, the peak η_{ext},

$\eta_{ext,\max}$ = 0.665% of the high M_W PVK PLEDs is more than 3 times that of the low M_W devices ($\eta_{ext,\max}$ = 0.184 %), demonstrating that the increased energetic disorder actually improves the efficiency, in contradiction with conventional understanding. By carefully examining the Type I device structure (Fig. 5-1(a)), this positive effect is attributed to the different RZ locations in the high and low M_W devices, in agreement with Konezny *et al.*'s analysis [9]. It is hence suspected that the reduced hole mobility in the high M_W PVK shifts the RZ toward the PEDOT:PSS. Within this scenario, in the low M_W the RZ is close to the cathode, resulting in severe EL quenching by the cathode.

To further validate the foregoing conclusions on the Type I devices, devices with the structure ITO/PEDOT:PSS/PVK (high and low M_W)/BPhen (40 nm)/LiF (1 nm)/Al (100 nm) (**Type II**, see Fig. 5-1(b)) were fabricated. The crucial difference between Type I and Type II devices is the additional 40 nm electron-transporting and hole-blocking layer (ETL/HBL) of BPhen. Most importantly, the 40-nm BPhen layer ensures that the RZ will be sufficiently distant from the cathode so EL quenching by the cathode will be negligible.

The EL spectra, *L-J-V* curves, and η_{ext} vs. L of the Type II devices are also shown in Fig. 5-2. As clearly seen in Fig. 5-2(a), the EL spectra of the high and low M_W PLEDs are the same, as Type I and Type II exhibit broad emission bands at ~400 and ~425 nm, respectively. The intriguing red-shift of the emission induced by the addition of the BPhen layer is not clear and warrants further investigation.

As clearly seen in Fig. 5-2(d), V_{on} ~ 4.2 V for the low M_W PVK is ~0.8 V lower than V_{on} ~ 5.0 V of the high M_W PVK, and J of the high M_W PVK PLEDs is still much lower throughout the whole bias range than that of the low M_W PVK PLEDs. Within the foregoing scenario, this reduction of V_{on} and higher J are, of course, due to

reduced hole trapping in the low M_W PVK. In contrast to Type I devices, $\eta_{ext,max}$ ~ 1.13% of the low M_W PVK PLEDs is higher than the 0.83% of the high M_W devices, again consistent with the negative effect of energetic disorder on efficiency in these devices where the cathode quenching effect is negligible [16].

As mentioned above, PVK is also widely used as a host material in PLEDs. In particular, previous studies showed that PVK:$Ir(mppy)_3$ PLEDs yield highly efficient phosphorescent devices, especially when electron-transporting PBD and hole-transporting TPD are co-doped with the PVK:$Ir(mppy)_3$ layer [17,18]. As the foregoing results demonstrate that for both the high and low M_W PVKs Type II PLEDs are much more efficient than Type I devices, 4 different high and low M_W PVK:$Ir(mppy)_3$ Type II PLEDs were fabricated:

Device A: ITO/PEDOT:PSS/high M_W PVK (0.94):$Ir(mppy)_3$ (0.06)/BPhen (40 nm)/LiF (1 nm)/Al (100 nm);

Device B: ITO/PEDOT:PSS/low M_W PVK (0.94):$Ir(mppy)_3$ (0.06)/BPhen (40 nm)/LiF (1 nm)/Al (100 nm);

Device C: ITO/PEDOT:PSS/high M_W PVK (0.61):TPD (0.09):PBD (0.24):$Ir(mppy)_3$ (0.06)/ BPhen (40 nm)/LiF (1 nm)/Al (100 nm);

Device D: ITO/PEDOT:PSS/low M_W PVK (0.61):TPD (0.09):PBD (0.24):$Ir(mppy)_3$ (0.06)/ BPhen (40 nm)/LiF (1 nm)/Al (100 nm).

The normalized EL spectra of Devices A-D, driven at 57 mA/cm^2, are shown in Fig. 5-3(a). As clearly seen, the spectra peak at ~510 nm, and their EL bands are nearly identical and independent of driven current. Even at very high J ~ 100 mA/cm^2, the emission from PVK, TPD or PBD is negligible—an indication of a complete energy or charge transfer from the other components of the blend to $Ir(mppy)_3$ guest molecules.

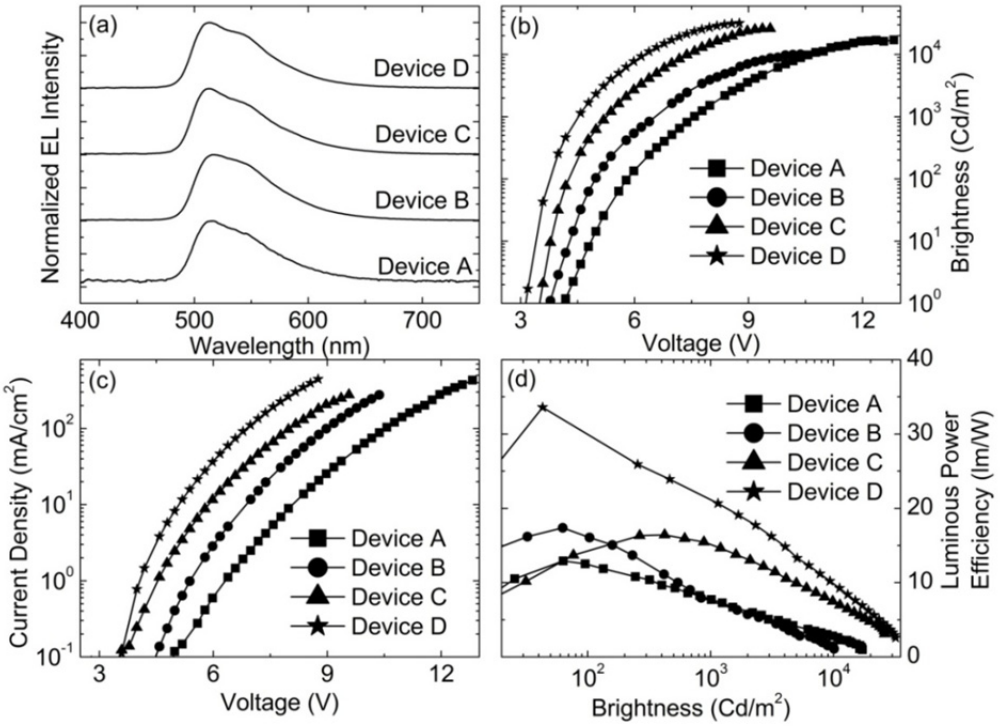

Fig. 5-3. *Comparison of device characteristics (a) EL spectra, (b) Brightness vs. voltage, (c) Current density vs. voltage and (d) Luminous power efficiency vs. brightness, of Device A (squares), Device B (circles), Device C (triangles), and Device D (stars).*

Figs. 5-3(b)-(d) show L and J vs. V and the luminous power efficiency η_{Power} vs. L. V_{on} = 4.2, 3.8, 3.5, and 3.1 V for Devices A-D, respectively, and $J_{Device\ D} > J_{Device\ C} > J_{Device\ B} > J_{Device\ A}$ throughout the whole bias range. The maximal $\eta_{Power,max}$ are 12.5, 17.4, 16.3 and 33.6 lm/W for Devices A-D, respectively.

Importantly, the comparison between Devices B and A and Devices D and C shows that the performance of the low M_W devices is clearly superior to that of the corresponding high M_W PVK: Ir(mppy)$_3$ PLEDs. This is consistent with the results on the Type II PVK-only PLEDs, indicating that the energetic disorder has a significant

negative effect η_{Power} when the metal cathode quenching effects are eliminated by the addition of the BPhen layer between the EML and metal cathode.

Conclusions

In conclusion, by comparing high and low M_W PVK and PVK:Ir(mppy)$_3$ PLEDs we have demonstrated that energetic disorder induced by an increased M_W significantly compromises device performance if cathode-quenching effects are eliminated. However, without any ETL such as a BPhen layer, the proximity of the RZ to the cathode and the ensuing cathode quenching can result in improved device efficiency in the PLEDs with greater energetic disorder. This is due to a shift in the RZ position away from the quenching cathode when μ_h is reduced by the increased energetic disorder.

Experimental procedures

The PLED and material structures are shown in Fig. 5-1. Poly(3,4-ethylenedioxythiophene): poly(4-styrenesulfonate) (PEDOT:PSS) was purchased from H. C. Starck and used as the hole injection layer (HIL). PVK, N,N'-diphenyl-N,N'-bis(3-methyl-phenyl)-[l,l'biphenyl]-4,4'-diamine (TPD), and 2-(4-biphenylyl)-5-(4-tert-butylphenyl)-1,3,4-oxadiazole (PBD), the hole- and electron-transporting molecules, respectively, and 4,7-diphenyl-1,10-phenanthroline (BPhen), an electron-transporting and hole-blocking material, were purchased from Sigma-Aldrich. Tris(2-(4-tolyl)phenylpyridine) iridium(III) (Ir(mppy)$_3$), the green-emitting phosphorescent dopant, was purchased from American Dye Source. The materials were used as received.

The ~60 nm-thick PEDOT:PSS layer was first spin coated on the precleaned and UV ozone treated indium tin oxide (ITO)/glass substrate [13] at 1000 rpm for 180 s, then baked in air at 160^{o}C for 1 hour. PVK, PVK:Ir(mppy)$_3$, and

PVK:PBD:TPD:Ir(mppy)$_3$ were dissolved in chlorobenzene and spin coated on the PEDOT:PSS layer inside a glove box(< 10 ppm O_2) at 4000 rpm for 60 s to form the emitting layer (EML) of the PLEDs. The ITO/PEDOT:PSS/EML was then annealed at 60°C for 30 min and transferred to a thermal evaporator chamber (background pressure $\sim 2 \times 10^{-6}$ mbar) where BPhen, CsF or LiF, and Al were deposited sequentially. Transient electroluminescence (EL) measurements were performed following 100 μs bias pulses that were generated by an Avtech AV-1011 power supply with nominal rise and fall times of ~10 ns [14,15]. The transient EL was monitored by a photomultiplier tube with a 50 Ω external load connected to a 350 MHz oscilloscope; see details on this measurement elsewhere [14,15].

Acknowledgements

Ames Laboratory is operated for the US Department of Energy (USDOE) by Iowa State University under Contract No. DE-AC02-07CH11358. This work was performed at the Ames Laboratory and supported by the USDOE Office of Basic Energy Science, Division of Materials Sciences and Engineering.

References

[1] *Electronic processes in organic crystals and polymers*, 2nd ed., by M. Pope and C. E. Swenberg (Oxford University Press, New York, 1999).

[2] *Semiconducting Polymers: Chemistry, Physics and Engineering*, 2nd ed., edited by G. Hadziioannou and G. G. Malliaras (Wiley, New York, 2007).

[3] J. H. Burroughes, D. D. C. Bradely, A. R. Brown, R. N. Marks, K. Mackay, R. H. Friend, P. L. Burns, and A. B. Holmes, Nature **347**, 539 (1990).

[4] X. H. Yang, D. C. Muller, D. Neher, and K. Meerholz, Adv. Mater. **18**, 948 (2006).

[5] G. Li, V. Shrotriya, J. Huang, Y. Yao, T. Moriarty, K. Emery, and Y. Yang, Nat. Mater. **4**, 864 (2005).

[6] C. D. Dimitrakopoulos, and P. R. Malenfant, Adv. Mater. **14**, 99 (2002).

[7] A. Menon, H. P. Dong, Z. I. Niazimbetova, L. J. Rothberg, and M. E. Galvin, Chem. Mater. **14**, 3668 (2002).

[8] S. J. Konezny, D. L. Smith, M. E. Galvin, and L. J. Rothberg, J. Appl. Phys. **99**, 064509 (2006).

[9] S. J. Konezny, L. J. Rothberg, M. E. Galvin, and D. L. Smith, Appl. Phys. Lett. **97**, 143305 (2010).

[10] P. D'Angelo, M. Barra, A. Cassinese, M. G. Maglione, P. Vacca, C. Minarini, and A. Rubino, Solid State Electron. **51**, 123 (2007).

[11] J. Kido, K. Hongawa, K. Okuyama, and K. Nagai, Appl. Phys. Lett. **63**, 2627 (1993).

[12] X. H. Yang, D. Neher, D. Hertel, and T. K. Daubler, Adv. Mater. **16**, 161 (2004).

[13] V. Gebhardt, A. Bacher, M. Thelakkat, U. Stalmach, H Meier, H. W. Schmidt, and D. Haarer, Adv. Mater. **11**, 119 (1999).

[14] Z. Gan, R. Liu, R. Shinar, and J. Shinar, Appl. Phys. Lett. **97**, 113301 (2010).

[15] R. Liu, Z. Gan, R. Shinar, and J. Shinar, Phys. Rev. B **83**, 245302 (2011).

[16] D. E. Markov, and P. W. M. Blom, Phys. Rev. B **72**, 161401(R) (2005).

[17] X. H. Yang, and D. Neher, Appl. Phys. Lett. **84**, 2476 (2004).

[18] S. A. Choulis, V. E. Choong, M. K. Mathai, and F. So, Appl. Phys. Lett. **87**, 113503 (2005).

[19] Z. Q. Zhou, R. Shinar, A. J. Allison, J. Shinar, Adv. Func. Mater. **17**, 3530 (2007).

Chapter 6. Blue fluorescent organic light-emitting diodes based on a new electron-accepting polymer

A paper to be submitted to *Organic Electronics*

Min Cai, Teng Xiao, Rui Liu, Ying Chen, Jeremy J. Intemann, Jared F. Mike, Malika Jeffries-El, Joseph Shinar and Ruth Shinar

Abstract

Fluorescent blue polymer light emitting diodes (PLEDs) with a new electron-accepting poly[(9,9-di-n-octylfluorene-2,7-vinylene)-2,6-diyl-benzo[1,2-d;5,4-d'] bisoxazole] (PFV*c*BBO) doped in poly(*N*-vinyl carbazole) (PVK) are described. PLEDs with different combinations of two different molecular weights (M_{WS}) of PFV*c*BBO (3,600 and 11,100) and PVK (~7.5×10^4 and 1.1×10^6) were tested. The performances of the different PLEDs are in accordance to the surface morphology of the emitting layer (EML), the smoother the EML's surface is, the better devices become. A peak 2.11 Cd/A luminous efficiency was obtained for the combination of low M_W PFV*c*BBO with the low M_W PVK host, which shows the best uniformity of EML.

Introduction

The performance of organic light-emitting diodes (OLEDs), small molecule- and polymer-based, has improved dramatically since the first thin film OLEDs were reported [1]. Intense research activities are undertaken on polymer light emitting diodes (PLEDs) due to their low-cost and roll-to-roll fabrication potential [2-4]. Within these efforts, blue OLEDs draw particular attention as a key component of white OLEDs and PLEDs are particularly promising as blue emitting devices. Two

polymer classes that have attracted significant attention are substituted poly(phenylene vinylene)s (PPVs) and poly(9,9-dialkylfluorene)s (PFOs). For example, yellow emitting poly[(2-ethylhexyloxy-5-methoxy-1,4-phenylene)vinylene] (MEH-PPV) is widely used via solution-processing [5]. Similarly, PFOs have been demonstrated as effective blue emitters with good solubility and high solid-state photoluminescence (PL) quantum efficiency $\eta_{PL} \sim 72\%$ [6]. However, like most conjugated polymers, the electron mobility μ_e of PFOs is much lower ($\geq$ 100 fold) than the hole mobility μ_h [7,8]. To meet the need for balanced hole and electron transport properties in a single polymer, which is essential to achieving efficient single-layer OLEDs, a common strategy is to use emissive copolymers containing both hole-transporting and electron-transporting moieties [9-13]. As an example, PLEDs based on a copolymer, poly(fluorenevinylene-*alt*-diphenyloxadiazole), which contains electron-accepting oxadiazole units and electron-donating triphenylamine units, have been reported [11].

We recently described the new blue electron-transporting polymer poly[(9,9- di-n-octylfluorene-2,7-vinylene)-2,6-diyl-benzo[1,2-d;5,4-d']bisoxazole] (PFV*c*BBO) [14]. This polymer is based on poly(*p*-phenylene benzobisoxazole), which is known to have a high electron affinity [12], efficient electron transport [15], and strong PL in solution [14,16-18]. The combination of the electron-transporting benzobisoxazole and 9,9-dialkyl fluorene moieties into one polymer backbone results in a new emissive, high electron-affinity polymer. Preliminary PLEDs based on this polymer doped in poly(*N*-vinyl carbazole) (PVK) emitted sky-blue luminescence with a peak luminous efficiency $\eta_{L,max} = 0.93$ Cd/A [14].

In this paper, in an attempt to improve the PLEDs' performance, various devices were fabricated by using combinations of two different molecular weights M_{WS} of the PFV*c*BBO dopant (3,600 and 11,100) and the PVK host (~7.5×10^4 and 1.1×10^6). Additionally, the electron transporting 2-(4-biphenylyl)-5-(4-tert-butylphenyl)-1,3,4-oxadiazole (PBD) and hole transporting N,N'-diphenyl-N,N'-bis(3-methyl-phenyl)-[l,l'biphenyl]-4,4'- diamine (TPD) were mixed with the dopant and host, to improve the charge carrier transport [19-24]. It was found that the best performance of the PLEDs was obtained when combining low M_W PFV*c*BBO with the low M_W PVK host. This behavior was likely due to the lowest surface roughness of the emitting layer, as observed by atomic force microscopy (AFM). A $\eta_{L,max}$ = 2.11 Cd/A was obtained for this PLED with the electroluminescence (EL) peaking at ~470 nm, which is 127% improvement compared to previous reported results [14].

Results and discussion

As reported previously [14], the fluorescence yield η_{PL} of PFV*c*BBO in the solid state is only ~0.01, however, in the THF solution η_{PL} is ~0.64, which makes it a promising candidate for use in guest-host PLEDs. We therefore tested it as a low-level dopant in the following devices:

Device A: ITO/PEDOT:PSS/PVK(high M_W):TPD:PBD:PFV*c*BBO(high M_W)/BPhen/LiF/Al,

Device B: ITO/PEDOT:PSS/PVK(low M_W):TPD:PBD:PFV*c*BBO(high M_W)/BPhen/LiF/Al,

Device C: ITO/PEDOT:PSS/PVK(high M_W):TPD:PBD:PFV*c*BBO(low M_W)/BPhen/LiF/Al, and

Device D: ITO/PEDOT:PSS/PVK(low M_W):TPD:PBD:PFV*c*BBO(low M_W)/BPhen/LiF/Al.

The concentrations of TPD and PBD were fixed at 10 and 25 wt.%, respectively.[19-21] The device structures and the highest occupied molecular orbital (HOMO) and lowest unoccupied molecular orbital (LUMO) energy levels for the different materials constituting these devices are shown in Fig. 6-1 [14,19-21,25].

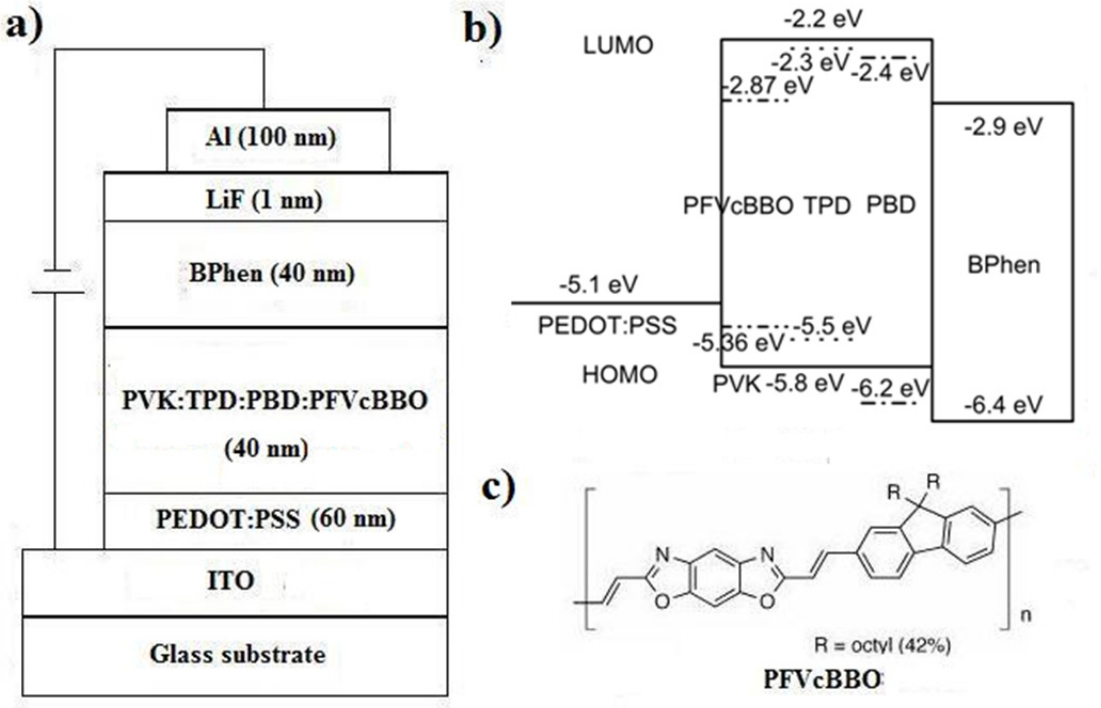

Fig. 6-1. *(a) OLED device architecture, (b) the HOMO and LUMO energy levels of the PFVcBBO, PVK, TPD, PBD and BPhen together with the work function of PEDOT:PSS (all referenced with respect to the vacuum) and (c) the chemical structure of PFVcBBO.*

Three different concentrations of PFVcBBO (1, 2, 4 wt.%) were doped into Devices A to D. Devices with the lowest doping level (1 wt.%) yielded the best performance, probably due to strong concentration-quenching of the PFV*c*BBO emission at the higher concentrations. BPhen was used as the electron-transporting layer ($\mu_e \sim 2.8\times10^{-4}$ cm^2/Vs) [26], and a buffer to prevent exciton quenching by the

metal cathode. As previously established [14], the optimal thickness of such a layer is ~40 nm. Therefore only results on Devices A to D with 1 wt.% dopant and a 40-nm thick BPhen layer are shown in Fig. 6-2.

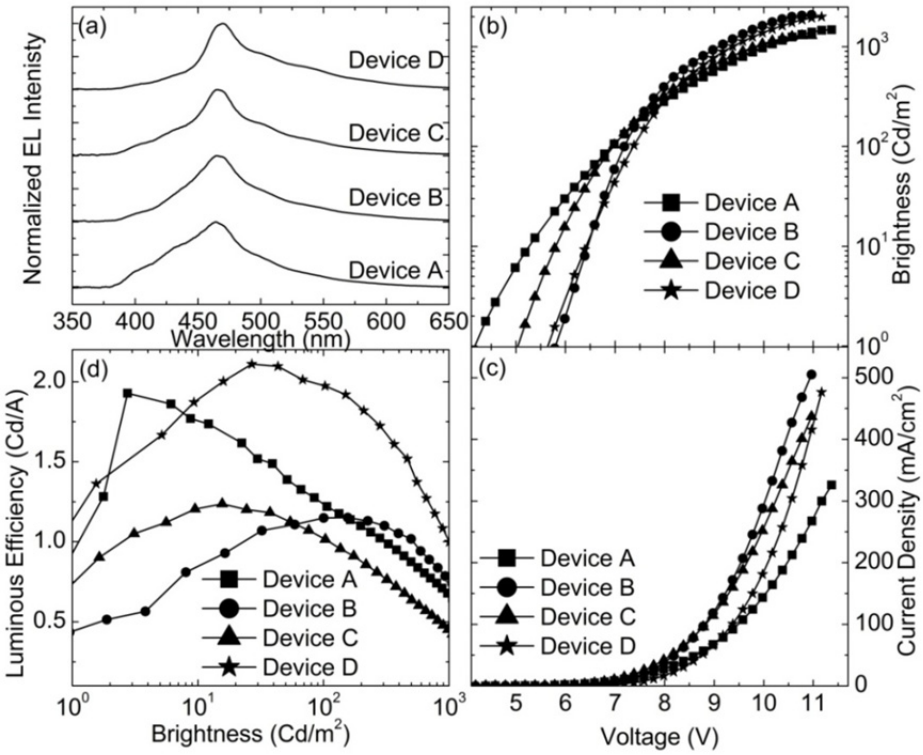

Fig. 6-2. *Comparison of device characteristics (a) EL spectra, (b) Brightness vs. voltage, (c) Current density vs. voltage, (d) Luminous efficiency vs. brightness of Device A (squares), Device B (circles), Device C (triangles) and Device D (stars).*

The normalized EL spectra of Devices A to D, driven at 57 mA/cm^2, are shown in Fig. 6-2(a). As clearly seen, the EL spectra peaked at ~470 nm. Hence, the EL originates from the PFVcBBO polymer, indicating an energy or charge transfer from the other components of the blend to the PFVcBBO.

Figs. 6-2(b)-(d) show the brightness L and current density J vs. the bias voltage V, and the luminous efficiency η_L (in Cd/A) vs. L for Devices A to D. The $\eta_{L,max}$ are 1.93,

1.15, 1.24 and 2.11 Cd/A for Devices A to D, respectively. Thus, as expected, as a result of the improved charge balance and transport due to the high hole mobility of TPD ($\mu_h \sim 10^{-3}$ cm^2/Vs) [22] and high electron mobility of PBD ($\mu_e \sim 2\times10^{-5}$ cm^2/Vs) [23], the values of $\eta_{L,max}$ for Devices A to D are all better than the previously reported $\eta_{L,max}$ (0.93 Cd/A) [14], in particularly for Device D, there is a significant 127% improvement.

To further determine the possible effect of morphology on device performance, we examined the EML films by atomic force microscopy (AFM); the images are shown in Fig. 6-3. As seen, all films show pinhole-free surfaces.

Figs. 6-3(a)-(d) show the root mean square roughness R_{rms} of the spin-coated emissive films of Devices A to D, respectively. The R_{rms} values of these films are 0.52, 0.70, 0.61 and 0.43 nm, respectively. It is clearly that the PLEDs' performance is related to the surface roughness of the EML. As expected, the smaller the R_{rms} value of the EML films, the higher the value of $\eta_{L,max}$ for the devices. The most efficient Device D shows the lowest value of the surface roughness.

As we known, the surface roughness of the films made by blends can be affected by so many different factors [27-28]. In order to get a very smooth film by spin-coating the blends' solutions, the first thing is to achieve a high homogeneous mixing in the blends' solution. Usually the higher the homogeneity of mixture in the solutions is, the better the films will be. This can be strongly affected by the different solubility of the components in the blends. After the solutions are spin-casted, another factor which would determine the surface roughness of the films is the formation of phase separation between the different components in the blends [24,29-30]. This can lead to aggregation of e.g., the dopant molecules, which would then increase the surface

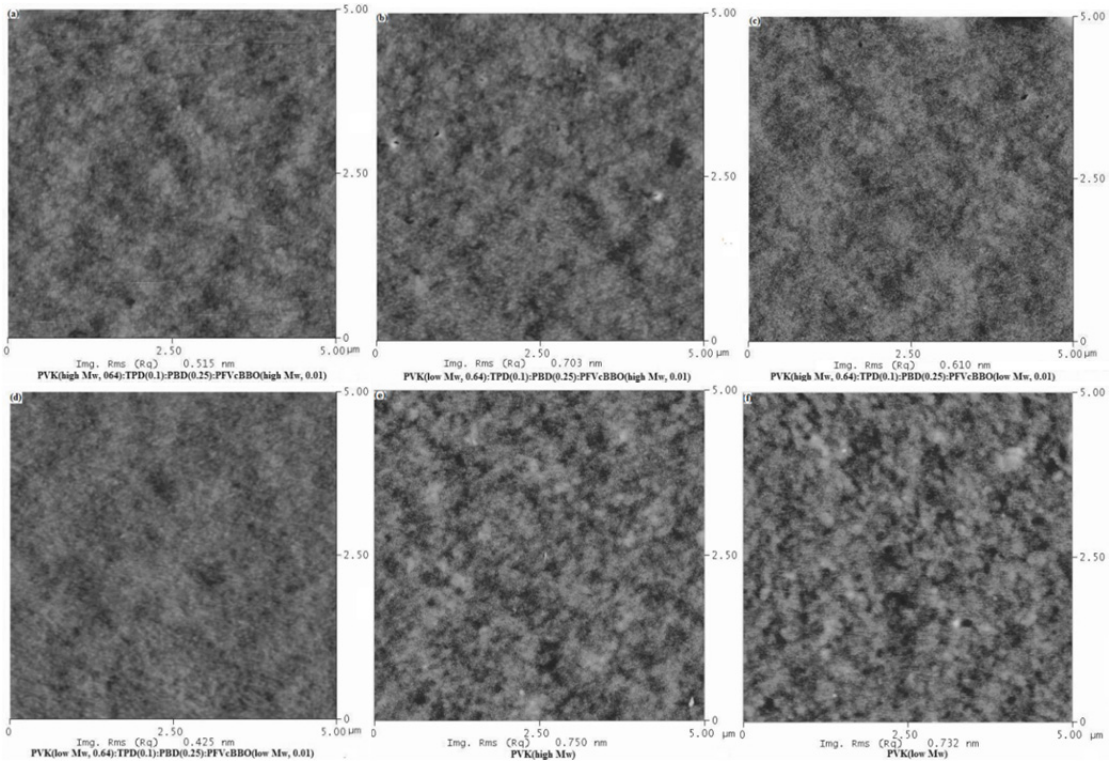

Fig. 6-3. *AFM images of thin films of (a) PVK(high M_W, 0.64):TPD(0.10):PBD(0.25):PFVcBBO (high M_W, 0.01) (b) PVK(low M_W, 0.64):TPD(0.10):PBD(0.25):PFVcBBO (high M_W, 0.01), (c) PVK(high M_W, 0.64):TPD(0.10):PBD(0.25):PFVcBBO (low M_W, 0.01), (d) PVK(low M_W, 0.64):TPD(0.10):PBD(0.25):PFVcBBO (low M_W, 0.01), (e) PVK(high M_W) and (f) PVK(low M_W).*

roughness. The compatibility of the blend's constituents in terms of physical attributes such as M_{WS}, vapor pressures, and structures are important in determining the degree of phase separation [24.29-30].

In this study, the two M_W PVKs show almost no difference in the solubility, especially at the low concentration (9 mg/mL) used for the solutions. But after the spin-coating, the high M_W PVK might simply lead to higher degrees of crystallinity which can increase the formation of phase separation between the different

components in the blend. On the other hand, the low M_W PVK is more amorphous and smooth compared to the high M_W PVK, so the effect of the phase separation is not that strong as for the low M_W PVK. However, for the dopant PFVcBBO, the difference in solubility between the high and low M_{WS} is quite significant. The low M_W one has much better solubility than the high M_W one due to its smaller polymer chains. So the low M_W PFVcBBO could diffuse better in the PVK matrix in the solution, which would increase the homogeneity of the PFVcBBO:PVK mixture. For low M_W PVK as the host's PLEDs, namely Devices B and D, the effect of phase separation is reduced due to property of the low M_W PVK. Therefore in these devices, the surface roughness of films are more dominant by the homogeneity of the PFVcBBO:PVK mixture. The low M_W PFVcBBO has better solubility, which leads to more homogenous mixture, then results in a much smoother surface roughness ($R_{rms,\ Device\ D}$ ~ 0.43 nm vs. $R_{rms,\ Device\ B}$ ~ 0.70 nm) and higher devices performance ($\eta_{L,max,\ Device\ D}$ ~ 2.11 Cd/A vs. $\eta_{L,max,\ Device\ B}$ ~ 1.15 Cd/A). For high M_W PVK as the host's PLEDs, namely Devices A and C, the effect of phase separation is increased due to property of the high M_W PVK. As shown in our previous work [24], the less difference between the components' physical properties, i.e., less M_W difference, in the blends would lead to less phase separation, which would result in much smoother surface in the films. Since the high M_W PFVcBBO has less M_W difference with the high M_W PVK, there is less formation of phase separation in the high M_W PFVcBBO's PLEDs (Device A) compared to the low M_W PFVcBBO's PLEDs (Device C). Less phase separation would leads to smoother surface roughness ($R_{rms,\ Device\ A}$ ~ 0.52 nm vs. $R_{rms,\ Device\ C}$ ~ 0.61 nm), which results in higher devices efficiency ($\eta_{L,max,\ Device\ A}$ ~ 1.93 Cd/A vs. $\eta_{L,max,\ Device\ C}$ ~ 1.24 Cd/A).

We also fabricated PVK-only PLEDs as reference devices. By comparing the PFVcBBO- doped devices to the undoped ones, it is seen, as expected, that the dopant is responsible for the improved device performance. In the doped devices the major EL peak (~470 nm) is largely that of the dopant (see Fig. 6-2(a)) and the efficiencies are clearly increased. For example, the peak external quantum efficiency $\eta_{EQE,max}$ in the PVK-only devices is 0.78%; which increases two-fold to 1.64% in Device D. The R_{rms} of spin-coated high and low M_W PVK films are 0.75 and 0.73 nm, respectively, as shown in Figs. 6-3(e) and (f). These two values are very close, which indicates that the differences in the R_{rms} values shown in Figs. 6-3(a)-(d) are certainly caused by doping with the different M_W PFVcBBO.

Finally, similar PFV*c*BBO-doped small molecule 4,4'-bis(9-carbazolyl)biphenyl (CBP)-based spin-coated OLEDs were fabricated. Unlike the recently reported results [24], the CBP-based OLEDs exhibited lower efficiencies than the PVK-based PLEDs. For example, the $\eta_{L,max}$ for the high and low M_W PFVcBBO in the CBP-based OLEDs, whose structure was: ITO/PEDOT:PSS/spin-coated CBP(0.64):TPD(0.1):PBD(0.25):PFV*c*BBO(high or low M_W, 0.01)/BPhen/LiF/ Al, were 0.88 and 1.80 Cd/A, respectively. These values are lower than those of the PVK-based PLEDs, which is probably due to increased phase separation between the polymer dopant and the small molecule host.

Conclusions

In summary, a new blue-emitting electron-accepting polymer, PFV*c*BBO, was successfully used as a dopant in the solution-processed PVK-based fluorescent PLEDs. PLEDs fabricated by doping two different M_{WS} of PFV*c*BBO (3,600 and 11,100) into two different M_{WS} of the PVK host (~7.5×10^4 and 1.1×10^6) were

demonstrated. It is clear that the PLEDs' performance is correlated with the roughness of the emitting layer, with the best device having the smoothest layer. This behavior is likely due to the reduced phase separation in the polymer:polymer blends. However, a correlation with the M_{WS} could not be established. By blending the emissive PVK:PFV*c*BBO with electron transporting PBD and hole transporting TPD, the $\eta_{L,max}$ was improved to 2.11 Cd/A in Device D. The $\eta_{L,max}$ of Device A was 1.93 Cd/A, a 108% improvement compared to a previously reported result of 0.93 Cd/A, for a similar blend but without TPD and PBD. These strong increases in device performance are a result of improved balance of the charge injection and transport in the EML by the high hole mobility TPD and the high electron mobility PBD together the smoother surfaces of the EMLs.

Experimental procedures

Poly(3,4-ethylenedioxy thiophene):poly(4-styrenesulfonate) (PEDOT:PSS) was purchased from H. C. Starck and used as the hole injection layer (HIL). PVK, the host material with $M_{WS} \approx 1.1\times10^6$ and $(7.5 \pm 2.5)\times10^4$; TPD and PBD, the hole- and electron-transporting moieties, respectively; and BPhen, an electron-transporting and hole-blocking material, were purchased from Sigma-Aldrich. These materials were used without further purification. PFV*c*BBO, the dopant material, whose the chemical structure is shown in Fig. 6-1(c), was synthesized using a procedure described by Intemann *et al.* [14].

A ~60 nm PEDOT:PSS was first spin coated at 1000 rpm for 180 s on the precleaned and UV-ozone treated ITO/glass substrate and then baked in air at 160°C for 1 hour. The PVK, and PVK:PBD:TPD:PFV*c*BBO blends in chlorobenzene (9 mg/mL) were spin coated on top of the PEDOT:PSS layer inside the glove box (< 10

ppm O_2) at 4000 rpm for 60 s to form the emission layer (EML). The EML was then annealed at 60°C for 30 min. Following the spin coating step, the films were transferred to a thermal evaporation chamber and BPhen, LiF, and Al layers were deposited sequentially at a typical pressure of $\sim 2 \times 10^{-6}$ mbar. Bias voltages across the OLEDs were supplied by a Kepco DPS 40-2M programmable power supply and the current was measured using a Keithley 2000 multimeter. The EL of the OLEDs was measured by a Minolta LS110 luminance meter and the EL spectra were obtained using an Ocean Optics CHEM2000 spectrometer.

Acknowledgements

Ames Laboratory is operated by Iowa State University for the US Department of Energy (USDOE) under Contract No. DE-AC 02-07CH11358. This work was performed at the Ames Laboratory and supported by the USDOE Office of Basic Energy Science, Division of Materials Sciences and Engineering.

References

[1] C. W. Tang and S. A. Vanslyke, Appl. Phys. Lett. **51**, 913 (1987).

[2] W. Wu, M. Inbasekaran, M. Hudack, D. Welsh, W. Yu, Y. Cheng, C. Wang, S. Kram, M. Tacey, M. Bernius, R. Fletcher, K. Kiszka, S. Munger and J. O'Brien, Microelectronics J. **35**, 343 (2004).

[3] A. P. Kulkarni, C. J. Tonzola, A. Babel and S. A. Jenekhe, Chem. Mater. **16**, 4556 (2004).

[4] L. Akcelrud, Prog. Polym. Sci. **28**, 875 (2003).

[5] D. Braun and A. J. Heeger, Appl. Phys. Lett. **58**, 1982 (1991).

[6] A. P. Kulkarni, Y. Zhu and S. A. Jenekhe, Macromolecules **38**, 1553 (2005).

[7] S. R. Tseng, Y. S. Chen, H. F. Meng, H. C. Lai, C. H. Yeh, S. F. Horng, H. H. Liao and C. S. Hsu, Synth. Met. **159**, 137 (2009).

[8] A. Babel and S. A. Jenekhe, Macromolecules **36,** 7759 (2003).

[9] E. Ahmed, F. S. Kim, H. Xin and S. A. Jenekhe, Macromolecules **42**, 8615 (2009).

[10] A. C. Grimsdale, K. Leok Chan, R. E. Martin, P. G. Jokisz, and A. B. Holmes, Chem. Rev. **109**, 897 (2009).

[11] J. A. Mikroyannidis, K. M. Gibbons, A. P. Kulkarni and S. A. Jenekhe, Macromolecules **41**, 663 (2008).

[12] C.-F. Shu, R. Dodda, F.-I. Wu, M. S. Liu and A. K.-Y. Jen, Macromolecules **36**, 6698 (2003).

[13] J. A. Mikroyannidis, M. Fakis and I. K. Spiliopoulos, Poly. Sci. A. **47**, 3370 (2009).

[14] J. J. Intemann, J. F. Mike, M. Cai, S. Bose, T. Xiao, T. C. Mauldin, J. Shinar, R. Shinar and M. Jeffries-EL, Macromolecules **44**, 248 (2011).

[15] A. Babel and S. A. Jenekhe, Adv. Mater. **14**, 371 (2002).

[16] Y. Chen, S. Wang, Q. Zhuang, X. Li, P. Wu and Z. Han, Macromolecules **38**, 9873 (2005).

[17] D. Feng, S. Wang, Q. Zhuang, P. Wu and Z. Han, Polymer **45**, 8871 (2004).

[18] X. Zhang and S. A. Jenekhe, Macromolecules **33**, 2069 (2000).

[19] X. H. Yang, D. Neher, D. Hertel and Th. K. Daubler, Adv. Mater. **16**, 161 (2004).

[20] X. H. Yang and D. Neher, Appl. Phys. Lett. **84**, 2476 (2004).

[21] S. A. Choulis, V. E. Choong, M. K. Mathai and F. So, Appl. Phys. Lett. **87**, 113503 (2005).

[22] A. Kuwahara, S. Naka, H. Okada and H. Onnagawa, Appl. Phys. Lett. **89**, 132106 (2006).

[23] Y. Kawabe and J. Abe, Appl. Phys. Lett. **81**, 493 (2002).

[24] M. Cai, T. Xiao, E. Hellerich, Y. Chen, R. Shinar and J. Shinar, Adv. Mater. **23**, 3590 (2011).

[25] S. Naka, H. Okada, H. Onnagawa and T. Tsutsui, Appl. Phys. Lett. **76**, 197 (2000).

[26] M. A. Khan, W. Xu, K. -u. Haq, Y. Bai, Y. Jiang, Z. L. Zhang, W. Q. Zhu, Z. L. Zhang and W. Q. Zhu. J. Appl. Phys. **103**, 014509 (2008).

[27] M. Geoghegan and G. Krausch. Prog. Polym. Sci. **28**, 261 (2003).

[28] L. Duan, L. Hou, T.-W. Lee, J. Qiao, D. Zhang, G. Dong, L. Wang and Y. Qiu, J. Mater. Chem. **20**, 6392 (2010).

[29] H. Razafitrimo, Y. Gao, W.A. Feld and B.R. Hsieh, Synth. Met. **79**, 103 (1996).

[30] C. Liu, X. C. Zou, S. Yin and W. X. Zhang, Thin Solid Films **466**, 279 (2004).

Chapter 7. PLDMR study of rubrene and oxygen-doped rubrene films and powders

A paper published in the *2009 SPIE Conference Proceedings*

Min Cai, Ying Chen, Oleg Mitrofanov, Christian Kloc,

Arthur P. Ramirez and Joseph Shinar

Abstract

A comprehensive photoluminescence (PL)-detected magnetic resonance (PLDMR) study of various vacuum-sealed 5,6,11,12-tetraphenyl-tetracene (rubrene) films and powders is described. Three PLDMR features are observed and analyzed: (i) A negative (PL-quenching) triplet exciton (TE) resonance at $T > 50$K, due to reduced spin-dependent fusion of geminate TE pairs to singlet excitons (SEs). (ii) A positive (PL-enhancing) triplet resonance at $T < 50$K. This resonance is suspected to result from reduced quenching of SEs by a reduced population of polarons and nongeminate TEs, the latter due to the spin-dependent annihilation of TEs by polarons. (iii) A negative (PL-quenching) spin 1/2 (polaron) resonance, believed to be due to enhanced formation of trions, i.e., bipolarons stabilized by a countercharge, at oxygen centers. As single crystal thin films of oxygen-doped rubrene exhibit exceptionally high room-temperature carrier mobility, the relation between this negative resonance and the transport properties is also discussed.

Introduction

Among π-conjugated materials, tetracenes and their derivatives, notably 5,6,11,12-tetraphenyl-tetracene (rubrene) (Fig. 7-1), are unusual in their electronic structure: The energy of their low lying triplet exciton (TE) state E_{TE} is approximately one half

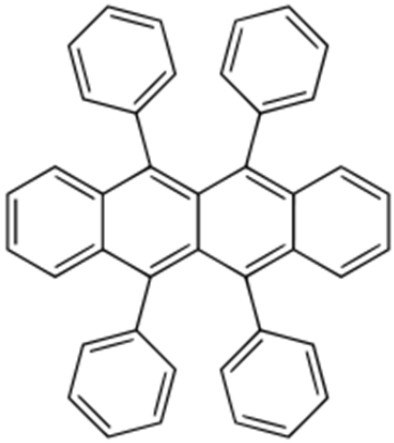

Fig. 7-1. *The molecular structure of rubrene.*

that of the low-lying singlet exciton (SE) state E_{SE} [1]. Consequently, in neat rubrene films or powders SEs efficiently fission to pairs of TEs, reducing the photoluminescence (PL) quantum yield η_{PL} of such films and powders to ~10%, from 100% in dilute solutions. At the same time, rubrene films and powders also exhibit a relatively strong delayed fluorescence due to relatively efficient fusion of such TEs (back) to SEs.

Rubrene is also an attractive dopant in fluorescent OLEDs: When doped into either N,N'-diphenyl-N,N'-bis(1-naphthylphenyl)-1,1'-biphenyl-4,4'-diamine (NPD) hole transport layers or tris(8-hydroxyquinoline) Al (Alq_3) electron transport layers, it enhances the efficiency and stability of the devices [2,3]. In the former, this is suspected to result from an increased glass transition temperature; in the latter, from efficient trapping of holes, which chemically destabilize Alq_3 [4]. When doped either into green Alq_3 or blue 4,4'-bis(2,2'-diphenylvinyl)-1,1'-biphenyl (DPVBi) OLEDs, it shifts the emission to orange-red; in the latter case it enables extremely bright and efficient (relative to other fluorescent devices) white OLEDs [3].

Rubrene has also drawn attention recently due to reports that oxygen-doped single crystals of this material exhibit the highest room temperature field effect transistor (FET) mobility, up to 20 cm^2/Vs, among all π-conjugated materials [5-7]. Hence, studies that provide insight into the role of the oxygen center in this material are highly desirable. A detailed study of the PL of oxidized rubrene crystals demonstrated a low-energy PL band that reflects an additional recombination path at an oxygen-related gap state [8]. The study also indicated that the oxygen-induced state is responsible for the rise in dark- and photo-conductivity. The authors proposed a model in which that state is a deep acceptor state, which, inter alia, enhances the exciton dissociation rate.

PL- and photoinduced absorption (PA)-detected magnetic resonance (PLDMR and PADMR, respectively) studies of luminescent π-conjugated materials, and electroluminescence (EL)- and electrical current-detected magnetic resonance (ELDMR and EDMR, respectively) studies of OLEDs, have yielded such insight [9-30]. In general, they have revealed three typical resonances:

(i) A positive (PL-, EL-, and current-enhancing, and PA-quenching) spin 1/2 resonance, due to reduced quenching of singlet excitons (SEs) by a reduced triplet exciton (TE) and polaron population [14,16-21,25-29]. The reduction in the TE and polaron populations is due to the well-known mechanism of enhancement of the spin-dependent annihilation of TEs by polarons [1, 27,28,31-39]. As a polaron annihilates a TE, it absorbs the TE energy and becomes detrapped, thereby increasing its own recombination rate [28].

(ii) A negative (PL-, EL-, and current-quenching) spin 1/2 resonance, due to enhanced formation of trions, which are bipolarons stabilized by a counterpolaron or counterion,

and which results in reduced current as more carriers become trapped in such sites, and enhanced quenching of SEs by such trions [13,15,16,25,26,29].

(iii) Positive full- and half-field spin 1 TE resonances that are due to reduced quenching of SEs by a reduced population of TEs and polarons, i.e., the same mechanism as that of the positive spin 1/2 resonance [13,21,28].

Peculiar to rubrene (and due to the fact that $E_{TE} \approx E_{TE}/2$) is a fourth resonance, which was studied many years ago by Frankevich and coworkers [9,10]: *(iv)* A negative spin 1 TE resonance. As suggested in those studies, the negative TE resonance is due to reduced spin-dependent fusion of geminate pairs of TEs that are generated by fission of a SE to two TEs. As the pair of TEs is geminate, within the spin-lattice relaxation time $T_{1,TE}$ the configuration of such pairs is predominantly a singlet configuration. As it appears that $T_{1,TE}$ is typically very long in π-conjugated materials [40], magnetic resonance conditions would reduce the number of pairs in the singlet configuration, and increase the number of pairs in the triplet and quintuplet configurations, which are forbidden from fusing back to a SE due to the spin conservation requirement. This would obviously result in a negative change in the PL.

This paper describes a comprehensive PLDMR study of rubrene films, including films carefully protected from oxygen contamination, unprotected films, and films intentionally doped with oxygen. As mentioned, it confirms the existence of the negative triplet resonance observed by Frankevich and coworkers [9,10]. However, it also reveals a low-temperature positive spin 1 TE resonance, possibly due to the mechanism *(iii)* mentioned above, and, most importantly, a negative oxygen-induced spin 1/2 resonance. Similar to the other negative spin 1/2 resonances mentioned in item *(ii)*, this resonance is believed to result from enhanced formation of trions at oxygen centers, in this case positive bipolarons stabilized by a negative polaron

trapped at an oxygen site. Such a conclusion suggests, in turn, that these trions do not adversely affect carrier transport in oxygen-doped rubrene. In fact, they may enhance it. Indeed, such an enhancement has been proposed to be due to bipolaron formation [41], but its nature was not well understood. This work, in combination with the study by Mitrofanov *et al.* [8], offers a possible explanation for this enhancement: The trion is likely a strong exciton dissociation center, and thereby converts such excitons into carriers that contribute to the conductivity.

Results and discussion

a) The PL spectra

Fig. 7-2(a) shows the PL spectra of fresh (nominally oxygen free) rubrene films at various temperatures. The spectra are in reasonable agreement with those obtained by Mitrofanov *et al.* [8], and clearly show the three main bands, band I is at 570 nm (2.18 eV), band II is at 590 nm (2.10 eV) and band III is at 608 nm (2.04 eV) . Compared with Band I and III, Band II is weaker and it starts to disappear when T >60 K. When T >180 K, three individual bands merge together to be a broad band. The PL intensity decreases as the temperature T increases from 20 to 300 K, in agreement with Mitrofanov *et al.* [8].

Fig. 7-2(b) shows the spectra of aged (unintentionally oxygen-doped) rubrene powders at various temperatures. An additional PL band I' red shifted by about 40 meV from the band I is clearly seen at 60 K. As the temperature increases to ~60 K, strong emission at 642 nm (1.93 eV) appears in the spectrum. This is a new PL band and which is due to the oxygen impurity center. The new band O remains the main spectral signature of the aged (unintentionally oxygen-doped) rubrene powders at temperatures above 240 K.

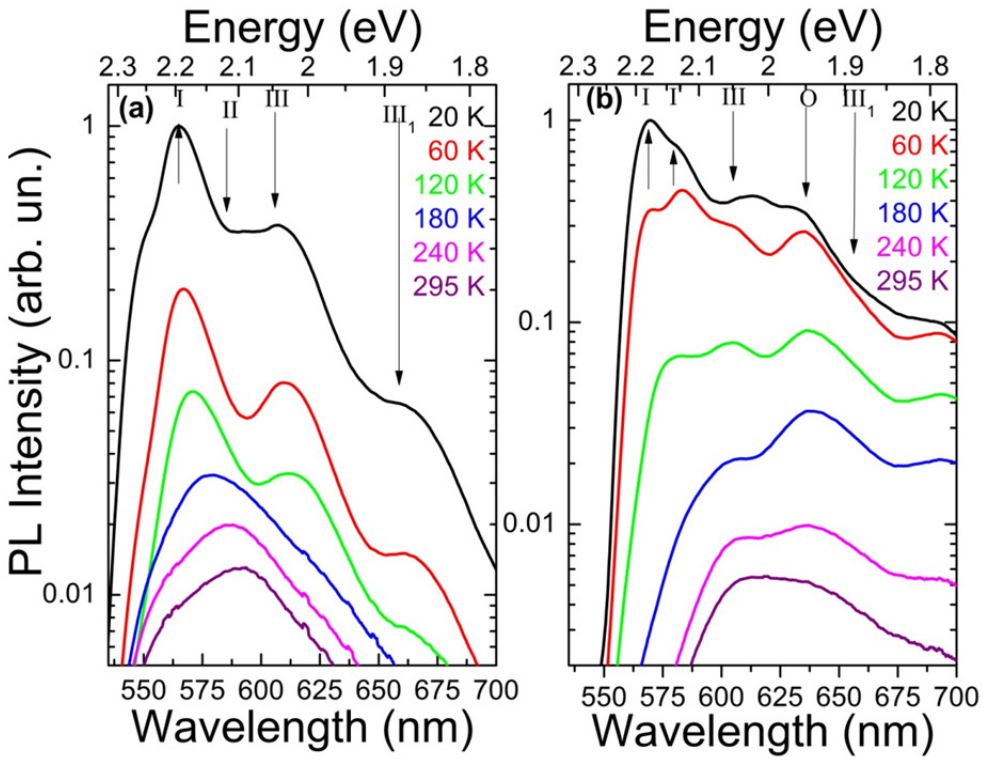

Fig. 7-2. *PL characteristics of (a) fresh (normally oxygen free) rubrene films and (b) aged (oxygen-doped) rubrene powders at various temperatures. PL bands I, II, and III, and their higher order vibronic band III_1, characteristic of fresh (normally oxygen free) rubrene films are indicated by arrows in (a), PL band I' and band O characteristic of aged (oxygen-doped) rubrene powders are indicated by arrows in (b).*

Fig. 7-3 shows the logarithm of the integrated intensities of total PL and different PL bands for aged (oxygen-doped) rubrene powders versus $1/T$. In general, two different temperature regimes can be distinguished: at very low temperatures, up to 50 K, the changing of the intensities remains slow for all PL bands except the O-band, with very low activation energy E_b. For the O-band, the activation energy is negative, which suggesting that the PL from O-band is enhancing not quenching at this temperature range. Above 50 K, a very rapid quenching is observed, with high

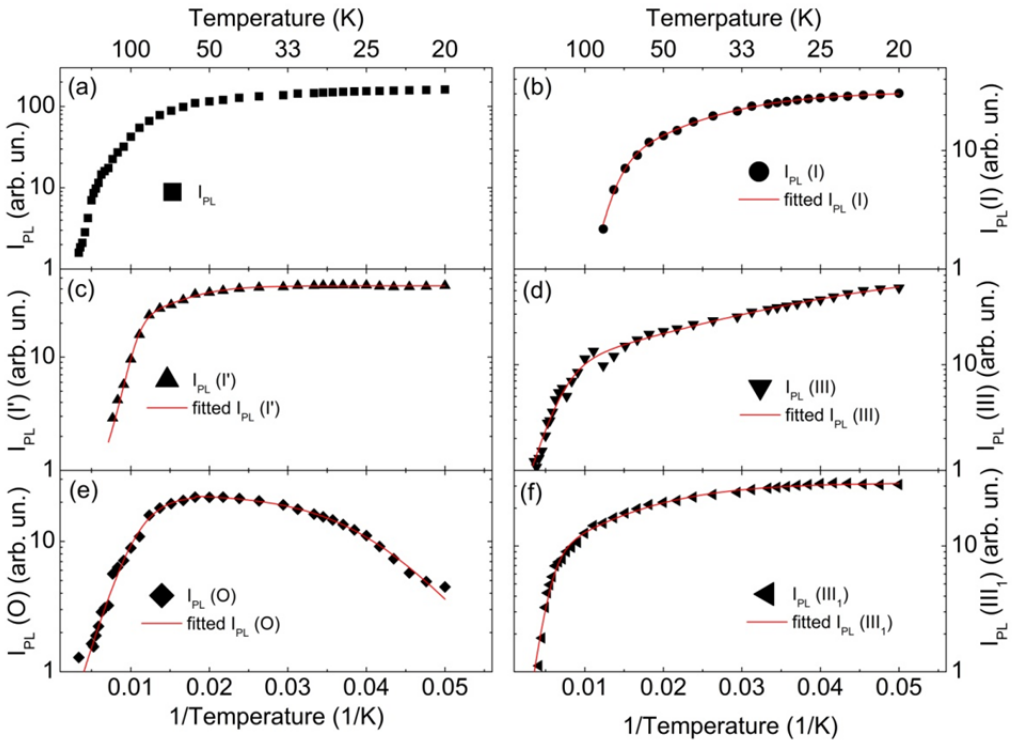

Fig. 7-3. *Temperature dependence of integrated intensities of total PL and different PL bands for aged (oxygen-doped) rubrene powders. Solid lines correspond to least square fits using the Equation 7.1 given in the text.*

activation energy E_a, indicating the free-exciton dissociation. An analysis of these data has been carried out using the well-known thermal activation relation [42-46]:

$$I_{PL}(T) = \frac{I_0}{1+\sum_i A_i e^{-\frac{E_i}{k_B T}}} \qquad (7.1)$$

A detailed evaluation shows that two activation energies are sufficient for a satisfactory fit of all PL bands. The respective activation energies obtained from the fitting procedure are given in Table 1.

Table 1. *Activation energies are shown for the all PL bands obtained from Eq. (7.1).*

PL Bands	Activation Energy E_a (meV)	Activation Energy E_b (meV)	R^2_{adj}
PL(I)	63 ± 7	10 ± 0	0.99929
PL(I')	87 ± 7	26 ± 2	0.99802
PL(III)	49 ± 7	5 ± 0	0.99614
PL(O)	39 ± 2	-13 ± 0	0.99688
$PL(III_1)$	87 ± 10	10 ± 1	0.99725

b) The negative spin 1/2 (polaron) resonance

Fig. 7-4(a) shows the negative spin 1/2 resonance of a vacuum-sealed fresh (open circles) rubrene films and an aged (solid squares) rubrene powders at room temperature. As clearly seen from Fig. 7-4(a), the fresh rubrene films exhibits no observable resonance, but the aged (oxygen-doped) powders exhibits a relatively strong negative resonance ($|\Delta I_{PL}/I_{PL}| > 0.5\times10^{-4}$) when excited by P_{exc} = 10 mW at λ_{exc}= 488 nm. This resonance is believed to be due to the enhanced formation of localized trions, in this case consisting of positive bipolarons stabilized by a negatively charged oxygen center. From the shift of the band O relative to band I, we suggest that the oxygen center is an acceptor whose level is formed ~0.25 eV above the valence band as a result of oxidation. During the optical excitation, some of photogenerated excitons decay into these oxygen centers (acceptor), emit the light at PL band O. The electrons of the decayed excitons are deeply trapped in this oxygen centers, the remaining holes acquire sufficient kinetic energy to become free, which will increase the photo-conductivity before they are captured again [8]. There are

several ways to capture the free holes, one way which is important here is forming the hole spinless bipolarons. BP itself is unstable due to its nature, so the BPs are

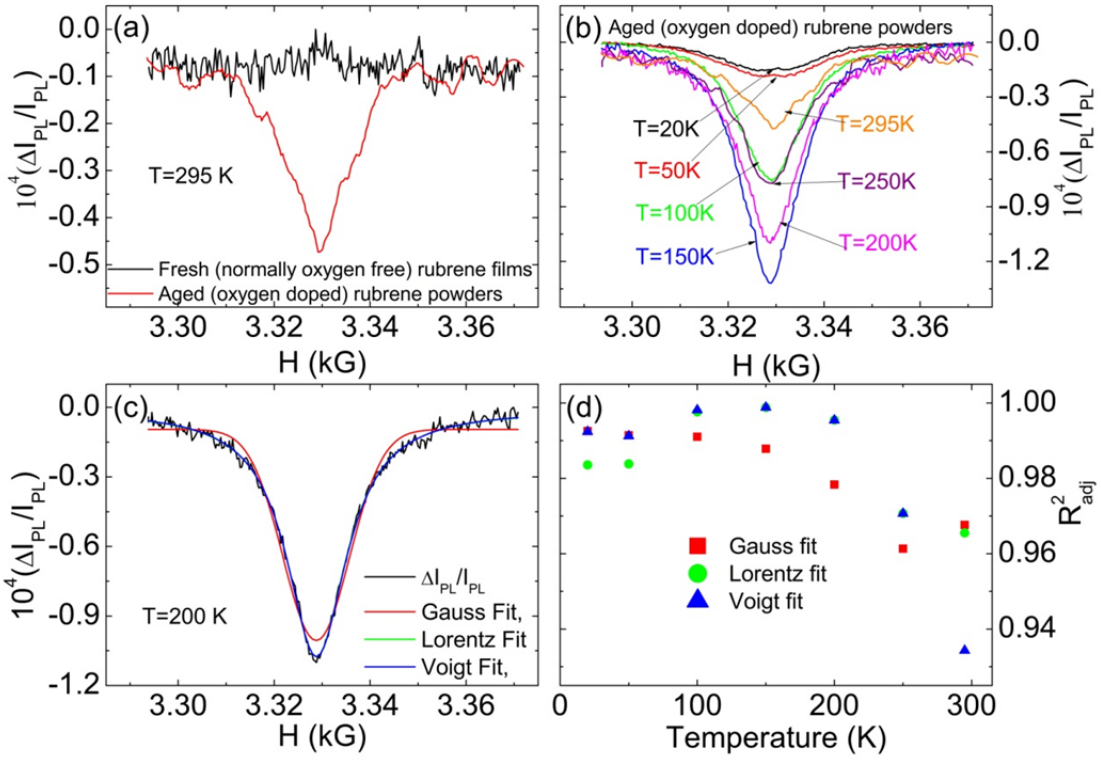

Fig. 7-4. *(a) Room temperature spin 1/2 resonance of vacuum-sealed fresh (nominally oxygen free) rubrene films (open circles) and aged (oxygen-doped) rubrene powders (solid line). (b) The negative spin 1/2 resonance in aged (oxygen-doped) rubrene powders at various temperatures. (c) 3 different fits of the negative spin 1/2 resonance at 200 K. (d) Adj. R-Square values of 3 different fits of the negative spin 1/2 resonance versus T. Samples are excited by 10 mW at 488 nm.*

stabilized by the deeply trapped electrons at oxygen centers, which are trions [29]. Under magnetic resonance condition, the spinless bipolarons formation are increased due to the microwave induced mixing. So more BPs, more trions, then the PL is quenched (BPs are the PL-quenchers) [8]. Fig. 7-4(b) shows the negative spin 1/2 resonance of the aged (oxygen-doped) powders at 20, 50, 100, 150, 200, and 295 K. Note that this temperature dependence is not monotonic. It was therefore explored in

detail. As Fig. 7-5(c) shows, $|\Delta I_{PL}/I_{PL}|$ increases with increasing T up to 180 K, and then decreases from 180 to 295 K. This behavior is distinct from that of the positive spin 1/2 resonance that is observed in other luminescent π-conjugated molecules and polymers, which invariably weakens with increasing T [11,12,16,17,20,25,26,29]. It suggests that the formation of the oxygen-center-induced localized trion is thermally activated, with an activation energy $E_a \sim 180$ K ~ 16 meV. The decrease at $T > 180$ K is possibly due to either an increasing spin-lattice relation rate and/or a decreased trion lifetime, as its dissociation rate likely increases with increasing T. Fig.7-4 (d) shows the adj. R-Square values of 3 different fits of the negative spin 1/2 resonance. It suggests that at low temperature, 20 K and 50K, the gauss fit has better adj. R-Square values than Lorentz fit, but the difference between those two fits is relatively small compared to high temperature adj. R-Square values. At high temperature ($T > 50$ K), the lineshape of this resonance is more close to a Lorentizan profile. The negative spin 1/2 resoance is maxima at 180 K (see Fig. 7-5 (c)), so at 150 K and 200 K the resonances are the clearest among all 7 resonances showing in Fig.7-4 (b). At these two temperatures, the Lorentz fit is much better than gauss fit, which may indicate the actual broadening is homogeneous for the resonance. When $T > 200$ K, the noise level is so high that the adj. R-Square values of all 3 fits are decreased a lot to 0.97-0.98 range, which means the all 3 fits are not good.

Fig. 7-5 also shows (d) $I_{PL,}$ (e) $|\Delta I_{PL}|$, and (f) $|\Delta I_{PL}/I_{PL}|$ of the spin 1/2 resonance in the aged (oxygen-doped) rubrene powders vs P_{exc} at 180 K. The observed behavior of $|\Delta I_{PL}/I_{PL}|$ is qualitatively similar to the injection current-dependence of the negative spin 1/2 ELDMR in typical polymer and small molecular OLEDs [13.25]. By monitoring I_{PL} and $|\Delta I_{PL}|$ separately, we identify, for the first time, a basic aspect of this resonance: While I_{PL} is nearly proportional to P_{exc} (Fig. 7-5(d)), $|\Delta I_{PL}|$ barely

increases with P_{exc} (Fig. 7-5(e)). This sublinear or saturation behavior results in the familiar decrease of $|\Delta I_{PL}/I_{PL}|$ with increasing P_{exc} (Fig. 7-5(f) and Ref. 13,25). It

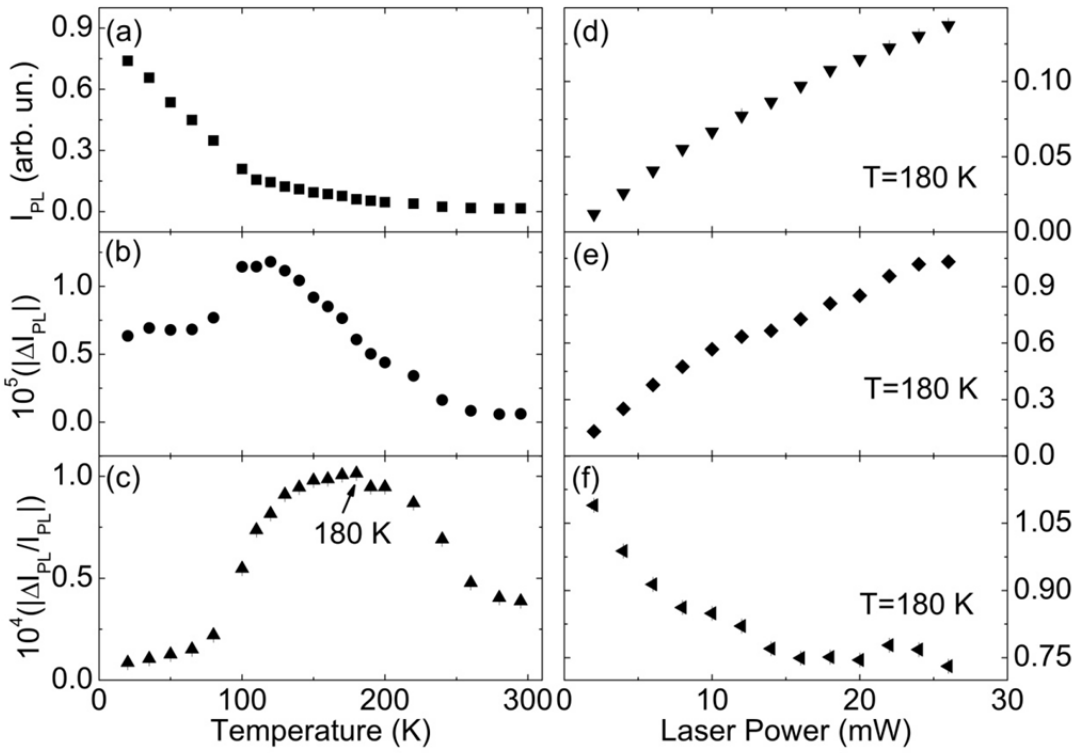

Fig. 7-5. *Temperature dependence of (a) the PL intensity I_{PL}, (b) the absolute value of the magnetic resonance-induced change in I_{PL}, $|\Delta I_{PL}|$, and (c) $|\Delta I_{PL}/I_{PL}|$ of the spin 1/2 resonance at H = 3.33 kG(shown in Fig. 7-4). Note that the dependence of $|\Delta I_{PL}|$ is distinct from that of I_{PL}. $|\Delta I_{PL}|$ is maxima at 120 K and $|\Delta I_{PL}/I_{PL}|$ is maxima at 180 K. Laser Power dependence of (d) the PL intensity I_{PL}, (e) the absolute value of the magnetic resonance-induced change in I_{PL}, $|\Delta I_{PL}|$, and (f) $|\Delta I_{PL}/I_{PL}|$ of the spin 1/2 resonance at H = 3.33 kG and T = 180 K(shown in Fig. 7-4). Note that the $|\Delta I_{PL}|$ is increased with laser power, but the $|\Delta I_{PL}/I_{PL}|$ is almost decreased with laser power.*

clearly suggests that this behavior is due to saturation of the oxygen centers with localized trions at low P_{exc}. If this scenario is correct, it clarifies the behavior of the negative spin 1/2 PLDMRs, ELDMRs and EDMRs observed to date.[13,15,16,25,26,29] They are all likely due to enhanced formation of negative or

positive bipolarons at specific sites, at which they are stabilized by a counterpolaron or other countercharge. The observation that $|\Delta I_{PL}/I_{PL}|$, $|\Delta I_{EL}/I_{EL}|$, and $|\Delta J/J|$ (where J is the current density) all decrease with increasing P_{exc} beginning at the lowest value, implies that these sites are not sufficiently dense to yield a flat dependence of the resonance on P_{exc}.

c) The TE resonances

Fig. 7-6 shows the full-field spin 1 TE PLDMR of fresh (nominally oxygen free) rubrene films at various temperatures. The full-field spin 1 TE resonance is the $\Delta m_s = \pm 1$ resonance, this resonance is very broad, here is about ~650 G. As clearly seen, at

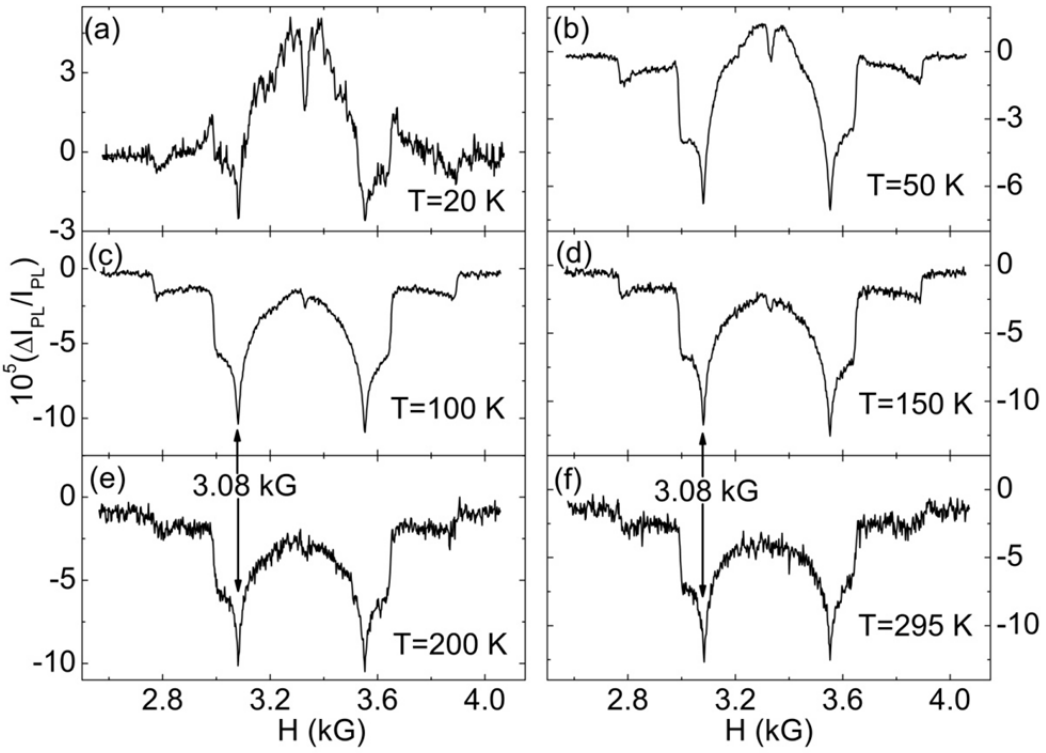

Fig. 7-6. *Full-field spin 1 TE PLDMR powder-pattern spectra of the spin 1 TE resonance of fresh (nominally oxygen free) rubrene films at various temperatures, excited by 10 mW at 488 nm.*

low T the dominant TE resonance is positive, but it gradually weakens, while a negative TE resonance strengthens, as T increases to 100 K; at T > 100 K, the

amplitude of this negative resonance remains essentially flat up to room temperature. The full-field spin 1 TE resonance of aged (oxygen doped) rubrene powders is similar to that of fresh (nominally oxygen free) rubrene films, but the amplitude is weaker. And aged (oxygen doped) rubrene powders has very stronge oxygen-induced negative spin 1/2 resonance, so the negative full-field spin 1 TE resonance of aged (oxygen doped) rubrene powders is barely observable above the noise level.

Recapping the TE powder-patterns, Fig. 7-6 shows that (i) the positive full-filed TE resonance dominates at low T while (ii) the negative resonance dominates at high T. The behavior of both resonances can be readily understood from their assumed nature: The positive TE resonance at low temperature is due to the enhanced fusion of non-geminate triplet pairs back to singlet excitons, the negative triplet resonance at high temperature is due to the reduced fusion of geminate triplet pairs back to singlet excitons.

Fig. 7-7 shows the temperature dependence of (a) $I_{PL,}$ (b) ΔI_{PL} and (c) $\Delta I_{PL}/I_{PL}$ of the full-filed spin 1 TE resonance at H = 3.08 kG(shown in Fig. 7-6) in fresh (normally oxygen free) rubrene films. The full-field spin 1 TE resonance (Figs. 7-7(b) and 7(c)) at low temperature (T < 50K) is positive, but it decreases with increasing T. At T > 50K, the resonance becomes negative and $|\Delta I_{PL}/I_{PL}|$ increases with T up to 130 -170K, and then decreases from 170 to 295 K. Fig. 7-7 also shows the exciting laser power dependence of (d) $I_{PL,}$ (e) $|\Delta I_{PL}|$ and (f) $|\Delta I_{PL}/I_{PL}|$ of the negative full-field spin 1 TE resonance in fresh (normally oxygen free) rubrene films at H = 3.08 kG and T = 150 K(shown in Fig. 7-6), where the $|\Delta I_{PL}/I_{PL}|$ is maximal. The $|\Delta I_{PL}/I_{PL}|$ is decreasing with increasing P_{exc}, which is similar to the exciting laser power dependence of negative spin 1/2 resonance. The low-temperature positive TE resonance is likely due to the same mechanism that yields the positive TE resonance in π-conjugated

polymers, namely reduced annihilation of SEs by a reduced population of TEs and polarons.[18,22]

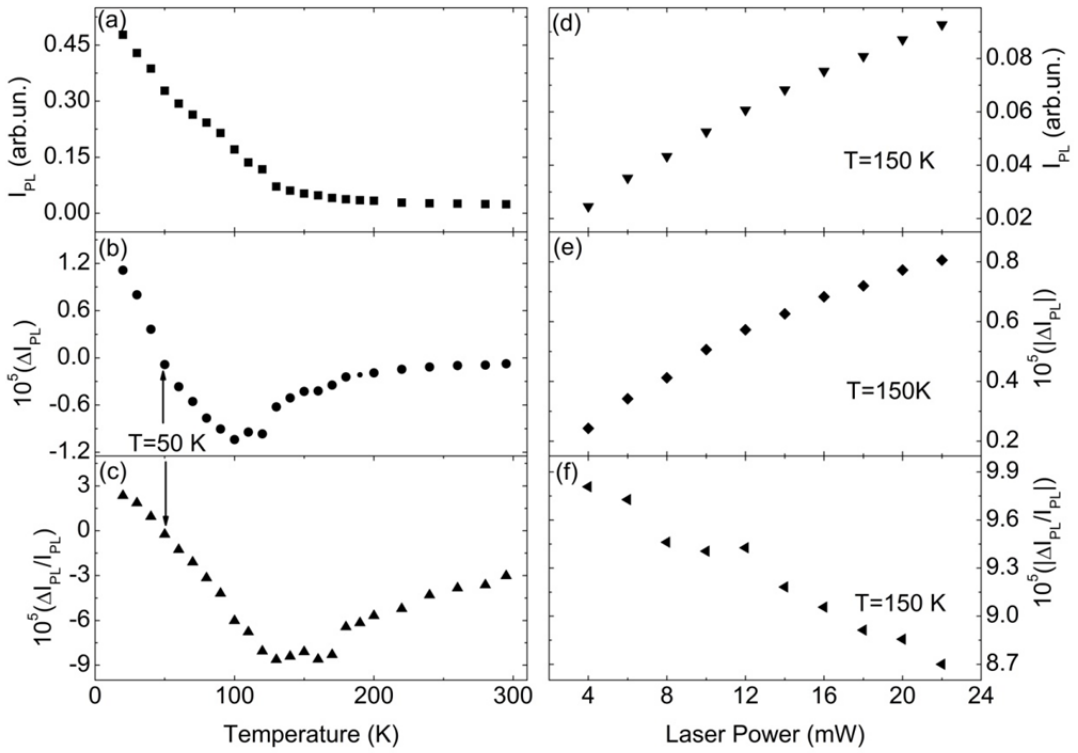

Fig. 7-7. *Temperature dependence of (a) the PL intensity I_{PL}, (b) the magnetic resonance-induced change in I_{PL}, ΔI_{PL}, and (c) $\Delta I_{PL}/I_{PL}$ of the full-field spin 1 TE resonance at H = 3.08 kG (shown in Fig. 7-6). Note that the sign of ΔI_{PL} is changed from positive to negative at 50K and it is maxima around 100 K. The $\Delta I_{PL}/I_{PL}$ is maxima around 150 K. Laser Power dependence of (d) the PL intensity I_{PL}, (e) the absolute value of the magnetic resonance-induced change in I_{PL}, $|\Delta I_{PL}|$, and (f) $|\Delta I_{PL}/I_{PL}|$ of the full-field spin 1 TE resonance at H = 3.08 kG and T = 150 K(shown in Fig. 7-6). Note that the $|\Delta I_{PL}|$ is increased with laser power, but the $|\Delta I_{PL}/I_{PL}|$ is decreased with laser power.*

Fig. 7-8 shows the Half-field PLDMR powder-pattern spectra of the negative spin 1 TE resonance of the fresh (nominally oxygen free) rubrene films at 20, 60, 90, 120, 160 and 200 K. The half-field spin 1 TE resonance is the $\Delta m_s = \pm 2$ resonance, this

resonance has only a second order dependence on the zero field splitting parameters so it is much narrower than the $\Delta m_s = \pm 1$ resonance , here is about ~80 G.

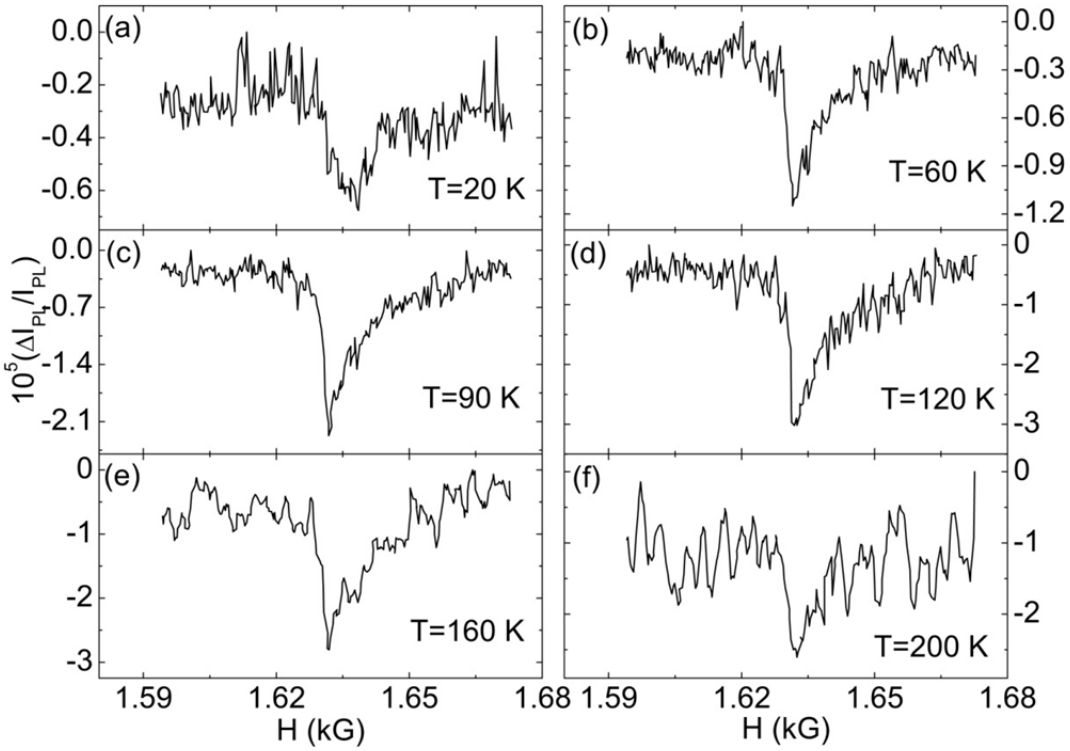

Fig. 7-8. *Half-field PLDMR powder-pattern spectra of the negative spin 1 TE resonance of fresh (nominally oxygen free) rubrene film at various temperatures, excited by 10 mW at 488 nm.*

Fig. 7-9 shows that $|\Delta I_{PL}/I_{PL}|$ (Fig. 7-9(c)) of negative half-filed spin 1 TE resonance increases with increasing T up to 130 K, and then decreases from 130 to 295 K. This behavior is very similar to the temperature dependence of negative full-field spin 1 TE resonance. Fig. 7-9 also shows the exciting laser power dependence of (d) $I_{PL,}$ (e) $|\Delta I_{PL}|$ and (f) $|\Delta I_{PL}/I_{PL}|$ of the negative half-field spin 1 TE resonance in fresh (normally oxygen free) rubrene films at 120 K, where the $|\Delta I_{PL}/I_{PL}|$ is maximal. The $|\Delta I_{PL}/I_{PL}|$ is increasing with increasing P_{exc}, which is different to the exciting laser power dependence of negative spin 1/2 resonance and the full field spin 1 TE resonance.

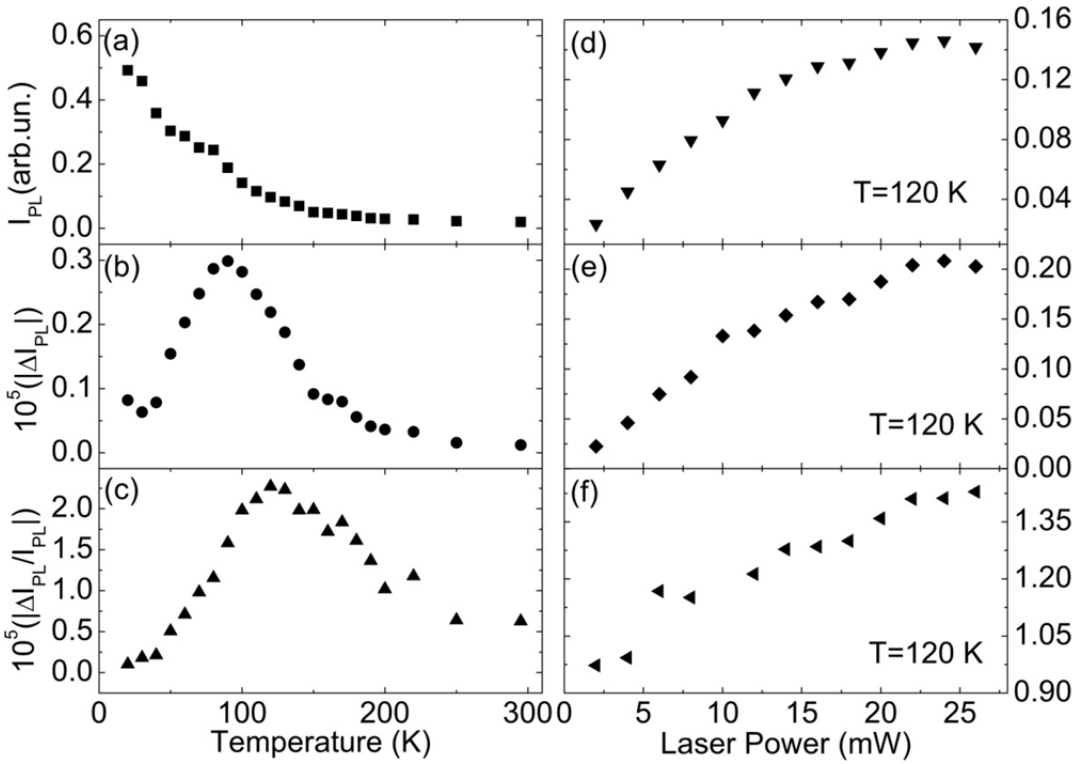

Fig. 7-9. *Temperature dependence of (a) the PL intensity I_{PL}, (b) the absolute value of magnetic resonance-induced change in I_{PL}, $|\Delta I_{PL}|$, and (c) $|\Delta I_{PL}/I_{PL}|$ of the half-field spin 1 TE resonance at H = 1.63 kG(shown in Fig. 7-8). Note that the $|\Delta I_{PL}|$ is maxima at 90 K and the $|\Delta I_{PL}/I_{PL}|$ is maxima around 120 K. Laser Power dependence of (d) the PL intensity I_{PL}, (e) the absolute value of the magnetic resonance-induced change in I_{PL}, $|\Delta I_{PL}|$, and (f) $|\Delta I_{PL}/I_{PL}|$ of the half-field spin 1 TE resonance at H = 1.63 kG and T = 120 K(shown in Fig. 7-8). Note that the $|\Delta I_{PL}|$ is increased with laser power and the $|\Delta I_{PL}/I_{PL}|$ is also increased with laser power, which is different from the spin 1/2 resonance and the full field spin 1 TE resonance.*

As mentioned above, Frankevich and coworkers [9,10] showed that the negative TE resonance is likely due to magnetic resonance inhibition of geminate TE-TE annihilation to SEs: The geminate pairs of TEs are predominantly in the singlet configuration and their spin-lattice relaxation rate is probably very low [24]. Hence, magnetic resonance conditions result in a net conversion of such pairs from the singlet

S = 0 to the triplet S = 1 and quintuplet S = 2 configurations, and in the latter configurations spin conservation prevents their fusion to a SE. The observation that the negative TE resonance amplitude increases with T up to ~100 K probably implies that the resonance, i.e., the geminate TE-TE fusion to SEs, is thermally activated across a low ~100 K ~ 9 meV barrier.

Conclusions

In conclusion, a PLDMR study of various rubrene and oxygen-doped rubrene films and powders was described. The fresh (normally oxygen free) rubrene films and powders exhibit no spin 1/2 (polaron) resonance, but they do yield two full-field spin 1 TE resonances:

(i) A positive TE resonance at low temperatures (T < 50 K), believed to result from reduced quenching of SEs by a reduced population of polarons and TEs, the latter caused by magnetic resonance enhancement of the spin-dependent TE annihilation polarons.

(ii) A negative TE resonance, which increases with T to an amplitude that levels off at ~100 K. This TE resonance is believed to result from magnetic resonance enhancement of conversion of geminate pairs of TEs from the singlet pair configuration to the triplet and quintuplet pair configurations, which prevents them from fusing back to a SE. The temperature dependence suggests a small ~9 meV barrier for this fusion.

The aged (oxygen-doped) rubrene powders also yield, besides the foregoing TE resonances, a negative spin 1/2 (polaron) resonance believed to result from magnetic resonance enhancement of the formation of localized trions at the oxygen centers. It is maximal at 180K, suggesting a barrier of ~16 meV for such trion formation.

Experimental procedures

The PLDMR system and measurement procedure have been described previously [11-13,15-21,25-29]. In brief, samples were prepared by depositing rubrene films from a 3:7 THF:toluene solvent onto the inner walls of a 4 mm outer diameter quartz tubes. To remove all dissolved oxygen from the solution, a freeze-pump-thaw cycle was performed several times until no bubbles were visible. The tube was then pumped for 24 h at room temperature and vacuum sealed. The sealed tube was then placed in the quartz "finger" dewar of an Oxford Instruments He gas-flow cryostat (enabling temperature control from 4 to 300 K), which is inserted in an optically accessible X-band microwave cavity (microwave frequency 9.35 GHz). To obtain the PLDMR, the sample was excited at 488 nm by an Ar^+ laser; the laser power was stabilized by a Cambridge Instruments laser stabilizer. The PL intensity I_{PL} was monitored using a Si photodiode. The microwave-induced change in I_{PL}, ΔI_{PL}, was determined by chopping the 810 mW X-band microwaves delivered to the sample at a chopping frequency ν_c = 500Hz, and connecting the photodiode output to the input signal channel of a lock-in amplifier referenced to ν_c. The X-band PLDMR spectra were obtained by monitoring the output of the lock-in amplifier vs the applied magnetic field.

Acknowledgments

Ames Laboratory is operated by Iowa State University for the US Department of Energy (USDOE) under Contract No. DE-AC 02-07CH11358. This work was supported by the Director for Energy Research, Office of Basic Energy Sciences, USDOE.

References

[1] *Electronic processes in organic crystals and polymers*, 2nd ed., by M. Pope and C. E. Swenberg (Oxford University Press, New York, 1999).

[2] H. Murata, C. D. Merritt and Z. H. Kafafi, IEEE Journal of Selected Topics in Quantum Electronics **4**, 119 (1998).

[3] G. Li and J. Shinar, Appl. Phys. Lett. **83**, 5359 (2003).

[4] H. Aziz, Z. D. Popovic, N.-X. Hu, A.-Mee. Hor and G. Xu, Science **238**, 1900 (1999).

[5] V. Podzorov, S. E. Sysoev, E. Loginova, V. M. Pudalov and M. E. Gershenson, Appl. Phys. Lett. **83**, 3504 (2003).

[6] V. Podzorov, E. Menard, A. Borissov, V. Kiryukhin, J. A. Rogers and M. E. Gershenson, Phys. Rev. Lett. **93**, 086602 (2004).

[7] Z. Rang, M. I. Nathan, P. P. Ruden, V. Podzorov, M. E. Gershenson, C. R. Newman and C. D. Frisbie, Appl. Phys. Lett. **86**, 123501 (2005).

[8] O. Mitrofanov, D. V. Lang, C. Kloc, J. M. Wikberg, T. Siegrist, W.-Y. So, M. A. Sergent and A. P. Ramirez, Phys. Rev. Lett. **97**, 166601 (2006).

[9] E. L. Frankevich, A. I. Pristupa and V. I. Lesin, Chem. Phys. Lett. 47, 304 (1977).

[10] V. I. Lesin, A. I. Pristupa, and E. L. Frankevich, Opt. Spectrosc+ **51**, 477 (1981).

[11] L. S. Swanson, J. Shinar and K. Yoshino, Phys. Rev. Lett. 65, 1140 (1990).

[12] L. S. Swanson, P. A. Lane, J. Shinar and F. Wudl, Phys. Rev. B 44, 10617 (1991).

[13] L. S. Swanson, J. Shinar, A. R. Brown, D. D. C. Bradley, R. H. Friend, P. L. Burn, A. Kraft and A. B. Holmes, Phys. Rev. B **46**, 15072 (1992).

[14] X. Wei, B. C. Hess, Z. V. Vardeny and F. Wudl, Phys. Rev. Lett. **68**, 666 (1992).

[15] J. Shinar, A. V. Smith, P. A. Lane, K. Yoshino, Y. W. Ding and T. J. Barton, Mol. Cryst. Liq. Cryst. **256**, 691 (1994).

[16] N. C. Greenham, J. Shinar, J. Partee, P. A. Lane, O. Amir, F. Lu and R. H. Friend, Phys. Rev. B **53**, 13528 (1996).

[17] W. Graupner, J. Partee, J. Shinar, G. Leising and U. Scherf, Phys. Rev. Lett. **77**, 2033 (1996).

[18] E. J. W. List, C. H. Kim, J. Shinar, A. Pogantsch, G. Leising and W. Graupner, Appl. Phys. Lett. **76**, 2083 (2000).

[19] E. J. W. List, J. Partee, J. Shinar, U. Scherf, K. Müllen, E. Zojer, K. Petritsch, G. Leising and W. Graupner, Phys. Rev. B **61**, 10807 (2000).

[20] E. J. W. List, C.-H. Kim, A. K. Naik, U. Scherf, G. Leising, W. Graupner and J. Shinar, Phys. Rev. B **64**, 155204 (2001).

[21] E. J. W. List, U. Scherf, K. Müllen, W. Graupner, C.-H. Kim and J. Shinar, Phys. Rev. B **66**, 235203 (2002).

[22] M. Wohlgenannt, Kunj Tandon, S. Mazumdar, S. Ramasesha and Z. V. Vardeny, Nature **409**, 494 (2001).

[23] M. Wohlgenannt, X. M. Jiang, Z. V. Vardeny and R. A. J. Janssen, Phys. Rev. Lett. **88**, 197401 (2002).

[24] M. Wohlgenannt, C. Yang and Z. V. Vardeny, Phys. Rev. B **66**, 241201(R) (2002).

[25] G. Li, C.-H. Kim, P. A. Lane and J. Shinar, Phys. Rev. B **69**, 165311 (2004).

[26] G. Li, J. Shinar and G. E. Jabbour, Phys. Rev. B **71**, 235211 (2005).

[27] M.-K. Lee, M. Segal, Z. G. Soos, J. Shinar and M. A. Baldo, Phys. Rev. Lett. **94**, 137403 (2005).

[28] M. Segal, M. A. Baldo, M. K. Lee, J. Shinar and Z. G. Soos, Phys. Rev. B **71**, 245201 (2005).

[29] A. Kadashchuk, V. I. Arkhipov, C.-H. Kim, J. Shinar, D.-W. Lee, Y.-R. Hong, J.-I. Jin, P. Heremans and H. Bässler, Phys. Rev. B **76**, 235205 (2007).

[30] D. R. McCamey, H. A. Seipel, S.-Y. Paik, M. J. Walter, N. J. Borys, J. M. Lupton and C. Boehme, Nat. Mat. **7**, 723 (2008).

[31] C. Blattler, F. Jent and H. Paul, Chem. Phys. Letters **166**, 375 (1990).

[32] G. H. Goudsmit, H. Paul and A. I. Shushin, J. Phys. Chem. **97**, 13243 (1993).

[33] A. I. Shushin, Chem. Phys. Lett. **208**, 173 (1993).

[34] A. Kawai, T. Okutsu and K. Obi, J. Phys. Chem. **95**, 9130 (1991).

[35] A. Kawai and K. Obi, J. Phys. Chem. **96**, 52 (1992).

[36] A. Kawai and K. Obi, Res. Chem. Intermed. **19**, 865 (1993).

[37] H. van Willigen, M. Vuolle and K.P. Dinse, J. Phys. Chem. **93**, 2441 (1989).

[38] C. Corvaja, L. Franco, U Pasimeni, A. Toffoletti and L. Montanari, Chem. Phys. Lett. **210**, 355 (1993).

[39] C. A. Steren, H. van Willigen and M. Fanciulli, Chem. Phys. Lett. **245**, 244 (1995).

[40] M. Reufer, M. J. Walter, P. G. Lagoudakis, A.. B. Hummel, J. S. Kolb, H. G. Roskos, U. Scherf and J. M. Lupton, Nat. Mat. **4**, 340 (2005).

[41] P. A. Bobbert, T. D. Nguyen, F. W. A. van Oost, B. Koopmans and M. Wohlgenannt, Phys. Rev. Lett. **99**, 216801 (2007).

[42] A. S. Zubrilov, S. A. Nikishin, G. D. Kipshidze, V. V. Kuryatkov, H. Temkin, T. I. Prokofyeva and M. Holtz, J. Appl. Phys. **91**, 1209 (2002).

[43] D. G. Chtchekine, Z. C. Feng, S. J. Chua and G. D. Gilliland, Phys. Rev. B **63**, 125211 (2001).

[44] G. Martínez-Criado, C. R. Miskys, A. Cros, O. Ambacher, A. Cantarero and M. Stutzmann, J. Appl. Phys. **90**, 5627 (2001).

[45] M. Leroux, N. Grandjean, B. Beaumont, G. Nataf, F. Semond, J. Massies and P. Gilbart, J. Appl. Phys. **86**, 3721 (1999).

[46] D. Bimberg, M. Sondergeld and E. Grobe, Phys. Rev. B **4**, 3451 (1971).

Chapter 8. Summary

A brief introduction of OLEDs and ODMR was provided in chapters 1 and 2. In Chapter 3, solution-processed CBP-based SMOLEDs were described and their performance was compared to that of PVK-based PLEDs, demonstrating SMOLEDs with peak power efficiency higher than any solution-processed devices and among the highest of any OLED reported to date. PLED EMLs PVK:PBD:TPD:Ir(mppy)$_3$) were obtained by spin-coating. The improved performance of these spin-coated SMOLEDs is believed to be due to the higher conductivity of CBP and the smoother spin-coated SMOLED EML. Consequently, solution-processing of SMOLEDs is expected to be a new and growing route for fabricating multi-components OLEDs, such as WOLEDs, to reduce manufacturing costs, increase device size, and avoid the complexity of the vacuum co-deposition process.

In Chapter 4, ITO-free SMOLEDs using EG-treated multilayers of the highly-conductive PEDOT:PSS as the anode was presented, which results in strongly improved device performance. The peak power efficiency $\eta_{P,max}$ = 3.82 lm/W of SMOLEDs with 2-layer (72 nm thick) PEDOT:PSS anode surpassed that of the SMOLEDs with ITO by ~81%. This strong increase in device performance is believed to result from the advantageous higher work function $\varphi_{PEDOT:PSS}$, lower refractive index $n_{PEDOT:PSS}$, reduced R_{rms} of PEDOT:PSS vs ITO, and Ohmic hole injection from the anode to the HTL induced by the MoO_3 layer. The results demonstrate that PEDOT:PSS has the potential to substitute ITO in OLEDs with strongly improved device performance.

In Chapter 5, a comparison of high and low molecular weight M_W PVK and PVK:Ir(mppy)$_3$ PLEDs demonstrated that energetic disorder induced by an increased

M_W significantly compromises device performance if cathode-quenching effects are eliminated. However, without any ETL, such as a BPhen layer, the proximity of the RZ to the cathode and the ensuing cathode quenching can result in improved device efficiency in PLEDs with a greater energetic disorder. This behavior is due to a shift in the RZ position away from the quenching cathode when hole mobility μ_h is reduced by the increased energetic disorder.

In Chapter 6, a new blue-emitting electron-accepting polymer, PFV*c*BBO, was successfully used as a dopant in the PVK-based fluorescent PLEDs. PLEDs fabricated by doping two different M_{Ws} of PFV*c*BBO (3,600 and 11,100) into two different M_{Ws} of the PVK host (~7.5×10^4 and 1.1×10^6) were demonstrated. The peak luminous efficiency $\eta_{L,max}$ = 2.11 Cd/A was achieved with low M_w PFV*c*BBO in low M_w PVK system, which also has the smoothest emitting layer. These results are due to the improved balance of the charge injection and transport in the EML by the high hole mobility TPD and the high electron mobility PBD together with the smoother surfaces of the EMLs.

In Chapter 7, a PLDMR study of various rubrene and oxygen-doped rubrene films and powders was described. The fresh (normally oxygen free) rubrene films and powders exhibit no spin-1/2 PLDMR, but they do yield the spin-1 TE resonances. (i) A positive TE resonance at low temperatures (T < 50 K), believed to result from reduced quenching of SEs by a reduced population of polarons and TEs, the latter caused by magnetic resonance enhancement of the spin-dependent TE annihilation polarons. (ii) A negative TE resonance, which increases with T to an amplitude that levels off at ~100 K, is believed to result from magnetic resonance enhancement of conversion of geminate pairs of TEs from the singlet pair configuration to the triplet and quintuplet pair configurations, which prevents them from fusing back to a SE.

The temperature dependence suggests a small ~9 meV barrier for this fusion. The aged (oxygen-doped) rubrene powders also yield, besides the foregoing TE resonances, a negative spin-1/2 PLDMR believed to result from magnetic resonance enhancement of the formation of localized trions at the oxygen centers.

Future developments will continue to focus on fabricating highly-efficient blue and white solution-processed and ITO-free phosphorescent OLEDs (PHOLEDs) and on the durability of these highly-efficient PHOLEDs. As OLED technology continues to advance, organic flexible flat-panel displays and solid state lighting products will continue to grow.

In order to fabricate blue PHOLEDs, several different organic materials are needed. Frist is the blue phosphorescent emitter, the most common one is FIrpic, but if there is some other new and more efficient blue phosphors are available, definitely I would like try. Second are the HTL, host and ETL materials. To reduce the energy loss during the host-guest exothermic energy transfer process, the lowest lying energy of triplet state E_{T1} of the HTL, host and ETL must larger than that of blue emitter, common ones are TAPC, UGH2 and 3TPYMB, respectively.

Nowadays, the dominating approach for making WOLEDs is to combine the EL from a set of different lumiphores, typically two or three, usually are red, green and blue (RGB) emitters. These lumiphores can be blended in a single layer, which is the case for the spin-coated WOLEDs, or separated in different layers of the same OLED, which is the case for ITO-free WOLEDs. So in WOLEDs, a red phosphorescent emitter, Ir(MDQ)2(acac), is necessary.

Acknowledgements

First of all, I would like to express my deep gratitude to my advisor Dr. Joseph Shinar for all the years' guidance, encouragement, support, and help. I also acknowledge his assistance and suggestions for my future career.

A special thanks to Dr. Ruth Shinar. I appreciate all her suggestions, help and support in my research and life. I also want to thank Dr. Malika Jeffries-El and her students Jeremy J. Intemann and Jared F. Mike in the Department of Chemistry for providing the new polymers.

I would like to thank my family members, especially my lovely and beautiful wife, Teng Xiao, who are always standing behind me and supporting me. I like to dedicate this dissertation to them.

My appreciation to former and current collaborators in Dr. Shinar's group: Dr. Moon-ky Lee for his guidance and help in my research, Teng Xiao, Ying Chen, Rui Liu and Emily Hellerich for their assistance and suggestions in this long journey of pursuing a PhD degree.

Finally, many thanks go to the Department of Physics and US Department of Energy for supporting my research at Iowa State University. I would also like to thank Larry, Lori, Gloria, Diane and Deb for their administrative work.